Assessment of Conceptual High-Capacity Regional Turbopropeller Aircraft

Master of Science Thesis

T.J.E. Schouten

Delft University of Technology

TU Delft

Assessment of Conceptual High-Capacity Regional Turbopropeller Aircraft

by

Thomas Johannes Eduard Schouten

to obtain the degree of

Master of Science
in Aerospace Engineering
at Delft University of Technology,

to be defended publicly on Monday April 30, 2018 at 10:00 AM.

Student number:	4104463	
Project duration:	March 2017 – April 2018	
Thesis committee:	Prof. dr. ir. L.L.M. Veldhuis,	TU Delft, committee chair
	Dr. ir. R. Vos,	TU Delft, supervisor
	Dr. ir. E. van Kampen,	TU Delft

TU Delft Delft University of Technology

Summary

Growth in air travel is expected to continue and new aircraft introduced to this growing market will need to be competitive with respect to existing designs whilst meeting strict regulation on environmental performance. This motivates aircraft designers to create more efficient design, resulting in a new interest in propeller-powered aircraft as such engines show higher theoretical propulsive efficiency as compared to turbofan engines.

The employment of turboprop engines on commercial aircraft has so far been limited on short-range regional aircraft, capable of transporting up to seventy passengers. Inspiration has been drawn from successful military applications of high-power turboprop engines to use such engines on a commercial aircraft design.

For accurate sizing of the turboprop aircraft the inclusion of propeller forces and slipstream effects is believed to be necessary in order to foresee potential complications in a later stage of the design. The implemented method is based on momentum flow theory assuming steady-state, inviscid and incompressible flow effects. Furthermore the rotational effects of the propeller slipstream are neglected in this research, simplifying the flow in the contracted wake of such a propeller to be a purely axial velocity increase. The geometry associated with such a circular slipstream is determined using a combination of the propeller thrust & normal force and the lift generation of the lifting surface.

Implementation of this theory is affecting the flow condition for each lifting surface affected by the slipstream. The influence is determined to be a combination of the change in angle of attack due to downwash and slipstream deflection and the increase in dynamic pressure aft of the propeller. Especially the latter proves to be significant in the performance assessment of the horizontal stabilizer.

Aircraft performance is collected in a set of key performance indicators summarizing the aerodynamic, propulsive and operational qualities of the aircraft. The inclusion of the power-on effects is applied to the sizing of the horizontal stabilizer. This surface is required to provide a range of forces depending on the limit under investigation. These limits are presented in a scissor plot diagram for sizing, relating the horizontal stabilizer surface area to the limits defined for longitudinal stability, equilibrium in high-lift configurations and the rate of rotation at takeoff. It is shown that for an aircraft configuration with the slipstream influencing the free stream flow condition of the horizontal stabilizer the effect of such slipstream is reducing the restrictiveness of these limits, allowing for a decrease of horizontal stabilizer area.

Applying the implemented sizing methods shows the feasibility of a 130-passenger commercial turboprop aircraft configuration where propeller effects are included in the determination of aircraft longitudinal stability & control. For configurations with increased stabilizer dynamic pressure the stability, equilibrium and rotation limits should still be satisfied in power-out conditions, eliminating the possibility of design an conventional aircraft capable of utilizing the slipstream effect to reduce the horizontal stabilizer area.

The final result shows how the position of engines is affecting the key performance indicators mostly by shifting the aircraft center of gravity aft. The set of configurations is shown to be competitive based on a comparison with existing turboprop aircraft and turbofan aircraft operating on the same mission. Robustness of the method is shown by means of a sensitivity study where variations in aerodynamic, propulsive and operational settings result in only slight deviations from the baseline design.

In order to verify the captured beneficial effect of increased dynamic pressure on the horizontal stabilizer is valid additional validation is required using experimental data. Current aircraft configuration do not allow for sizing in power-on conditions as the worst case scenario needs be considered. Future designs, most notably those with a distributed propulsion system, are expected to potentially benefit from the design conclusions drawn by analysis of this longitudinal aircraft performance.

Acknowledgments

The thesis presented is the final step in obtaining my Master of Science in Aerospace Engineering. The thesis project itself was a significant part of my studies at Delft University of Technology and as such is no isolated achievement. It is for that reason that I would like to use this page to express my gratitude towards those that stood by me in one way or another.

First I would like to thank my supervisor, Dr.ir. Roelof Vos, for providing me with the opportunity to graduate within aircraft design. The field of aircraft design is a broad and challenging one and his guidance, advice and support allowed me to define the thesis as it is presented. Thanks to everyone who assisted me in the technical implementation of the thesis and to the committee members for dedicating their time to critically review my work. A big thanks to all my fellow students, especially those in rooms 1.07 & 1.09, for helping create the pleasant working environment where I spent the better part of a year.

Lastly, I want to thank my family for their unlimited support and encouragement throughout my time in Delft. A special thanks goes to Iris for her patience in doing so whilst always being a source of motivation for me.

Tom Schouten,
Delft, April 2018.

List of Figures

List of Tables

Abbreviations

a.c.	aerodynamic center
ADT	actuator disk theory
ASK	available seat kilometers
AVL	Athena Vortex Lattice
BWB	blended wing body
c.g.	center of gravity
DatCom	Data Compendium
DOC	direct operating cost
DUUC	Delft University Unconventional Configuration
EASA	European Aviation Safety Association
ESDU	Engineering Sciences Data Unit
HLD	high lift device
KPI	key performance indicator
LLT	lifting line theory
mac	mean aerodynamic chord
MFM	mission fuel mass
MTOM	maximum takeoff mass
n.p.	neutral point
NLF	natural laminar flow
OEM	operating empty mass
RTP	Regional TurboProp
SFC	specific fuel consumption
SM	static margin
USAF	United States Air Force
VLM	vortex-lattice method

Nomenclature

Latin Symbols

A	aspect ratio	(~)
a	speed of sound	(m/s)
B_P	number of propeller blades	(~)
b	wing span	(m)
b_F	fuselage diameter	(m)
c	chord length	(m)
$\bar{c}$	mean aerodynamic chord	(m)
C_D	drag coefficient	(~)
C_L	lift coefficient	(~)
C_{L_α}	lift gradient	(~)
C_m	pitching moment coefficient	(~)
C_N	normal force coefficient	(~)
C_T	thrust coefficient	(~)
D	drag force	(N)
D_P	propeller diameter	(N)
d	slipstream diameter	(m)
E_U	energy metric	(MJ/ASK)
h	altitude	(m)
h_F	fuselage height	(m)
J	propeller advance ratio	(~)
L	lift force	(N)
l_F	fuselage length	(m)
l_H	tail arm length	(m)
M	pitching moment	(N)
M_∞	free stream Mach number	(~)
M_{tip}	blade tip Mach number	(~)
$\dot{m}$	mass flow rate	(kg/s)
N	normal force	(N)
n	rotations per second	(s^{-1})
P	propeller power	(W)
q	dynamic pressure	(kg/ms^2)
R	harmonic mission range	(km)
S	main wing surface area	(m^2)
S_H	horizontal tail surface area	(m^2)
S_D	normalized drag area	(~)
T	thrust force	(N)
T_C	thrust coefficient	(~)
V	main wing free stream velocity	(m/s)
V_H	horizontal tail free stream velocity	(m/s)
V_R	takeoff rotation velocity	(m/s)
V_S	stall velocity	(m/s)
V_S	slipstream velocity	(m/s)
V_∞	aircraft freestream velocity	(m/s)
W	weight force	(N)
x_{ac}	position of a.c.	(m)
$\bar{x}_{\text{ac}}$	normalized position of a.c.	(~)
x_{cg}	position of c.g.	(m)
$\bar{x}_{\text{cg}}$	normalized position of c.g.	(~)

x_{mg}	position of main gear	(m)
$\bar{x}_{\mathrm{mg}}$	normalized position of main gear	(∼)

Greek Symbols

α	angle of attack	(°)
β	blade pitch angle	(°)
Δ	symbol denoting change	(∼)
δ	flap deflection angle	(°)
ϵ	downwash angle	(°)
η	efficiency	(∼)
θ	deflection angle	(°)
$\dot{\theta}$	rate of rotation	(°/s^2)
λ	taper ratio	(∼)
ρ	air density	(kg/m^3)
σ	propeller solidity	(∼)

Contents

1 Introduction

The introductory chapter of this thesis will explain the motivation for the research in Section 1.1. The research objectives and research question are presented in Section 1.2 before the structure of the thesis is shown in Section 1.4.

1.1. Research motivation

Air travel is expected to double over the next 20 years, where three-quarters of the market requires short to medium range regional aircraft to fulfill passenger demand.[7] New aircraft in this market should perform the envisioned mission at a reduced fuel burn as compared to existing designs, stemming from more stringent aircraft emission regulation together with the desire of airliners to reduce costs. As such, these aircraft could be powered by turbopropeller engines. Outperforming existing aircraft in the context of this thesis is defined as reducing operational costs and ecological footprint of the aircraft.

This rationale leads to the questions and objectives of the following section.

1.2. Research Question & Objective

The research presented in this thesis is of an exploratory nature, determining if a large turboprop configuration can be competitive in the future. For the creation of the design the effects of propeller forces and slipstream are included to obtain a feasible design accounting for (potential) adverse power-on effects which leads to the following main research question:

> Can a large-capacity aircraft with turboprop engines be competitive based on top-level performance when created using a design generator accounting for the influence of the propeller forces and slipstream effects on the horizontal stabilizer sizing?

Which is split in a number of sub-questions:

> How do propeller forces and slipstream effects influence the sizing of the horizontal stabilizer of an aircraft?
>
> Can a large-capacity passenger turboprop aircraft be converged using the design generator?
>
> How does the placement of the engines affect the top-level performance of the turboprop aircraft?

The belief is that a converged and correct aircraft design can only be obtained by implementing some methods to account for the propeller slipstream effect. This will improve the overall design for all propeller aircraft sized with the same tool. The objective of the research can be summarized as follows:

> Assess the top-level performance of a large stabilizer-mounted-turboprop aircraft design incorporating the effects of the propeller in power-on situation.

This objective can only be achieved by performing the following actions for this research:

1. Implement slipstream and propeller force effects in the sizing method for the horizontal stabilizer as to foresee design driving situations in the power-on scenario.
2. Verify and validate the horizontal tail sizing method in the design tool to create a feasible aircraft configuration.
3. Create a family of equal-requirement turboprop aircraft with various engine locations to assess how the placement of the engine affects the performance of the initial design.
4. Perform a study of design robustness accounting for (future) technology advancements in the fields of propulsion and aerodynamics as well as imposed operational constraints.

1.3. Research Scope

As both the fields of aircraft design and propeller aerodynamics span a far to great amount of subjects to include in the scope of a master's thesis, the research is limited. The choice has been made to limit the investigation in aircraft configuration effects to aircraft with conventional lifting surfaces, meaning a main wing is present about halfway the tube-style fuselage and a horizontal stabilizer is installed at the rear of the aircraft. For this horizontal stabilizer, two distinct designs are considered being the conventional tail layout and the T-tail layout. The placement of the turboprop engines is the performance influence of interest in the research where specific choices for engine placement are expected to impact the top-level performance of the aircraft significantly.

This aircraft performance is primarily assessed for the longitudinal stability and equilibrium control of the aircraft where the main focus is to determine the influence of the propeller forces and slipstream effects on the horizontal tail. For the inclusion of propeller forces and slipstream effects the focus is on axial flow effects only to create a two-dimensional situation for the flow conditions. This choice impacts the final result as rotational effects are expected to contribute to the change in distribution of lift and drag of lifting surfaces.

In order to obtain a first inclusion of propeller slipstream effects on the horizontal stabilizer sizing of aircraft the two-dimensional flow problem described will be able to show the influence of a change in axial flow properties of lifting surfaces, capturing a dominant effect in the early design stages. The believe is that this implementation allows the designer to be forewarned of potential unwanted effects stemming from propeller installation at which point more detailed performance assessments can be performed.

1.4. Thesis structure

The report will start with a theoretical outlook on propeller and slipstream development in Chapter 3. . Chapter 4 shows the stabilizer sizing method and how the implementation of this method is performed in the existing design tool. Chapter 5 starts with a verification of these methods before the implementation is validated. The new turboprop aircraft are presented and assessed in Chapter 6 after which a sensitivity study of the designed aircraft is performed. Finally, conclusions and the answer to the research question are presented together with recommendations for future development in Chapter 7.

2

Aircraft Design Objective

Aircraft are introduced to the market only if they are competition to existing designs. As such the need is present to outperform existing aircraft or to create a design that is able to be unique in operation. The aim of this research is to investigate the capabilities of the Regional TurboProp (RTP) to do both, that is to outperform existing turboprop and turbofan designs by creating a large capacity turboprop design. In order to determine the minimum requirements of the RTP it is crucial to determine what existing and operational turboprop aircraft offer in Section 2.1. Following that comparison the requirements for the design can be derived and quantified in Section 2.2 before design configurations are presented in Section 2.3.

2.1. Existing Aircraft

In order to warrant the research into a large regional aircraft powered by turboprop engines it is important to state the market in which such an aircraft will be operated. Current-day operational turboprop aircraft are co-defined by their maximum passenger capacity, being 50 passengers for the single-class Saab 2000 and Fokker 50 aircraft and up to 68 passengers for the ATR 72-600. These aircraft are all presented in Figure 2.1 showing the relative small size of these aircraft.

(a) ATR72-600, 68 passengers

(b) Saab 2000, 50 passengers

(c) Fokker 50, 50 passengers

Figure 2.1: Typical current in-service regional turboprop aircraft

For this research a new configuration is proposed with a deviation from the existing set of turboprop aircraft. The main feature of this aircraft should be the capacity to carry up to 130 passengers in a single economy configuration over a range exceeding that of the existing turboprop aircraft. To do so the new Europrop TP400-D6 turboprop engine, capable of providing over $8000\ kW$ shaft power [5], is used as engine of the envisioned turboprop aircraft. Initially designed for and implemented on the military Airbus A400 Atlas transport aircraft, the proposed design will be the first commercial aircraft implementing two of these powerful turboprop engines.

The choice for turboprop propulsion stems from the expected increase in propulsive efficiency relative to jet powered aircraft. The derivation of propulsive efficiency is later presented in Chapter 3. For now the market analysis of Babikian et al. shows with Figure 2.2 that historically regional turboprop aircraft are more efficient than regional jets. The energy metric E_U presented is the required fuel energy in Joules divided by the available seat kilometers (ASK). This is a direct relation between income (ticket sale) and expense (fuel) where a lower metric depicts a higher operational efficiency for potential airliners.

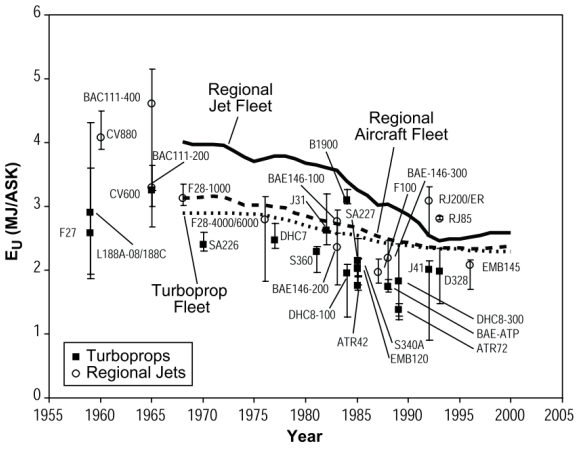

Figure 2.2: Trend of energy efficiency for regional aircraft showing averages for jets and propellers, [6, p. 391]

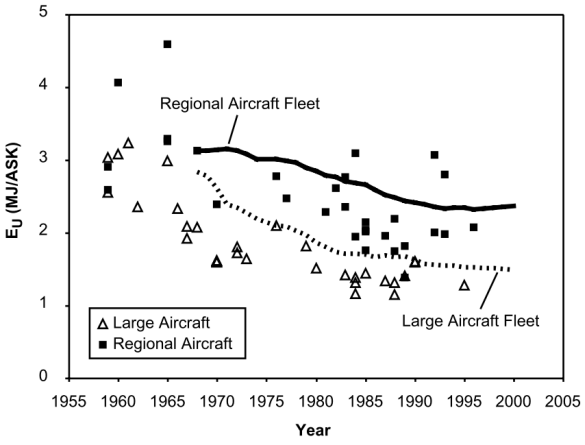

Figure 2.3: Trend of energy efficiency for large aircraft and regional aircraft, [6, p. 391]

From these trend lines it is clear the gap between jet powered and propeller powered aircraft is decreasing over time. This is interesting as it would drive the design towards a jet powered configuration, were it not for the fact that a significant reduction of E_U is shown from the ATR42 (introduced 1985) to the ATR72 (introduced 1989). These two aircraft feature a similar design and level of technology where the ATR72 is showing a reduction in energy metric of almost 25%. This difference is contributed fully to the increased passenger capacity of the ATR72 aircraft where the total ASK is increased by 65% relative to the ATR42, increasing total efficiency.

The theorem of increasing the ASK to obtain a more energy efficient design is further reinforced by the comparison of regional aircraft (combined jet and propeller) and large aircraft (turbofan powered) in Figure 2.3. If one contributed an improvement of energy metric to just the method of propulsion one would expect regional aircraft to outperform the large aircraft. Instead, the large aircraft show a substantial reduction in this metric, indicating the absolute size of the aircraft is a dominating influence in the comparison.

It is for this reason that the focus will be on a high-capacity turboprop aircraft which is expected to show beneficial propulsive efficiency for a high ASK, thereby providing a new option in the market for intra-continental air travel. The recent development of the Bombardier CSeries aircraft, shown in Figure 2.4, shows the feasibility of aircraft with such a capacity in the current market.

Figure 2.4: Bombardier CS100 turbofan aircraft

With the main difference between the Bombardier CS100 and the envisioned RTP being the propulsion system it is not possible to one-on-one compare the aircraft, however, the Bombardier CS100 can provide valuable input for the creation of a 130 passenger single-class aircraft design.

2.2. Top Level Requirements

After the choice is made to investigate a turboprop aircraft with a larger passenger capacity than currently existing turboprop aircraft it is important to quantify the performance requirements of this aircraft. Each requirement stems from one of the following three sources:

- Bombardier CS100 performance & design;
- propeller operation restrictions;
- Aircraft Design Initiator restrictions.

Where the first will be explained in this section. Restrictions stemming from the employment of a propeller on the aircraft will be briefly touched upon before being described in detail in Chapter 3. Lastly, any restrictions stemming from the assessment tool in the form of the Aircraft Design Initiator will be presented in Chapter 4.

The top-level requirements of an aircraft present the minimal level of compliance the design should adhere to. As such these requirements are strong drivers for the design and quantification of these requirements needs to be done with great consideration. The top level requirements for the RTP are summarized in Table 2.1.

Table 2.1: Top level requirements for conceptual RTP

pax (~)	$R_{\text{max. pax}}$ (km)	h_{cruise} (m)	M_{cruise} (~)	b_{max} (m)
130	2960	8500	0.60	35

The passenger capacity stems from the desire to create a larger turboprop than currently existing and is set equal to the Bombardier CS100 aircraft. [8] The range requirement is derived from the mission profile of this turbofan design as equal endurance of the aircraft. This means the cruise phase for both aircraft is taking an equal amount of time but, for the lower cruise velocity of the RTP, this means a reduction in range. This cruise velocity, expressed in Table 2.1 as Mach number M, together with cruise altitude h is a direct consequence of the turboprop propulsion system as will be explained further in Chapter 3. Finally, the requirement is put in place to not exceed the Bombardier CS100 wing span b of 35m as to allow the new RTP to service the same airports.

These five top level requirements will feature prominently in the creation and the assessment of the RTP aircraft. Together with the settings required for the Aircraft Design Initiator (see Chapter 4) they form the basis of the performance assessment.

The requirements in Table 2.1 regarding the mission range and passenger capacity stem from a direct comparison with the in-development Bombardier CS100 aircraft.[4] This turbofan aircraft is capable of transporting 130 passengers in a 2-3 seating arrangement for a total mission of almost five hours. The maximum wing span b_{max} of is taken directly from the CS100 as well. The selection of turboprop engines results in a decrease of available range for equal mission time to under $3000km$ $(1600NM)$. A comparison of the range for the European internal market is presented in Section 2.2, showing the ability of the RTP to fill the gap between current turboprop and turbofan aircraft. Unless stated otherwise, any range given is the harmonic mission range for maximum payload.

The envisioned RTP aircraft is designed with the Europrop TP400-D6 turbopropeller engine in mind. This is the only western engine capable of providing over 8000kW of shaft power required for the propulsion of this aircraft.[5] This power is converted to thrust using two 10-bladed constant speed propellers with $M_{\text{tip}} = 0.93$ as to avoid supersonic flow conditions. Propeller diameter D_P is derived with Equation 3.14 to obtain the design diameter of 3.18m.

This is because both cruise altitude h_{cruise} and Mach number M_{cruise} are a result from powerplant selection, the Europrop TP400-D6 turbopropeller engine. This is the only western engine capable of providing over $8000kW$ of shaft power required for the propulsion of the envisioned turbopropeller aircraft.[5] This power is converted to thrust using two 10-bladed constant speed propellers limited in diameter by the tip Mach number limit of 0.93 as to avoid supersonic flow.

2.3. RTP Configurations

The main innovation in design is the placement of the turboprop engines. The initial design will be powered by two horizontal stabilizer tip-mounted engines at the rear of the fuselage. Such a configuration

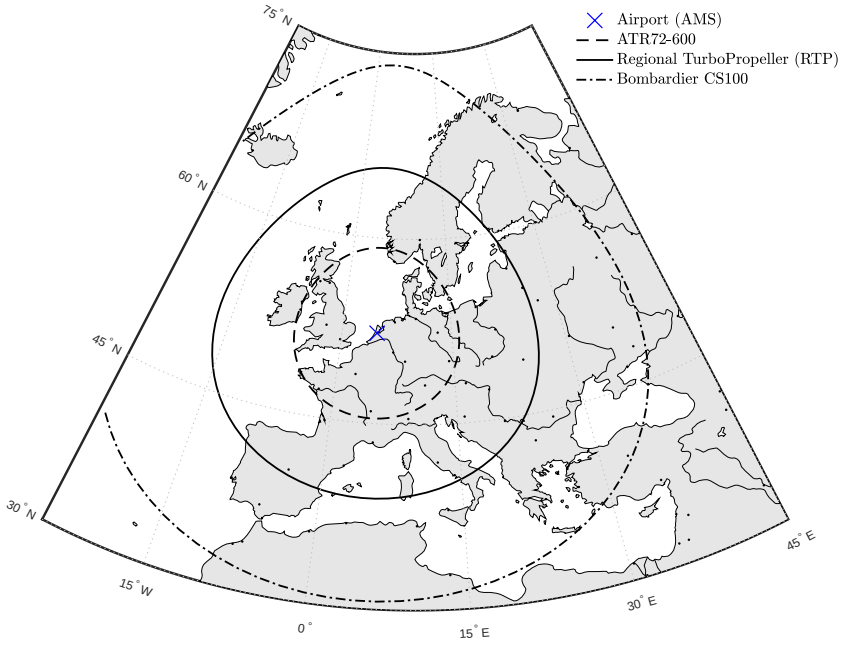

Figure 2.5: Comparison of aircraft harmonic mission range from Amsterdam Schiphol airport

is believed to possess favorable design elements as it uses a pre-existing component for mounting the engine and it clears the main wing of flow-disturbing elements. Potential risks include a larger tail surface to allow for compliance with aircraft limits in equilibrium and control. To assess whether such a design is the best for the mission, a family of designs is created to determine how design choices result in a desirable configuration. The configurations selected will be shown in more detail later and will be chosen based on the analysis presented in Table 2.2.

Table 2.2: Trade-off matrix for engine placement configurations. Adapted from Goldsmith [19]

	Tractor				Pusher	
Configuration	**Pylon**	**H-Tail**	**V-Tail**	**Fuselage**	**Pylon**	**H-Tail**
Aerodynamics						
S&C	1	2	3	4	5	6
Drag	5	1	2	4	6	3
Performance	2	1	2	6	4	5
Structures	4	5	1	6	2	3
Dynamics	no particular preference, movable surfaces present problems					
Weights	1	2	3	6	4	5
Acoustics	5	3	4	6	1	1
Hamilton Standard						
Aerodynamics	3	1	2	n.a.	4	5
Structures	1	2	3	n.a.	4	5
Acoustics	3	2	1	n.a.	4	5
Ranking	3	1	2	4	5	6

From the trade-off performed by Goldsmith the following conclusions are drawn. First of all, any pusher arrangement where the propeller is placed aft of the engine is estimated to perform poor compared to a tractor configuration. The option with two tractor propellers powered by an engine installed in the aft fuselage is scoring in the lower half of options for each design group and as such will not be investigated further. Each of the remaining three configurations show promising performance with different design areas dominating the ranking for each configuration.

The least compromising option appears to be integrating the engines in the horizontal tail as aerodynamics seem most favorable for this option. The pylon-mounted configuration is suffering from the introduction of the pylons which increase the wetted area of the aircraft and influence the drag performance. The V-Tail design of Table 2.2 is a combined horizontal and vertical tail which includes the engines. As the main field of interest for this thesis is longitudinal stability and control under influence of propeller effects this situation is undesired as it strongly couples longitudinal and lateral control.

As such, taking into account the existing turboprop aircraft, the 130-passenger Bombardier CS100 and the trade-off performed by Goldsmith, the four RTP aircraft configurations of Table 2.3 are selected to be assessed.

Table 2.3: Layout configurations for new regional turboprop aircraft

Name	Main wing	Engine	Hor. Stabilizer
RTP1	Low	Above	Conventional
RTP2	High	Below	T-Tail
RTP3	Low	Fuselage	T-Tail
RTP4	Low	Hor. Stabilizer	Conventional

This set of RTP configurations is believed to cover the most promising layouts and will allow for the influence of propeller effects to be assessed over a variety of configurations. The first two configurations mimic existing regional turboprop aircraft configurations, the Fokker 50 and the ATR72 respectively. An example of the envisioned RTP2 configuration, following from the ATR72 design, is presented in Section 2.3. Furthermore the overlap with the configurations of Goldsmith for RTP 3 & 4 allows a validation to be performed to identify possible discrepancies in analysis between that research and this thesis, improving the reliability of the implemented longitudinal performance assessment.

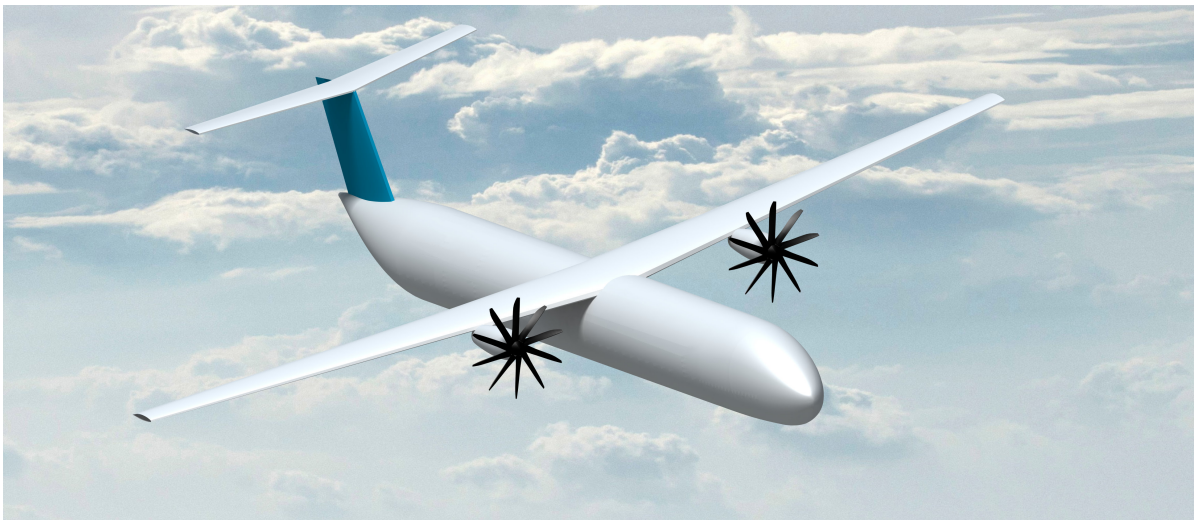

Figure 2.6: Design configuration overview for the RTP2 aircraft

3

Theoretical Background

The new RTP will be a large propeller-powered commercial aircraft and it is expected that the performance is dependent on the presence of propeller effects. These propeller effects can be split in the direct propeller effects, resulting from the forces acting on and from the propeller, and in slipstream effects. The first include but are not limited to the presence of thrust misalignment and propeller normal forces, where the second affect the flow around and aft of the propeller. These contributions are usually not considered in much detail for conceptual propeller aircraft design even though they may pose limits on the design of such aircraft.

As shown in the research objective of Chapter 1, the goal is to include power-on effects in the analysis and sizing of a conceptual aircraft design. This chapter will present the theories underlying the implementation, starting with the methods employed for propeller effects in Section 3.1. Next, the presence of the slipstream and associated effects are explained in Section 3.2 before finally the influences of power-on effects are presented in Section 3.3.

3.1. Propeller Theory

The new concept aircraft presented in this thesis, the RTP, is powered by turboprop engines. The reason such engines are selected is because turboprop engines have been proven to achieve higher propulsive efficiency than turbofan aircraft, see Figure 3.1.

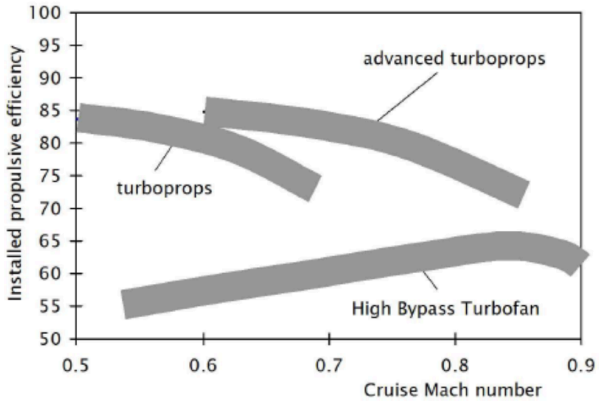

Figure 3.1: Comparison of propulsive efficiency versus Mach number for different aero-engine types [29, p. 9]

This increase in propulsive efficiency (η_p) is following from the theory of actuator disk theory (ADT) in Section 3.1.1. Direct propeller forces influencing aircraft performance are discussed in Section 3.1.2 before some design considerations are presented in Section 3.1.3.

3.1.1. Actuator Disk Theory

Propeller performance and flow modeling is a complex field of aerodynamics which is simplified for the purposes of this research. The method applied to determining the propeller effects is ADT. ADT has been around from before the application of propellers on aircraft, providing a method to determine marine propeller performance. The application method relies on a number of assumptions:

- steady-state analysis;
- no viscous effects;
- no flow compressibility;
- no rotational effects.

The underlying analysis of performance stems from momentum theory which is best summarized by McCormick [22]: *"momentum theorem in fluid mechanics is the counterpart of Newton's second law in solid mechanics, which states that a force imposed on a system produces a rate of change in the momentum of the system"*. For ADT the imposed force is the thrust force T delivered by the propeller and the system is a control volume as presented by Figure 3.2.

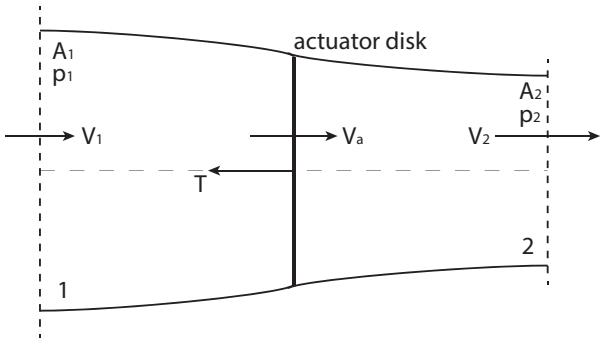

Figure 3.2: Momentum theory control volume with actuator disk

In this control volume the propeller is replaced with a disk, hence the naming of ADT. Velocity is continuously increasing from upstream (station 1) towards downstream (station 2). The mass flow $\dot{m}$ throughout the system is required to remain constant which, using Equation 3.1, requires the cross-sectional area A to decrease for stations of increased velocity V, taking into account the assumption of incompressible flow.

$$\dot{m} = \rho A V \tag{3.1}$$

The next step in determining the properties of the actuator disk system is to express propeller T in terms of the flow properties. Applying momentum theorem in the axial direction, the integral of Equation 3.2 is representing the force on the system due to flow properties. [22]

$$\sum F_x = \int_s u_x \rho V_1 \mathrm{d}s \tag{3.2}$$

Where $\sum F_x$ is equal to T and, by analyzing Figure 3.2, the right-hand side should be equal to the momentum flux of the system. Combining Equation 3.1 and Equation 3.2 the result is presented in Equation 3.3.

$$T = \dot{m}(V_2 - V_1) \tag{3.3}$$

The final step to be taken is to relate T to the power P present in the control volume. Total power in the system can be defined as the difference in kinetic energy between station 1 and station 2, shown with Equation 3.4.

$$P = \dot{m}\left(\frac{V_2^2}{2} - \frac{V_1^2}{2}\right) = \dot{m}(V_2 - V_1)\frac{V_2 + V_1}{2} \tag{3.4}$$

Next it is important to determine propeller power, equal to the thrust force multiplied with the flow velocity. One obtains the relation of Equation 3.5, using Equation 3.3 for the thrust force exerted.

$$P = TV_a = \dot{m}(V_2 - V_1)V_a \tag{3.5}$$

Combining this relation with Equation 3.4 it is clear the velocity at the actuator disk V_a is equal to the average of the free stream and slip stream velocity. This in turn means the flow is accelerated in equal amounts ahead and aft of the propeller. Relating the power obtained from the propeller and the power of the system, one can see the efficiency is equal to the ratio of usable power in the form of thrust and total power in terms of momentum flux. The final relation for propeller efficiency is represented by Equation 3.6.

$$\eta_p = \frac{1}{1 + \frac{V_2}{V_1}} \tag{3.6}$$

Showing that any flow acceleration between stations 1 (free stream) and 2 (slipstream) reduces the efficiency of the propeller. It should be noted that the same relation is valid for jet propulsion, explaining the difference in efficiency in Figure 3.1. Flow is required to accelerate for a net thrust force to be present, showing a conflict of interest for efficient propulsion systems. The approach taken by propellers is to minimize acceleration for a large mass flow, resulting in a significant efficiency increase over jet propulsion which are required to greatly accelerate a limited mass flow. For turbofans, a combination of effects is present where an increase in bypass ratio will allow a greater efficiency as the system is mimicking the principles of propeller propulsion.

The equations presented for ADT are required in the determination of slipstream geometry in Section 3.2 where the fundamental slipstream theory for this thesis is explained.

3.1.2. Propeller Forces

The previous section covered axial flow velocity and the change in flow properties by means of ADT. Here the consequences of propeller forces are explained. The main goal of the propeller is to provide thrust. Together with this thrust force a side force and normal force is present, totaling forces in all three directions of the propeller axis system. On top of this, moments along these axes will exist.

According to Veldhuis the two elements of interest are the thrust force and the normal force. [29] The first since it is the main reason to operate the propeller in the first place and the latter as it is influencing stability of the aircraft. The side force and moments present are to be neglected in order to reduce the complexity of the problem at hand and because their influence on the longitudinal stability and control of the aircraft is assumed marginal.

The influence of the thrust and normal force can be seen analogously to the lift of a surface. As a matter of fact, the main effect, apart from generating thrust, is influencing the total lift of the aircraft. This influence is due to two components which will be briefly explained next.

Vertical Thrust Component

The first, the vertical component of thrust, can be quantified by decomposing T along the angle of attack of the propeller α_P by means of Equation 3.7.

$$C_{L_T} = C_T \sin \alpha_P \tag{3.7}$$

Where the thrust coefficient C_T is given in Equation 3.8.

$$C_T = \frac{2T}{\rho V_\infty S} \tag{3.8}$$

This equation normalizes T with the free stream density ρ, flow velocity V_∞ and the wing surface area S. This coefficient is largest for high-thrust and low-velocity conditions such as aircraft take-off and landing. The vertical component of thrust will only be significant in case a substantial α_P is present.

Normal Force

Propeller normal force N is always perpendicular to the propeller thrust T and is present because of the change in flow direction presented before. The normal force coefficient C_N is therefore a contribution to the total lift of an aircraft and needs to be included for this reason. The method used to determine the change in C_N with the propeller angle of attack α is adopted from De Young [14] as presented in Equation 3.9.

$$\frac{\mathrm{d}C_N}{\mathrm{d}\alpha_P} = \frac{4.25\sigma_e}{1+2\sigma_e} \sin(\beta_0 + 3) \cdot f \cdot \frac{\pi J^2}{8} \tag{3.9}$$

Where B_0 denotes the blade pitch angle at zero lift for a 75% radial position along the blade and the blade solidity σ_e, the advance ratio J and the thrust factor f are presented in Equations 3.10 to 3.12.

$$\sigma_e = \frac{4B_P}{3\pi} \frac{c_P}{D_P} \frac{C_{l_{\alpha,\mathrm{P}}}}{0.95 \cdot 2\pi} \tag{3.10}$$

$$J = \frac{V_\infty}{nD_P} \tag{3.11}$$

$$f = 1 + 0.5\left(\sqrt{1+T_C} - 1\right) + \frac{T_C}{4(2+T_C)} \tag{3.12}$$

Factors influencing σ_e are the number of blades B_P, the average blade chord c_P, the propeller diameter D_P and the blade chord lift gradient $C_{l_{\alpha,P}}$. It is, in essence, indicating how 'obstructive' the presence of the propeller geometry is in the total circular area enclosed by the propeller perimeter. The propeller advance ratio J is a non-dimensional value relating V_∞ to the propeller $\mathrm{rpm}\ n$. Lastly the thrust factor f is only changing with the thrust coefficient T_C of Equation 3.13.

$$T_C = \frac{8}{\pi J^2} \frac{T}{\rho n^2 D_P^4} \tag{3.13}$$

The resulting system of equations shows the value for the normal force gradient ($C_{N_\alpha} = \mathrm{d}C_N/\mathrm{d}\alpha_P$) is increasing with a higher propeller solidity, an increased advance ratio and an increase in thrust. The lift coefficient due to normal force C_{L_N} can then be determined for any flight condition by multiplying with the angle of attack of the propeller α_P. Generally this is equal to the angle of attack of the aircraft except for the case where the propeller is installed under incidence. Together with the vertical component of thrust the normal force is included to account for the propeller forces and will play a role in determining the performance of the aircraft in power-on conditions.

3.1.3. Design Limitations

The choice for propellers is expected to be beneficial for propulsive efficiency but imposes limitations on the design as well. Higher efficiency is achieved by increasing the propeller diameter to allow more air to be accelerated less. However, the size of the propeller is typically restricted by a combination of the following three items:

- propeller blade tip speed;
- structural limits of the propeller blade;
- clearance of the propeller.

Out oft these, according to Roskam, the propeller blade tip speed is most limiting the diameter of the propeller. This tip speed is limiting the design as high-transonic tip speeds decrease the efficiency of the propeller by introducing shock waves to the propeller. To avoid this from happening the tip Mach number M_{tip} is limited in Equation 3.14 determining propeller diameter. [26]

$$D_P = \sqrt{\frac{a^2}{\pi^2 n^2}\left(M_{\text{tip}}^2 - M_\infty^2\right)} \tag{3.14}$$

Where the atmospheric conditions are included by means of the speed of sound a and the Mach number M_∞. The propeller diameter is following from the aforementioned value of M_{tip} for a certain set propeller rotational velocity of n.

The other concern of employing propellers on the aircraft stem from the clearance between propeller and aircraft frame and propeller and ground. The certification specification of the European Aviation Safety Association (EASA) for large aircraft (CS-25) state the following regarding these propeller clearances in CS 25.925: [17]

- a: Minimum 18 centimeters between propeller and ground in level take-off;
- c1: Minimum 25 millimeters radial clearance between the propeller tip and aircraft structure;
- c2: Minimum 13 millimeters longitudinal clearance between the propeller tip and aircraft structure.

In the employed tool for aircraft design and assessment these requirements are included, more on this in Chapter 4. These requirements all present a minimum of clearance stemming from requirements which do not necessarily account for performance degradation following from poor propeller positioning. For this, some design guidelines are obtained from the aircraft design collection of Roskam. [26] These guidelines recommend to maintain a radial clearance between propeller and fuselage equal to at least 40 inches (approx. 1m), mainly for noise considerations in the cabin. Furthermore a longitudinal clearance should be present equal to a value between a quarter and a full chord length to prevent strong loading of the propeller blades due to the close proximity to the wing leading edge. [21]

3.2. Slipstream Geometry

This section identifies the geometry of the slipstream where the focus before was purely on the propeller forces and the propeller performance. The final result from ADT is the system of equations allowing one to determine the velocities at each station in the control volume. The flow characteristics are known for the station downstream of the propeller. Theory behind the methods used to determine the slipstream geometry aft of any propeller are shown, first for the top and side views in Sections 3.2.1 and 3.2.2 before the total affected surface area is determined in Section 3.2.3

3.2.1. Top View

From the ADT of Figure 3.2 and using Equation 3.1 it is apparent that in order to allow equal mass flux at increased velocity, the slipstream diameter is reduced downstream of the propeller. As shown before the velocity at the propeller is the average of the velocity upstream and downstream, resulting in the final contracted slipstream diameter D_S represented by Equation 3.15. [26]

$$D_S = D_P\sqrt{\frac{V_\infty + \Delta V/2}{V_\infty + \Delta V}} = D_P\sqrt{\frac{V_\infty + \Delta V/2}{V_S}} \tag{3.15}$$

The main assumption is this contracted slipstream is constant in diameter in the region downstream of the propeller, neglecting slipstream degradation in this region. The resulting slipstream is presented in the top view in Figure 3.3. Here the actuator disk geometry of Figure 3.2 is clearly identifiable in proximity of the propeller.

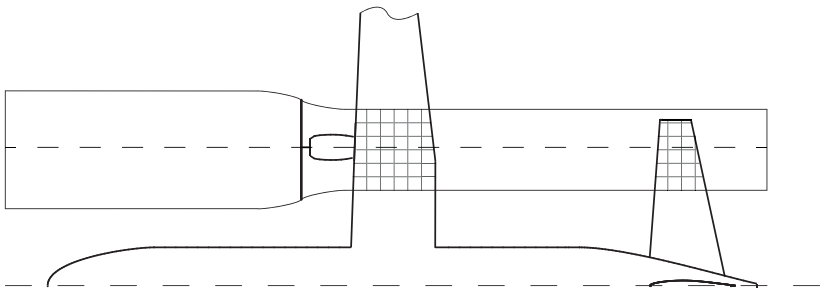

Figure 3.3: Top view of slipstream impacting main wing and horizontal stabilizer

The flow velocity in the slipstream V_S is, from the assumptions, constant as well. The amount of slipstream contraction is corresponding to the difference in flow velocities and as such will be more present in high-thrust, low free stream velocity conditions.

3.2.2. Side View

Whether or not a lifting surface is affected by the slipstream does not just depend on the top geometry presented before. The second component of the slipstream geometry is the deflection of the slipstream downwards. This deflection may result in the stabilizer remaining clear of the direct propeller slipstream and is shown for a typical high wing configuration in Figure 3.4.

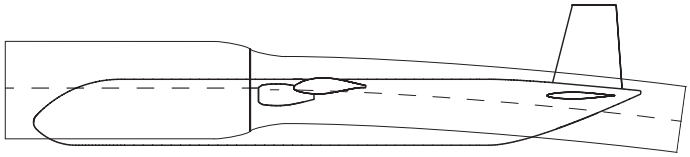

Figure 3.4: Side view of slipstream impacting main wing and horizontal stabilizer

The total angle of deflection for the slipstream is defined as the flow deflection due to propeller normal force. This follows from Section 3.1.2 where the propeller normal force is determined. The normal force deflects the angle of the slipstream θ_S according to Equation 3.16, presented by Alba et. al [2] as the isolated slipstream deflection.

$$\theta_S = \frac{\mathrm{d}\theta_S}{\mathrm{d}\alpha_P}\alpha_P \tag{3.16}$$

Where the gradient of slipstream deflection angle is given by Equation 3.17.

$$\frac{\mathrm{d}\theta_S}{\mathrm{d}\alpha_P} = \frac{1+T_C-\sqrt{1+T_C}}{2+T_C} + \frac{3+2T_C+\sqrt{1+T_C}}{(2+T_C)^2}\cdot\frac{\sqrt{1+T_C}}{4}\cdot\left.\frac{\mathrm{d}C_N}{\mathrm{d}\alpha_P}\right|_{T_C=0}\frac{8}{\pi J^2} \tag{3.17}$$

Here the normal force gradient $\frac{\mathrm{d}C_N}{\mathrm{d}\alpha_P}$ of Equation 3.9 is evaluated at $T_C = 0$ to obtain the power-off normal force gradient. This gradient is multiplied with the factors containing T_C to determine the gradient of θ_S with respect to the propeller angle of attack α_P. As with the normal force, the resulting deflection is only significant in case of a substantial angle of attack for the propeller.

3.2.3. Affected Wing Section

With both the top and side geometry quantified the total affected area of the lifting surface can be determined. In case the slipstream is symmetrically aligned with the lifting surface the total width of the affected wing section is equal to the contracted slipstream diameter. This situation is rare as the downward deflection and engine placement usually result in a partial slipstream covering the lifting surface as has been illustrated by Bouquet & Vos with Figure 3.5.

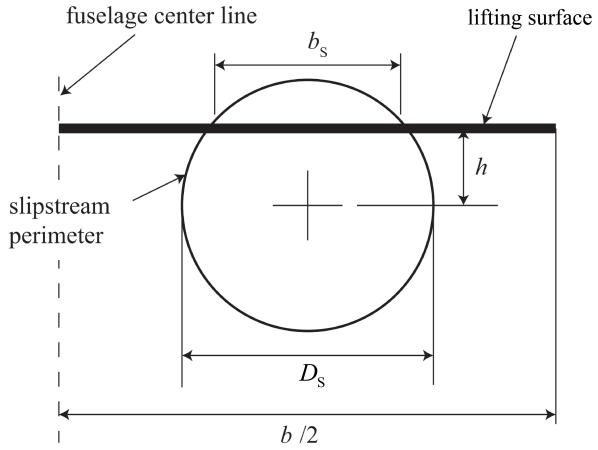

Figure 3.5: Geometry of slipstream impacting horizontal stabilizer. Adapted from [10]

The final span enclosed in the slipstream geometry is denoted as b_S and depends on the slipstream diameter D_S and the offset h through Equation 3.18.

$$b_S = D_S \sqrt{1 - \left(\frac{2h}{D_S}\right)^2} \tag{3.18}$$

The total distance h is a combination of multiple effects. The first is the geometric separation between surface and propeller axis. Next the angle of attack of the aircraft results in a change in horizontal stabilizer position. Finally the deflection of high-lift devices is influential in determining the total distance h of Equation 3.19. [10]

$$h = Z_H - Z_P - l_H \sin\alpha + l_H^* \sin\theta_S - (x_{\bar{c}/4} - x_P) + c_f \sin\delta_f + 0.25(x_{\bar{c}/4} - x_P)\sin\Delta\alpha_{0,f} \tag{3.19}$$

With Z_H and Z_P denoting the horizontal stabilizer and propeller vertical position, respectively. The distance between wing and tail mac l_h and the distance between wing trailing edge and tail l_h^* are present to account for a shift in position with angle of attack. The term $x_{\bar{c}/4} - x_P$ is relating the longitudinal position of the propeller with the reference point, taken as the quarter-chord mac. Next the second-to-last term of Equation 3.19 is accounting for (a possible) flap deflection of the preceding wing surface by relating flap chord c_f with flap deflection δ_f. Finally the term including the change in zero-lift angle of attack due to flap deflection $\Delta\alpha_{0,f}$ is presented to account for the wing upwash and a reduction of slipstream deflection.

The shown theory relates the results of Section 3.1, notably the propeller sizing and slipstream velocity, to the geometry of the slipstream. This allows the determination of the affected area to include the power-on effects in later methods. The influence of these power-on effects is shown next in Section 3.3.

3.3. Influence of Slipstream

The previous theory presented is applied in the effectiveness of lifting surfaces. This effectiveness is regarding the aerodynamic performance of the lifting surface and is defined by two parameters, apart

from the geometry of the surface. These are the angle of attack α and the dynamic pressure q, both combine in the determination of lift according to Equation 3.20.

$$L = q\left(C_{L_\alpha}\alpha\right)S \tag{3.20}$$

An increase in either, for a given lift gradient C_{L_α} and surface area S, will result in an increase in lift. Similarly a certain required lift is achieved for a lower α or q, allowing the design to account for this. The determination of both q and α are presented next for a lifting surface.

3.3.1. Dynamic Pressure

The dynamic pressure q is provided in Equation 3.21 and relates (local) flow velocity V with the atmospheric density ρ.

$$q = \frac{1}{2}\rho V^2 \tag{3.21}$$

In the framework of the research, the influence of the dynamic pressure is presented as a consequence of the increased flow velocity in the propeller slipstream. As such the parts of the lifting surfaces that are (partially) submerged in the slipstream will experience an increase in dynamic pressure. This in turn results in an increase in lift of the submerged section, provided all other variables of Equation 3.20 are constant. The increase in lift can either be beneficial or detrimental to the overall longitudinal stability and equilibrium of an aircraft depending on the design configuration of the aircraft.

3.3.2. Angle of Attack

The angle of attack of a lifting surface is important in assessing the lift of this surface. With the previously presented propeller and slipstream influences on the flow direction it is apparent this angle of attack will be determined to a certain extent by these power-on effects. In general for any lifting surface Equation 3.22 presents the final angle of attack $\alpha_{\text{surf.}}$.

$$\alpha_{\text{surf.}} = \alpha + i - \epsilon - \theta_S \tag{3.22}$$

Where the angle of attack of the aircraft α and the incidence angle i apply to any lifting surface. The last two influences constitute of the preceding downwash ϵ and the deflection of the slipstream θ_S. The definition of these angles is downward negative, opposite to the angle definition of α and i.

Out of these angles the determination of the downwash angle has not been presented. This downwash angle ϵ is only accounted for in case a preceding lifting surface is present and is a result from the lift force generated by the surface. Analogous to the presented slipstream deflection downward due to normal force, this lift force impacts ϵ as given by Equation 3.23. The method employed is an adaptation by Obert of lifting line theory (LLT) and follows from equating outgoing momentum of this control volume to the lift force. [23]

$$L = \dot{m}V\sin\epsilon \tag{3.23}$$

Where $\dot{m}$ denotes the mass flow through the control volume. For an isolated wing without propeller influence this control volume is the circle with diameter equal to wing span b, providing the enclosed area in Figure 3.6 and subsequently Equation 3.24 for the lift of the wing without power-on effects.

$$L_W = \rho\frac{\pi}{4}b^2V_\infty^2\sin\epsilon \tag{3.24}$$

To obtain the average downwash angle ϵ the lift of the surface L and the free stream flow velocity V need to be known, as well as the aircraft altitude to determine air density ρ. These values are determined for the lifting surfaces using Athena Vortex Lattice (AVL), an open source vortex-lattice method (VLM) available from Drela. [15]

Power-on effects are included by means of a similar analysis, taking the contracted slipstream diameter D_S and the position of this slipstream to determine the downwash angle for the wing section affected by

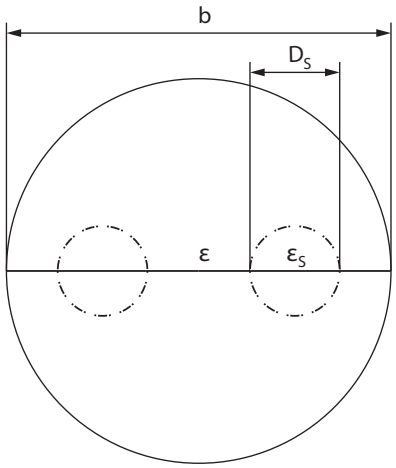

Figure 3.6: Overview of downwash control areas for wing with two propeller slipstreams. Adapted from Obert [23, Appendix IV]

the propeller slipstream. The downwash angle of the wing section immersed in the propeller slipstream ϵ_S is derived from Equation 3.23 to obtain Equation 3.25, provided by Bouquet. [10]

$$L_S = n_e \cdot \rho \frac{\pi}{4} D_S^2 V_S^2 \sin \epsilon_S \tag{3.25}$$

Where n_e is the number of engines under consideration. The total lift of a full wing with power-on effects is therefore a combination of Equation 3.24 and Equation 3.25 to obtain Equation 3.26.

$$L_{W+S} = \rho V_\infty^2 \left(\frac{\pi}{4} b^2 - n_e \frac{\pi}{4} D_S^2 \right) \sin \epsilon + \rho V_S^2 \left(n_e \frac{\pi}{4} D_S^2 \right) \sin \epsilon_S \tag{3.26}$$

Which is effectively subtracting the propeller slipstream(s) from the wing's outgoing momentum flow before adding the slipstream momentum of the propeller(s). Equation 3.26 will be used to determine the wing lift in the affected region. The unknown is L_{W+S} with ϵ obtained from the power-off lift of the wing surface. For this power-off lift several tools exist which will be further presented in the methodology in Chapter 4. The other variables apart from the slipstream downwash ϵ_S are all known by means of previously presented theory.

Bouquet proves the estimation by Obert for this ϵ_S by assuming the lift in the affected wing section relates to a wing in free flow with an airfoil section equal to the wing airfoil with deflected flaps holds true, showing Equation 3.27 as a result.

$$\sin \epsilon_S = \frac{2 C_{L_{\alpha_{S,\text{eff}}}}}{\pi A_s} \tag{3.27}$$

This equation is a direct application of LLT. Important here are the effective lift curve gradient $C_{L_{\alpha_{S,\text{eff}}}}$ in the slipstream region, determined using empirical NACA data. [12] The effective aspect ratio of the wing section affected, $A_{S_{\text{eff}}}$, is provided by Bouquet as Equation 3.28. [10]

$$A_{S_{\text{eff}}} = A_S + (A_W - A_S) \left(\frac{V_\infty}{V_S} \right)^{A_W - A_S} \tag{3.28}$$

$$A = \frac{b^2}{S} \tag{3.29}$$

Where the aspect ratio of a wing is shown in Equation 3.29, reflecting wing slenderness. Similarly A_S is obtained from the submerged wing span of Equation 3.18 in Section 3.2, with the area defined using the average chord for this submerged wing section.

The final angle of attack of the lifting surface given by Equation 3.22 is now fully defined as a combination of geometric and aerodynamic angles. It is possible to predict this angle in order to assess the aerodynamic performance of the surface in both power-off and power-on conditions, even accounting for possible high lift device (HLD) deflection.

The full influence on aircraft longitudinal stability and equilibrium will be explained further next in Chapter 4, where the theory in this chapter is applied to the limits defining the longitudinal performance of the aircraft. These limits are then applied to determine an adequate size for the horizontal stabilizer, including both power-off and power-on effects.

4

Methodology

With the introductory chapters of this thesis presenting the research background and the position of the to-be-assessed RTP, this chapter aims to connect the theory to the employed methods. These methods are the implemented models in the Aircraft Design Initiator, the software framework in which the assessment of aircraft is performed. A general overview of the Aircraft Design Initiator is given in Section 4.1 before the sizing method is explained in depth in Section 4.2.

4.1. Initiator implementation

The main tool to be used for the research is the Aircraft Design Initiator, a preliminary physics-based aircraft design tool created at Delft University of Technology. The goal of the Initiator is to combine empirical design and analysis with low-fidelity analysis tools to assess aircraft designs based on a given set of top level requirements.

The Initiator follows an iterative design approach where it converges to a feasible design. A feasible design means the Initiator result is converged with performance and weight results consistent with each other and all top level requirements satisfied. This process is generalized to be displayed comprehensively in Figure 4.1. The method is a top-down approach where the sizing in Class I is performed using a pre-existing database of aircraft to determine initial weights. This feeds into a component-level weight sizing in Class II, taking into account the specifics of the aircraft configuration. It is at this point an initial geometry is created in order to assess the prerequisites for the aerodynamic and performance analysis of the aircraft.

The Class II.V sizing method features a detailed sizing of the main wing and fuselage and is coupled to the aerodynamic analysis to obtain the first level of convergence within the Aircraft Design Initiator. The second convergence checks whether final performance is a match with the top-level requirements to verify full convergence. It is after this full convergence that an aircraft design is obtained, featuring a detailed geometry and presenting performance by means of key performance indicators (KPIs).

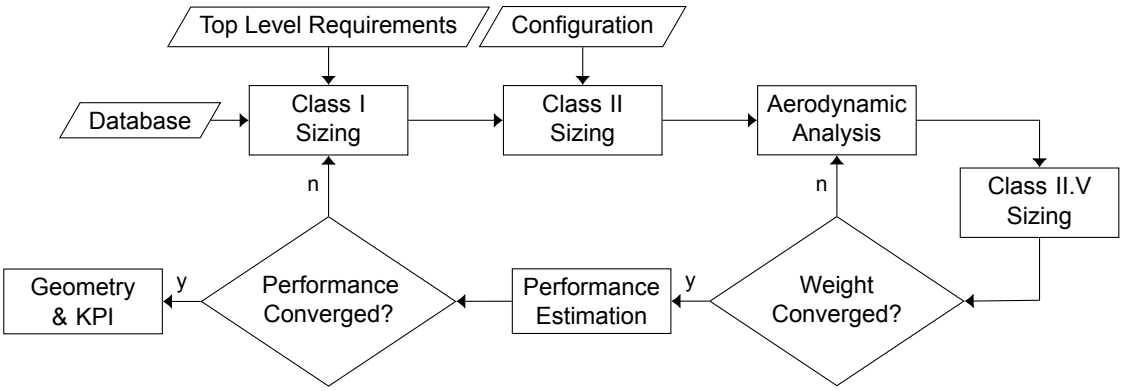

Figure 4.1: Overview of Aircraft Design Initiator process

Even though unconventional designs as blended wing body (BWB) and three-surface aircraft are able to be generated by the tool, the usage of empirical models may hinder in the analysis of these concepts. This also holds true for the envisioned RTP featuring large propeller engines in unconventional positions for which no database is present to be used in the convergence of the Initiator. This depicts how physics-based modules are preferred over empirical modules as they can be applied to unforeseen design choices. On top of this the very interaction between propeller effects and the horizontal stabilizer is expected to drive certain design parameters depending on configuration, requiring an implementation of slipstream and propeller effects in the Aircraft Design Initiator.

In terms of the converging Aircraft Design Initiator, the envisioned methods are implemented to influence the aerodynamic analysis and the performance estimation. It will alter the input for the Class II.V sizing method and may show that pre-converged aircraft are unfeasible designs when accounting for power-on effects, at which point a re-sizing is required. The main risk is how a significant discrepancy between the obtained performance and weight estimation relative to the database could exist, requiring additional iterations and as such computational effort. A strength of the Aircraft Design Initiator is the capability to output converged aircraft using fast and reliable methods, a feat that should not be lost by implementing more complicated design routines.

4.1.1. Existing Sizing Method

At the start of this thesis, three separate methods existed in the Aircraft Design Initiator to size the horizontal tail surface. These methods are:

- Tail volume coefficients (turboprop aircraft)
- Scissor plot sizing (turbofan aircraft)
- Custom sizing routines (exotic configurations)

The first is of special interest as this method of tail sizing relies on the use of tail volume coefficients, both for the horizontal and vertical tail surfaces. The tail volume coefficients for the horizontal tail is shown in Equation 4.1.

$$V_{HT} = \frac{l_H}{\bar{c}} \frac{S_H}{S} \tag{4.1}$$

Where the tail area ratio S_H/S is normalized using the tail arm l_H over the wing mac mac. It is important to state why this existing method is insufficient in sizing the envisioned RTP aircraft and, more generally, any propeller-powered configuration. The current implementation relies on a database of similar configurations, assuming a close connection exists between tail volume and the design choices. By relying on similarity the capabilities of the Aircraft Design Initiator to assess unconventional configurations is undermined, resulting in unreliable configurations at best and unfeasible designs at worst. The usage of tail volume coefficients should be limited to the Class I weight sizing where the sizing is fully empirical and as such does not warrant the use of more advanced methods.

The existing sizing for turbofan aircraft is most important as it provides the framework on which the turboprop stabilizer sizing is built. It relies on the generation of an aircraft scissor plot featuring limits for stability and control for a range of c.g. positions. Adaptations to the scissor plot sizing to account for power-on effects are explained next in Section 4.1.2 before the intricacies of scissor plot sizing are shown in Section 4.2.

The last sizing method features an adaptation of the limit sizing for highly unconventional aircraft. These aircraft include the ducted fan design of the Delft University Unconventional Configuration (DUUC) or a BWB configuration, both featuring no traditional empennage at all. [11, 28] These methods will remain in place for the sizing of such aircraft in the future.

4.1.2. New Sizing Method

As mentioned a previous implementation of scissor plot sizing is present in the Aircraft Design Initiator for turbofan aircraft. The new turboprop tail sizing method will expand on this implemented method by means of two main activities. First the existing module needs to be allowing for turboprop aircraft, requiring the existing method to be including turboprop engines as an option. Secondly the power-on effects need be included in order to account for the expected change in limits due to these effects. This concludes in the general work flow of the turboprop horizontal tail sizing method as described in Figure 4.2.

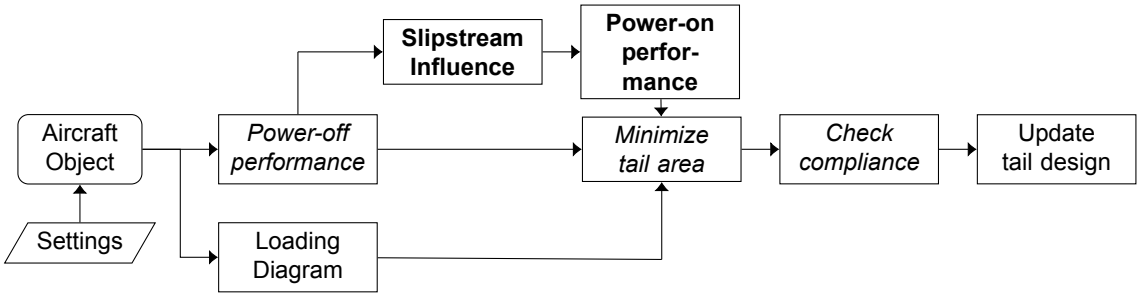

Figure 4.2: Overview of horizontal tail surface sizing method

Here the methods in *italic* present the modified components of the sizing method relative to the turbofan implementation. The methods in **bold** are newly implemented to account for the power-on performance in the final determination of the minimum required tail surface area. This power-on performance is stemming from the power-off performance directly where the effects on the local angle of attack α and dynamic pressure q, together with direct propeller forces, are included from the theory in Chapter 3.

Flow conditions from the power-off case are used to determine the propeller force and slipstream geometry. These initial flow conditions stem from the power-off analysis using the United States Air Force (USAF) Data Compendium (DatCom) and AVL to obtain aerodynamic properties of the main wing and horizontal stabilizer. In total six flight conditions are assessed: three aircraft settings and conditions for cruise, landing & takeoff, each assessed for power-on and power-off.

4.2. Scissor Plot Limits

The goal of the method depicted in Figure 4.2 is to minimize horizontal tail area while satisfying the limits imposed by longitudinal stability & equilibrium and aircraft rotation restrictions. To do so the aircraft scissor plot is created. A general example of such a scissor plot, featuring limits for one flight condition, is depicted in Figure 4.3 where the top filled area is the region where none of the shown limits are violated.

The limits shown are selected as they are typical limits present for conventional aircraft configurations. A number of potential scissor plot limits is not included for a variety of reasons. Examples of limits are the landing flare requirement and the aircraft maneuver point. These are not implemented for lack of an adaptive method to determine this limit for any aircraft configuration, thereby possibly limiting the applicability of the new scissor plot sizing. Additionally the sizing is performed using static limits only, not considering the steady-state aircraft dynamic stability requirements. Both additional static limits and the inclusion of dynamic stability have been investigated before by Q. Jansen. [20]

The final aircraft tail area ratio S_H/S as in Figure 4.3 is the main result of all implemented methods. It is determined by the relative position of these limits and the aircraft c.g. excursion. The next sections will describe the underlying equations for the construction of the scissor plot limits before the required aerodynamic coefficients are explained further in Section 4.3.

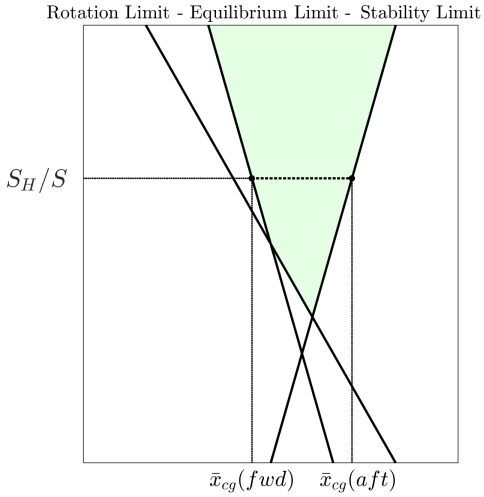

Figure 4.3: Example of aircraft scissor plot showing design area restricted by typical limits

4.2.1. Longitudinal Stability

The right-side bound in a typical aircraft scissor plot as shown in Figure 4.3 is defined by the longitudinal equilibrium of the aircraft. This stability is shown in the overview of Figure 4.4 for a conventional aircraft design.

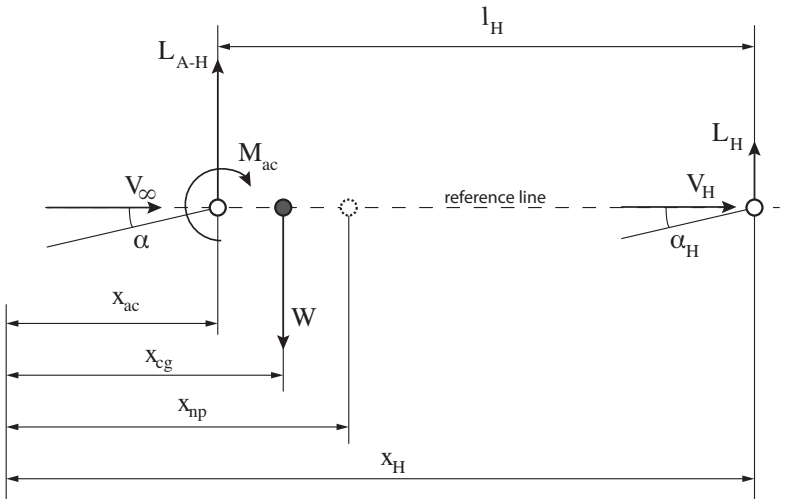

Figure 4.4: Overview of parameters influencing longitudinal stability. Adopted from [27, p. 308]

Here the function of the tail is to ensure the aircraft is level by introducing a lifting force L_H aft of the aircraft-minus-tail lift L_{A-H} to counteract the moment created by this latter lift, the aircraft weight force W and the pitching moment about the main wing aerodynamic center (a.c.). A longitudinally stable aircraft is one where any disturbance in this equilibrium, for instance a change in angle of attack due to a wing gust, is counteracted by the system of forces present. Equation 4.2 is able to describe the relation to obtain a satisfactory tail surface area.

$$\bar{x}_{cg} = \bar{x}_{ac} + \frac{C_{L_{\alpha_H}}}{C_{L_\alpha}}\left(1 - \frac{\mathrm{d}\epsilon}{\mathrm{d}\alpha}\right)\frac{S_H}{S}\frac{l_H}{\bar{c}}\left(\frac{V_H}{V}\right)^2 - \mathrm{SM} \tag{4.2}$$

With the goal of the method to minimize S_H/S for a given c.g. excursion, the equation is rewritten to output this value for the set of aerodynamic and geometric properties in Equation 4.3.

$$\frac{S_H}{S} = \left[\bar{x}_{cg} - (\bar{x}_{ac} - \mathrm{S.M})\right]\left[\frac{C_{L_{\alpha_H}}}{C_{L_\alpha}}\left(1 - \frac{\mathrm{d}\epsilon}{\mathrm{d}\alpha}\right)\frac{l_H}{\bar{c}}\left(\frac{V_H}{V}\right)^2\right]^{-1} \tag{4.3}$$

This linear equation is intersecting the x-axis of Figure 4.3 at the aircraft neutral point (n.p.), given by Equation 4.4.

$$\bar{x}_{\mathrm{np}} = \bar{x}_{\mathrm{ac}} - \mathrm{SM} \tag{4.4}$$

The longitudinal stability limit is restricting the aft movement of the aircraft c.g.. The static margin SM is included to design the tail surface to achieve static stability as opposed to neutral stability and is typically a few to ten percent of the aircraft mean aerodynamic chord. Current control system technology has allowed for the design of longitudinally unstable aircraft by means of a relaxed static margin. The application of non-reversible controls in aircraft allows an on-board controller to mimic the behavior of a stable aircraft and as such allowing the tail area ratio to decrease, increasing operational performance by saving on structural weight for the aircraft.

To obtain a minimal tail area ratio it is important to maximize the term in square brackets in Equation 4.3. With a selected main wing position the geometry of the aircraft is presumed fixed, meaning for a given aft c.g. the ratio of lift gradients, the downwash gradient and the tail velocity ratio are defining the longitudinal stability limit. This limit therefore is a metric of the rate of change in lift for a changing inflow angle of the lifting surfaces, whether this stems from external (gusts) or internal (slipstream) effects.

4.2.2. Equilibrium in Stall

An equal approach to the previous limit is taken where Figure 4.5 depicts the situation. Now the tail area ratio is defined by the maximum amount of lift this surface is able to generate in order to counteract the most unfavorable (i.e. largest in magnitude) aircraft-minus-tail pitching moment.

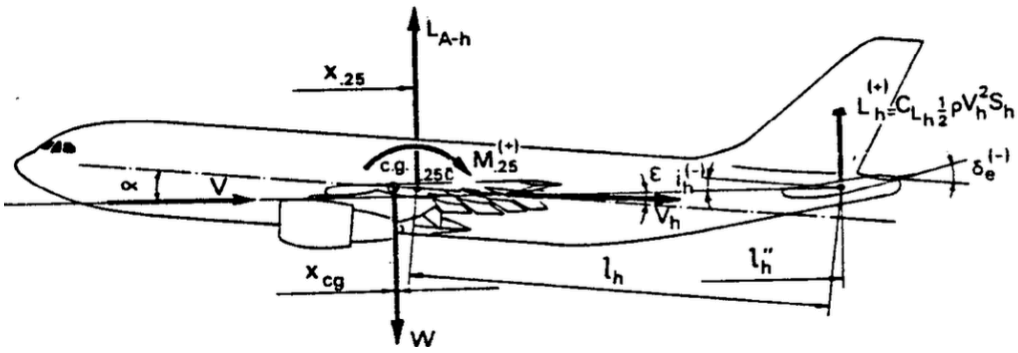

Figure 4.5: Overview of parameters influencing longitudinal equilibrium in landing stall. [27, p. 324]

Equation 4.5 relates to the stall control limit of the aircraft.

$$\bar{x}_{cg} = \bar{x}_{ac} - \frac{C_{m_{ac}}}{C_{L_{A-H}}} + \frac{C_{L_H}}{C_{L_{A-H}}} \frac{S_H}{S} \frac{l_H}{\bar{c}} \left(\frac{V_H}{V}\right)^2 \tag{4.5}$$

Similar to the stability limit, the relation is rewritten to be a linear function for S_H/S as shown in Equation 4.6.

$$\frac{S_H}{S} = \left[\bar{x}_{cg} - \left(\bar{x}_{ac} - \frac{C_{m_{ac}}}{C_{L_{A-H}}}\right)\right] \left[\frac{C_{L_H}}{C_{L_{A-H}}} \frac{l_H}{\bar{c}} \left(\frac{V_H}{V}\right)^2\right]^{-1} \tag{4.6}$$

This limit intersects the x-axis of Figure 4.3 at the point $\bar{x}_{ac} - {}^{C_{m_{ac}}}/_{C_{L_{A-H}}}$ and as such will be depending strongly on the pitching moment about the aerodynamic center $C_{m_{ac}}$. This provides the explanation to determine the takeoff and landing stall equilibrium and to omit the cruise condition. The pitching moment coefficient is expected to be significantly larger in these configurations compared to cruise, shifting the limit to the right in Figure 4.3 and resulting in a more restrictive limit. As was the case with the stability limit, the term in square brackets is proportional to the limit slope and an increase in this

term results in an increase of the design space. With given geometry, the forward c.g. is limited by the aforementioned $C_{m_{ac}}$ as well as the ratio of maximum lift coefficients and the tail velocity ratio. As such the limit is determining the high-lift requirement of the horizontal stabilizer and sizes this surface accordingly.

4.2.3. Rotation at Takeoff

The final limit under consideration is the requirement to rotate at takeoff, requiring (for conventional aircraft) a strong downward lift force to be generated by the horizontal stabilizer. An overview of this rotation run is represented by Figure 4.6.

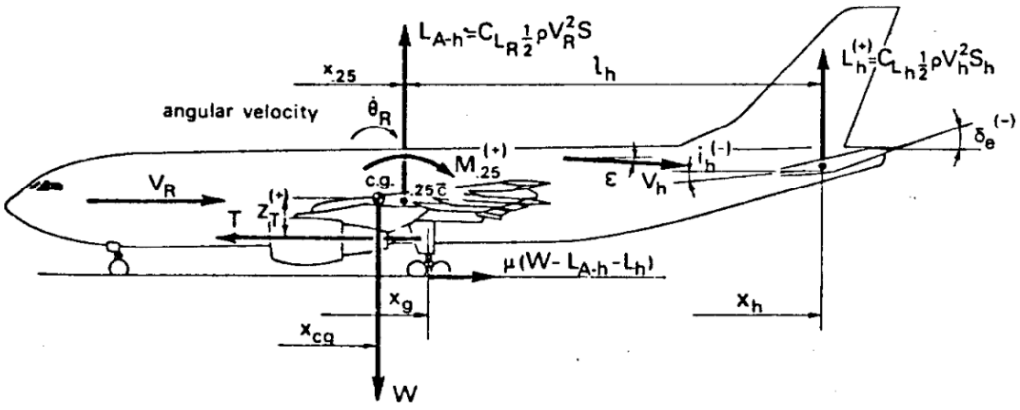

Figure 4.6: Overview of parameters influencing the takeoff rotation requirement. [27, p. 325]

The static analysis of the rotation at takeoff takes place at the point of rotation where the aircraft reached rotation velocity V_R. This velocity is taken relative to the aircraft stall speed V_S at the takeoff configuration as given by Equation 4.7

$$V_R = 105\% V_S = 1.05\sqrt{\frac{W}{S}\frac{2}{\rho}\frac{1}{C_{L_{\max}}}} \tag{4.7}$$

Where W is equal to the maximum takeoff mass (MTOM) times the gravitational acceleration g. Now Equation 4.8 shows the relation for takeoff rotation.

$$\bar{x}_{cg} = \bar{x}_{mg} - \bar{z}_T \sum \frac{T}{W} - \left\{\frac{C_{m_{ac}}}{C_{L_{\max}}} - \eta_h \eta_q \frac{C_{L_H}}{C_{L_{\max}}}\left[\frac{S_H}{S}\frac{l_H}{\bar{c}} - \frac{C_{L_R}}{C_{L_H}}(\bar{x}_{cg} - \bar{x}_{ac})\right]\right\}\left(\frac{V_R}{V_S}\right)^2 \tag{4.8}$$

This relation is similar to that for the stall equilibrium with two main differences. First of all, all moments are determined around the point of rotation which is no longer the aircraft c.g.. Instead the aircraft main landing gear position x_{mg} is required for this limit as the aircraft pivots about this point. Equation 4.8 includes two factors η. The first, η_h, accounts for the dynamic pressure over the tail surface by means of Equation 4.9.

$$\eta_h = \frac{\bar{x}_{cg} - \bar{x}_{mg}}{l_H}\left(\frac{V_H}{V}\right)^2 \tag{4.9}$$

Where the second factor η_q relates the tail lift capabilities to the desired rate of rotation $\dot{\theta}$ as shown in Equation 4.10.

$$\eta_q = 1 + \frac{C_{L_{\alpha_H}}}{C_{L_H}}\frac{\dot{\theta}_R(\bar{x}_{cg} - \bar{x}_{mg})}{V_R} \tag{4.10}$$

Take-off rotation is also influenced by the offset of the provided thrust relative to the c.g. as shown by the component $\bar{z}_T \sum {}^T/_W$. The value for $\bar{z}_T$ is negative for engines placed above the c.g., meaning

thrust counteracts the rotation at take-off. As for the equilibrium and stability limits, the limit is rewritten to represent the tail area ratio S_H/S in Equation 4.11.

$$\frac{S_H}{S} = \frac{\bar{c}}{l_H}\left\{\frac{C_{L_{\max}}}{\eta_h \eta_q C_{L_H}}\left[\frac{C_{m_{ac}}}{C_{L_{\max}}} - \left(\frac{V_R}{V_S}\right)^2\left(\bar{x}_{mg} - \bar{z}_T \sum \frac{T}{W} - \bar{x}_{cg}\right)\right] + \frac{C_{L_R}}{C_{L_H}}(\bar{x}_{cg} - \bar{x}_{ac})\right\} \tag{4.11}$$

This rotation relation contains multiple components influencing the total rotation performance of the aircraft. Important is the fact that, similar to control at stall, this limit creates a requirement for the tail maximum lift coefficient C_{L_H}. Clearly decreasing the distance between main gear and forward c.g. position will increase the design space of Figure 4.3 by moving the limit leftwards, although care needs to be taken as to not surpass the most aft c.g. position as doing so can result in aircraft tip-over during ground operation. A negative pitching moment $C_{m_{\text{ac}}}$, contributing to the longitudinal stability of the aircraft, is hindering rotation at take-off. Furthermore any engines positioned above the aircraft c.g. will negatively affect the rate of rotation of the aircraft.

The resulting set of equations encompass the scissor plot sizing method. Although all limits need not be violated in all flight cases, only the stability limit of Equation 4.3 is calculated for each flight phase at the most aft c.g. position. The Equation 4.6 equilibrium limit bounding the maximum lift requirement for the most forward c.g. limit is implemented for the take-off and landing setting as the low-speed high-lift nature of these flight phases are more limiting. Finally the requirement shown in Equation 4.11 is included to account for the lift requirement of the horizontal stabilizer to obtain adequate rotation during the take-off run.

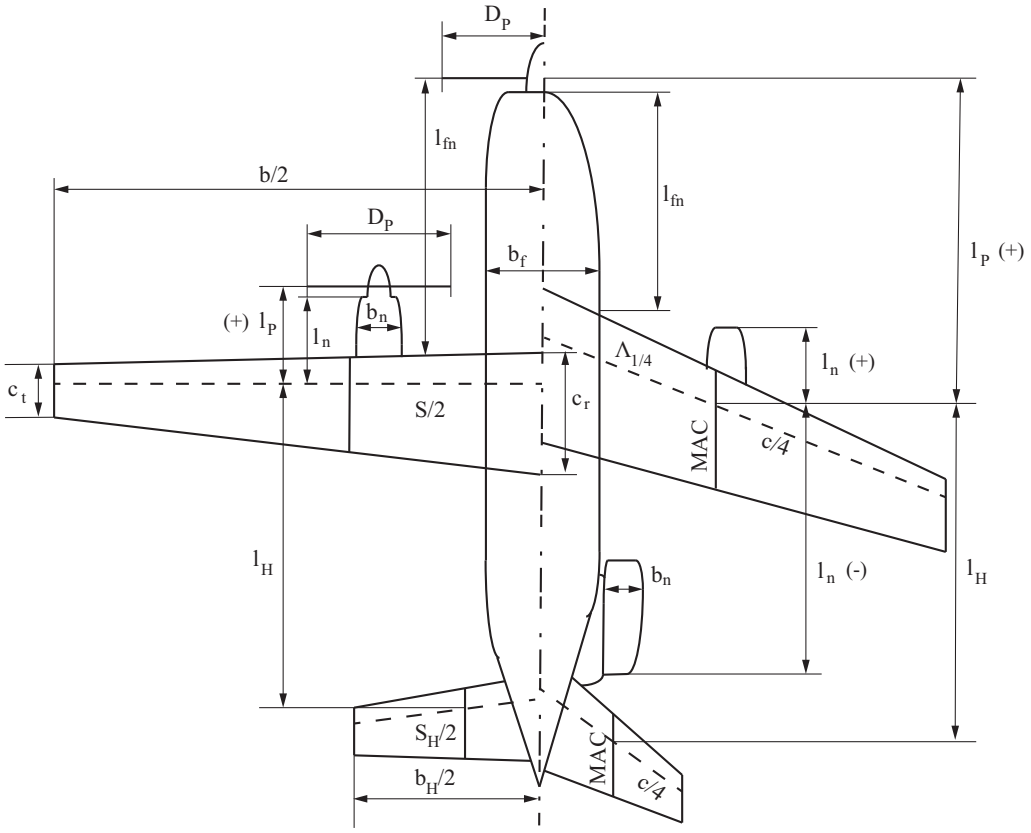

Figure 4.7: Aircraft geometry definitions. Adapted from Torenbeek [27, page 480]

4.3. Aerodynamic Coefficients

With all limits presented it is of importance to go into detail in explaining the behavior of the aircraft parameters influencing tail sizing. As such the effect of the propeller forces and slipstream on the

sizing of the horizontal stabilizer can be qualified by assessing the influence of these on the coefficients. Section 4.2.3 is shown for the distances and dimensions of components relating to the aircraft, showing sign definitions in the top-down view.

The list of aerodynamic coefficients used in the limits of the scissor plot is broken down in the following sections:

- Lift Coefficient and Lift Gradient
- Aerodynamic Center
- Pitching Moment Coefficient
- Velocity Ratio
- Center of Gravity

All will be discussed next, showing the methods used to obtain the values and the change of coefficient in the power-on analysis.

4.3.1. Lift Coefficient and Lift Gradient

The lift coefficient of a wing surface is important for the sizing explained before through the values directly and by means of the gradient C_{L_α} with respect to the angle of attack α.

Lift Coefficient

The power-off lift coefficient $C_{L_{\text{PO}}}$ is obtained from total lift determined by AVL for the lifting surface. This lift is normalized with dynamic pressure q and wing reference area S. Next the slipstream and propeller effects are included using Equation 4.12 to obtain the power-on lift coefficient.

$$C_{L_{\text{power}}} = C_{L_{\text{PO}}} + \Delta C_{L_S} + C_{L_T} + C_{L_N} \tag{4.12}$$

Where the three power-on effects are the thrust vector component parallel to the lift of the wing C_{L_T} (Equation 3.7), the lift coefficient due to propeller normal force C_{L_N} (Equation 3.9) and the slipstream lift increment ΔC_{L_S} (Equation 3.25).

For an unaffected wing surface, in case no engines are mounted to the surface and no slipstream is present, the power-on lift coefficient is unchanged from the power-off lift coefficient. In case of an engine mounted to the lifting surface, the increase in lift is proportional to the engine power P and inversely proportional to the cube of free stream velocity V. As such the increase in lift due to propeller forces is expected to be more influential in the low speed flow conditions of take-off and landing. The same holds true for the increase in lift in the slipstream. The flow velocity here is increased significantly with respect to the free stream velocity, resulting in a strong increase in dynamic pressure q and as such increased lift.

Lift Gradient

Together with the absolute value of the lift coefficient, the gradient with respect to the angle of attack α is expected to increase as well. This stems from the fact that both the lift due to propeller normal force and propeller thrust are scaling with this angle, resulting in a stronger addition at higher angles of attack. This is of importance for the stability limit of Equation 4.3 as the ratio of lift gradients ${}^{C_{L_{\alpha_H}}}/_{C_{L_\alpha}}$ is represented. The larger this ratio the less limiting this requirement is. As such one would increase the gradient of tail lift whilst leaving the main wing unaffected. In case both are affected, the expectation is such that the ratio will decrease. This can be explained by the absolute size of the lift gradients. As for both surfaces the lift coefficient is normalized with the main wing surface area, an equal relative increase will result in a larger absolute increase for the main wing lift gradient.

Maximum Lift Coefficient

For the main wing a maximum lift coefficient is implemented by means of an Aircraft Design Initiator setting. This setting is used as a starting value in sizing. For the horizontal stabilizer the maximum lift coefficient is depending on the type of tail surface. For a fixed stabilizer, as employed on turboprop aircraft, the maximum coefficient is empirically determined to follow Equation 4.13. [27]

$$C_{L_{H,\max}} = \pm 0.35\sqrt[3]{A_H} \tag{4.13}$$

The assumption made by Torenbeek is that the tail surface is symmetrical and able to generate lift in both directions of equal magnitude. In reality, tail surfaces for conventional designs are typically capable of providing more downward lift, provided this is the limiting case for a forward c.g. position. This can be done by either installing a tail under a certain angle of incidence or by using non-symmetrical airfoil profiles. For this research the first is assumed where the total range of attainable C_{L_H} is still provided by Equation 4.13, although the limit cases have been shifted to simulate the effect of stabilizer incidence. The resulting incidence is different per configuration and will be shown later for the RTP and reference aircraft.

4.3.2. Aerodynamic Center

All three scissor plot limits change relative to the aerodynamic center $\bar{x}_{ac}$. The total aircraft minus tail aerodynamic center a.c. is determined as a summation of the wing a.c. and the influence of aircraft components as provided in Equation 4.14.

$$\bar{x}_{ac} = \bar{x}_{ac_W} + \Delta_F \bar{x}_{ac} + \Delta_N \bar{x}_{ac} + \Delta_P \bar{x}_{ac} \tag{4.14}$$

Which sums the position of the main wing a.c. with the shift caused by the fuselage, the nacelle and the propeller.

Main Wing

The aerodynamic center of the main wing ($\bar{x}_{ac_W}$) is obtained empirically from Torenbeek Appendix E and is expected to be close the quarter-chord point of the mean aerodynamic chord mac. [27] The method does not allow to compensate for the shift in aerodynamic center due to the presence of power-on effects, which is why the following assumptions are made.

The sweep angle Λ of the wing is low (<10°) as the operational velocity of the aircraft is limited at moderate Mach numbers. These aircraft are operating below the transonic regime (M_∞ > 0.8~) where the application of sweep is beneficial in delaying compressibility effects resulting in an increase in drag. This low sweep angle assumption ensures the power-off a.c. of the wing is an accurate prediction for the power-on a.c. as any influence of the slipstream is expected to shift the a.c. lateral position only. The second assumption is that the propeller forces are not included in the determination of the clean wing as the influence of these is included in a separate term of Equation 4.14.

Fuselage

Presence of the fuselage results in a forward shift of the aerodynamic center, hence $\Delta_F \bar{x}_{ac}$ is destabilizing the aircraft. The effect of the fuselage is determined using the Engineering Sciences Data Unit (ESDU) empirical model of Equation 4.15.[3] According to Catalano this method is accurate to a couple percent-point for a variety of wing-fuselage combinations when compared to wind tunnel results.[13] The previous implementation of Torenbeek showed discrepancies between the theoretical a.c. position and the wind tunnel results of over 10% for certain wing-fuselage combinations. As the shift due to the fuselage is expected to greatly influence the longitudinal a.c. position, any method providing a greater accuracy is desirable.

$$\Delta_F \bar{x}_{ac} = \frac{c_r b_F^2 FG}{\bar{c} C_{L_\alpha} S}\left[1 + 0.15\left(\frac{h_F}{d_F} - 1\right)\right] - (K_1 + \lambda K_2) \tag{4.15}$$

Equation 4.15 shows the calculation of a shift forward (destabilizing) in a.c. position due to the presence of the fuselage. In this equation the equivalent wing root chord c_r, mac, fuselage width b_F, fuselage height h_F and wing reference area S are all geometric properties of the aircraft (see Section 4.2.3). The function constants F and K_1 are purely based on geometric properties and obtained from carpet plots provided by ESDU. Similarly, constants G and K_2 are obtained and do scale with free stream Mach number (M_∞) only. In power-on, the influence on the aircraft a.c. by the fuselage is decreased (less destabilizing) in case of a slipstream present because the wing lift gradient (C_{L_α}) will increase. As a result, the denominator of Equation 4.15 increases, reducing the forward shift of the a.c..

Nacelle

The a.c. shift due to engine nacelle $\Delta\bar{x}_{ac_N}$ is given by Equation 4.16, an empirical relation obtained from Torenbeek.[27]

$$\Delta_N \bar{x}_{ac} = \sum k_N \frac{b_N^2 l_N}{S\bar{c}C_{L_{\alpha,W+F}}} \tag{4.16}$$

Where the summation ensures the correction per each engine is added. The influence of the nacelles on the a.c. depends on the position of the nacelle relative to the quarter-chord mac l_N, defined in Section 4.2.3. Factor k_N is by definition negative so that engines aft of the quarter-chord point on the mac are a stabilizing contribution. This is equivalent to the effect of fletching on an arrow. The only power-on effect to be considered here is the wing-fuselage combined lift gradient $C_{L_{\alpha,W+F}}$ and this value is increased in power-on, assuming the influence impacts the main wing. Combined the nacelles are stabilizing when placed aft and destabilizing when located in front of the quarter-chord mac and the influence on the a.c. is magnified when including slipstream effects.

Propeller

The final component in the determination of the aircraft minus tail a.c. is the shift due to the propeller, denoted as $\Delta_P \bar{x}_{ac}$ in Equation 4.14. As one expects this contribution changes substantially between the power-off and power-on case. The influence is determined using Equation 4.17, accounting for the feathering of a propeller in power-off situations.[27]

$$\Delta_P \bar{x}_{ac} = -0.05 \sum \frac{B_p D_p^2 l_p}{S\bar{c}C_{L_{\alpha,W}}} \tag{4.17}$$

The contribution per engine scales with the number of blades B_p and the diameter of the propeller D_p. The effect is similar to that of propeller solidity σ presented before where the influence increases for propellers with a large amount of blades. The contribution is destabilizing in case the propeller is present in front of the quarter-chord mac as the value of l_P is defined to be positive in such a case. Therefore, propellers aft of the a.c. of an aircraft will shift the a.c. aft. In case of power-on this propeller effect on the a.c. is absent and the effect of propeller thrust and normal force are included in other components of the tail sizing limits.

Total

Finally, by applying Equation 4.14 the total aircraft minus tail a.c. position is determined for the aircraft. A typical position for an isolated wing a.c. is around the quarter-chord mac position. From here the fuselage is shifting the a.c. forward, an effect that can be countered slightly by the presence of a main wing propeller slipstream increasing the lift gradient of the wing-fuselage combination. The position of the engines is crucial as well, where aft positioned engines and propellers are shifting the a.c. aft. This effect scales with the lift gradient of the wing-fuselage combination for the nacelles where the propeller itself is not adding a contribution directly in case of normal operation.

Applying the a.c. position to the limits of Figure 4.3 a further aft a.c. allows the stability limit of Figure 4.3 to shift to the right, allowing for a potentially lower tail surface area ratio by shifting the n.p. further aft. Contrasting to this is the effect on the stall equilibrium limit and rotation requirement. Here, a further aft a.c. limits the design space by shifting the limits to the right, requiring a trade-off between both sides of the scissor plot limits.

4.3.3. Pitching Moment Coefficient

The aircraft minus tail pitching moment about the a.c. $C_{m_{\text{ac}}}$ is determined as a summation of factors as presented in Equation 4.18 Standard sign convention is defined as negative for a nose-down pitching moment.

$$C_{m_{ac}} = C_{m_{ac,W}} + \Delta_F C_{m_{ac}} + \Delta_N C_{m_{ac}} + \Delta_{HLD} C_{m_{ac}} \tag{4.18}$$

Similar to the determination of the a.c., the pitching moment is a summation starting from the main wing contribution. The result is the aircraft-minus-tail total pitching moment coefficient that can be applied to the limits of the scissor plot sizing to determine the horizontal stabilizer contribution.

Main Wing

The starting point is the clean wing pitching moment $C_{m_{\text{ac},W}}$. This value is determined using the USAF DatCom.[18] This collection of methods is created to, among others, assess performance of lifting surfaces. The wing pitching moment about aerodynamic center is by definition not different per flight phase as it is determined for the clean wing (no deployment of HLDs) at zero lift.

The power-on effects on the pitching moment of this wing are limited to only include the increase in dynamic pressure q in the slipstream as direct propeller forces have been implemented in the surface lift coefficient before. The method employed is a collection of equations presented by T. Bouquet who was able to verify the applicability of the equations by means of wind tunnel tests. The final result to determine the effect of slipstream on a clean wing is shown in Equation 4.19. [9]

$$C_{m_{S,0}} = n_e \frac{D_S c_S}{S} C_{m_{0,S}} \left[\left(\frac{V_\infty + \Delta V}{V_\infty} \right)^2 - 1 \right] \tag{4.19}$$

This gives the change in pitching moment coefficient at zero angle of attack for a clean wing with slipstream present, $C_{m_{S,0}}$. The equation presented is including the slipstream geometry in D_S and c_S together with the wing reference area S. The total contribution is performed per engine and will be a negative pitching moment contribution in case the increased flow velocity of the slipstream, ΔV, is present. The assumption made here is that any increase in lift due to the slipstream is applied at the quarter-chord of the influenced wing section. In reality the a.c. of the clean wing will be close to this point, allowing for this simplification.

Fuselage

The effect of the fuselage on the pitching moment is determined using Equation 4.20 from Torenbeek.[27]

$$\Delta_F C_{m_{ac}} = -1.8 \left(1 - \frac{2.5 b_F}{l_F} \right) \frac{\pi d_F h_F l_F}{4 S \bar{c}} \frac{C_{L_0}}{C_{L_{\alpha,W+F}}} \tag{4.20}$$

Where fuselage dimensions b_F, h_F and l_F are included as geometric properties of the aircraft, together with the wing reference area S and the mac $\bar{c}$. The wing lift coefficient at zero angle of attack C_{L_0} is obtained from the wing lift gradient presented before. This value is affected by flight phase and power setting together with the wing-fuselage lift gradient $C_{L_{\alpha,W+F}}$. Since the ratio of C_{L_0} over $C_{L_{\alpha,W+F}}$ both change with this gradient the net effect of the power-on condition on the pitching moment coefficient is minimal.

Nacelle

The third component of Equation 4.18 $\Delta_N C_{m_{ac}}$ accounts for the engine position and its contribution is a constant depending on the vertical distance between aircraft c.g. and nacelle. In case the nacelle is below the aircraft c.g. the contribution is nose-down and equal to -0.05. In case the nacelle is present above the c.g. the pitching moment coefficient is increased by 0.02. [27] In general this effect is of minor influence on the total aircraft pitching moment coefficient and is unaffected by power-on effects.

High Lift Devices

The final contribution to the pitching moment coefficient is due to the presence of HLDs. This contribution is included for the take-off and landing configuration and needs to be determined for power-on and power-off conditions. The contribution is implemented from Torenbeek [27, App. G] and determines the flap contribution on wing pitching moment. This contribution induces a strong negative pitching moment coefficient due to the flap placement aft of the a.c. Only for highly swept wings with inboard flaps this negative contribution diminishes or may indeed rise to a pitch-up effect on the aircraft.

The differentiating factor between power-off and power-on is the position of the aircraft a.c. In power-on there is a contribution to the pitching moment by the slipstream impacting the deployed flaps. This influence is given by Bouquet as Equation 4.21. [9]

$$C_{m_{S,\Delta\text{HLD}}} = \frac{c'}{c}\left(-0.25 + 0.32\frac{c_f}{c}\right)\left[1 + 0.2\left(1 - \sqrt{2\sin\delta_f}\right)\right]\Delta C_{L_{S,0}} - 0.25\left(\frac{c'}{c} - 1\right)\Delta C_{L_{S,\alpha}} \tag{4.21}$$

The first term is to account for the addition of lift away from the quarter-chord point due to the deflection of the flap δ_f, relating the chords defined by Figure 4.8. The final term is accounting for the change of this chord with the change in angle of attack. Both changes in lift coefficient $\Delta C_{L_{S,0}}$ and $\Delta C_{L_{S,\alpha}}$ stem from the increase in lift due to the propeller slipstream ΔC_{L_S}. The values have been separated to account for the effect of lift offset and an increase in angle of attack, respectively.

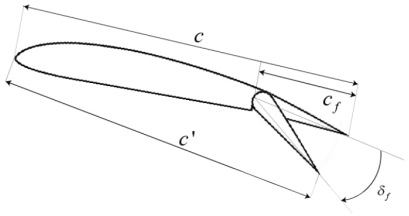

Figure 4.8: Chord definitions for deflected flap. [9, p. 25]

It should be noted that Equation 4.21 is an addition to Equation 4.19 and as such both need be evaluated for the main wing in all flight conditions.

Total

The final pitching moment coefficient will, taking into account all aforementioned effects, show the following trend for Equation 4.18. The power-on effect will be mostly present for situations where the total lift coefficient is increased due to the presence of HLDs. As such the landing and take-off condition will show a strong increase in nose-down pitching moment where the cruise condition will not show significant changes between power settings due to the absence of HLDs.

4.3.4. Horizontal Tail Velocity Ratio

A final and significant contribution to the effectiveness of the horizontal stabilizer and as such influential to the limits of Figure 4.3 is the velocity ratio V_H/V. This ratio is present in each of the scissor plot limits and effectively accounts for the relative dynamic pressure of the lifting surfaces.

The method presented by Torenbeek is to determine the type of horizontal tail present on the aircraft to set the ratio to a fixed value based on reference aircraft. For a T-tail configuration the ratio is assumed to equal $1.0\sim$, denoting the absence of main wing influence on the tail free stream velocity. A more conventional tail design is approximated with a velocity ratio of $0.85\sim$. [27]

For the power-on situation the tail velocity ratio can be one of the dominating influences on tail sizing limits. This is because the velocities in the contracted propeller slipstream can be significant as shown in Chapter 3. The expectation is values of over twice the free stream flow velocity in low speed, high thrust situations are not uncommon, showing the velocity ratio can seriously affect all limits shown in Equations 4.3, 4.6 and 4.11.

4.3.5. Center of Gravity

The final tail area ratio of Figure 4.3 is dependent on the total c.g. excursion of the aircraft. This excursion is the range between the two extreme bounds in which the aircraft c.g. exists. These bounds are defined using a loading diagram where the aircraft operating empty mass (OEM) is increasing with passengers, cargo and fuel mass to end up at the MTOM. A typical example of a 2-2 seating layout aircraft is presented in Figure 4.9. Here one sees that the final forward and aft c.g. limits are obtained from the aircraft loading phase. The shift during the maximum payload mission is minimal in this example, depicted by the close-to-vertical fuel line. For typical aircraft it is not uncommon to impose additional limits on the c.g. by providing aircraft loading instructions. Such additional limits decrease the excursion for which the horizontal stabilizer should function and as such allow for an even smaller surface.

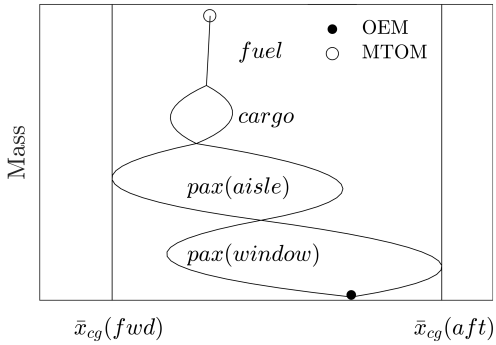

Figure 4.9: Typical aircraft loading diagram showing most forward and most aft c.g. limits

The final c.g. excursion is determined in a tail optimizer which varies the position of the main wing. The wing position that results in the lowest value of the tail area ratio S_H/S is selected. This process is presented by Figure 4.9, showing the final (optimum) position together with two more displaced wing positions.

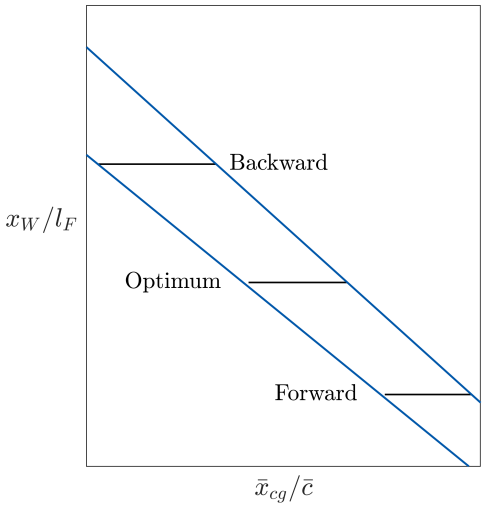

Figure 4.10: Aircraft c.g. excursion versus main wing position relative to fuselage length

For the final position, the module once more determines the limits of the scissor plot and checks whether the selected tail area ratio does satisfy all conditions set. The influence of shifting the main wing is significant as it results in a shift of the main gear and fuel, assuming both are integrated with the main wing. This means that the more backward position of the main wing shown in Figure 4.10 results in a far larger c.g. excursion. One aims to minimize this excursion in order to allow for the smallest possible tail surface area as presented with Figure 4.3. Note that the optimizing for main wing position is performed irrespective of power setting, resulting in the final c.g. limits and excursion.

For this final c.g. excursion all limits presented for stability, equilibrium and rotation are evaluated (Equations 4.3, 4.6 and 4.11). The result is a tail surface ratio S_H/S satisfying all limits. Longitudinal stability is restricted by the most aft c.g. position when an aircraft typically requires positive tail lift. The equilibrium limit is where, due to the high lift devices, a high nose-down pitching moment needs to be balanced with the downforce from the horizontal stabilizer. The most forward c.g. is limiting here as for conventional aircraft layouts the weight of the aircraft is offering the least relief on the nose-down pitching moment, requiring the stabilizer to produce a large counteracting moment. Similarly the rotation limit is assessed at the least favorable forward c.g. limit as here the aircraft weight provides the least assistance in providing a nose-up rotational speed.

4.4. Power-on Effects on Scissor Plot Limits

Summarizing the effect of including propeller slipstream effects some observations are made for conventional aircraft, assuming . Assuming that lifting surfaces are affected by the propeller forces and slipstream, the lift curve slope for components increases. This lift curve slope is employed in numerous methods. The ratio of the lift curve slope can adversely influence the limit for static stability, whereas the indirect influence is present in the determination of the total aircraft-minus-tail a.c. The a.c. shifts aft for increasing lift gradient and for nacelles and propellers aft and above the c.g. The a.c. defines the starting point of the stability and equilibrium limits in the scissor plot and a balance between stability and equilibrium at high lift needs to be struck.

The nose-down pitching moment $C_{m_{ac}}$ strongly increases with flap deflection and the influence of the slipstream on the wing section. Furthermore with the aft shift in a.c. the total tail load for longitudinal equilibrium at stall is expected to be more negative. This lift is bound by the maximum lifting capacity of the surface, showing the needs to counteract the strong nose-down effects.

The rotation limit is expected to be critical only in case the landing gear position is placed significantly rearwards in terms of mean aerodynamic chord mac. For such a case the download from the tail to ensure rotation speed is expected to be larger than the download to ensure equilibrium in low-speed high-lift conditions due to the aircraft weight force counteracting the nose-up pitching.

A propeller slipstream impacting the lifting surfaces results in a drastic dynamic pressure increase which is favorable for the slope of all scissor plot limits. For aircraft with engines mounted in close proximity to the horizontal stabilizer the effect on this surface is greatly beneficial, resulting in an expected power-off critical tail sizing. For aircraft where the stabilizer is unaffected the power-on case will not benefit from the dynamic pressure effect and equilibrium will be determined by the power-on scenario due to the main wing lift gradient increase.

From analysis of the aerodynamic coefficients one may conclude that aft placement is therefore beneficial in aircraft design, however, the c.g. excursion of such a configuration will be larger than that of a similar design with wing-mounted engines. This can be directly attributed to the weight of these engines acting aft on the aircraft together with a decrease of l_H due to a wing shift aft. This wing shift is required to counteract this aft weight contribution, resulting in an increase in tail size. A full comparative overview is presented for the RTP in Chapter 6 where the expectations stated here will be tested.

5

Method Verification & Validation

This chapter starts with the verification of the slipstream effects in the aircraft Initiator. It shows the method results follow logically from the presented methods in Chapter 4 and as such the propeller effects are implemented correctly. The second part of this chapter is concerned with the validation of the end result, a design generator which accounts for these slipstream effects to obtain feasible and converged aircraft designs.

5.1. Verification of Horizontal Stabilizer Sizing

For the verification of the slipstream methods two different aircraft are used. The ATR72-600 is selected as a typical existing turboprop aircraft featuring a T-tail layout. As a second aircraft the Fokker 50 is chosen as it features a conventional tail layout. This selection is capable of showing the influence of propeller and slipstream in case the slipstream is impacting the horizontal stabilizer and in case the stabilizer is clear of direct slipstream influence. Note that names of aircraft assessed by the Initiator are appended with (I) to show the deviation from real life aircraft.

5.1.1. ATR72-600(I) Analysis

The ATR72-600 aircraft has been created by the Aircraft Design Initiator, showing a good correspondence to the real life aircraft. The design features a high main wing to which a set of turboprop engines are mounted. A comparison of the ATR72-600 with the ATR72-600(I) is shown in Figure 5.1.

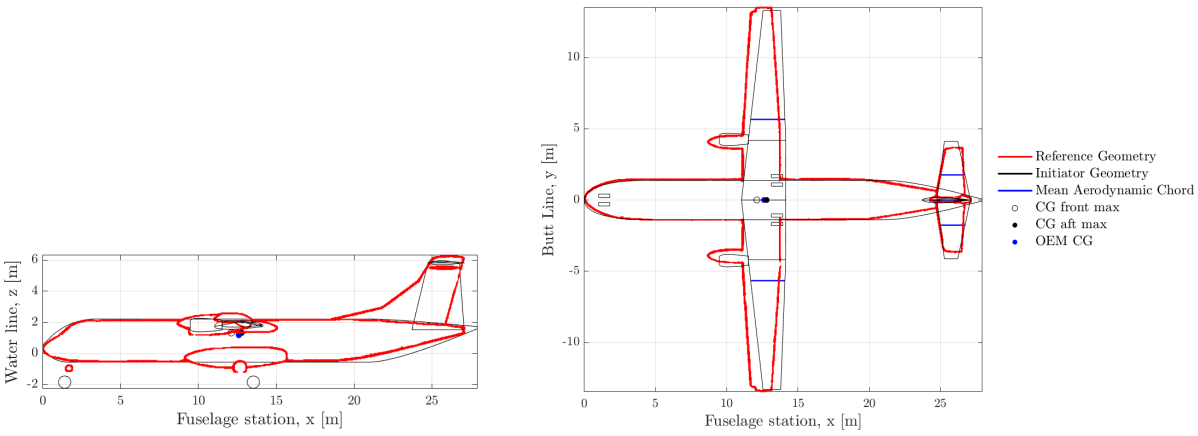

(a) Top View

(b) Side View

Figure 5.1: ATR72-600 geometry comparison

Slipstream Geometry

With the horizontal stabilizer positioned atop the vertical stabilizer the propeller slipstream remains clear of this surface, limiting the influence of the power-on scenario to just the main wing. This provides the framework to identify the influence of power-on effects on the main wing only. The slipstream geometry of the ATR72-600(I) is summarized in Table 5.1 to summarize the areas of the lifting surfaces impacted by the slipstream. Where the percentages represent the submerged length or area relative to a half-

Table 5.1: Slipstream presence on lifting surfaces of ATR72-600(I) aircraft

Flight phase	V_∞ (m/s)	V_S (m/s)	D_S (m)	b_S (m)	S_S (m^2)	$b_{S,H}$ (m)	$S_{S,H}$ (m^2)
Takeoff	41	92	3.3	3.3 (25%)	8.6 (29%)	~ (0%)	~ (0%)
Landing	48	90	3.4	3.4 (26%)	8.9 (30%)	~ (0%)	~ (0%)
Cruise	139	154	3.8	3.8 (29%)	9.8 (33%)	~ (0%)	~ (0%)

wing, accounting for the slipstream presence of one propeller. One can see the horizontal stabilizer is clear of any slipstream presence, independent of the flight phase. For the main wing the span submerged by the slipstream b_S is over a quarter in all flight cases, resulting in an effective submerged wing area S_S of about 30%. Taking into account the substantial velocity in the slipstream V_S relative to the free stream velocity V_∞ for takeoff and landing one can predict the presence of the slipstream will impact performance in these flight phases the most.

Aircraft Lift Coefficient

The first influence of power-on effects investigated is the lift coefficient of the aircraft minus tail $C_{L_{\mathrm{A-H}}}$. Figure 5.2 presents the lift curves for the ATR72-600(I) for a changing flap deflection δ_f and thrust coefficient C_T.

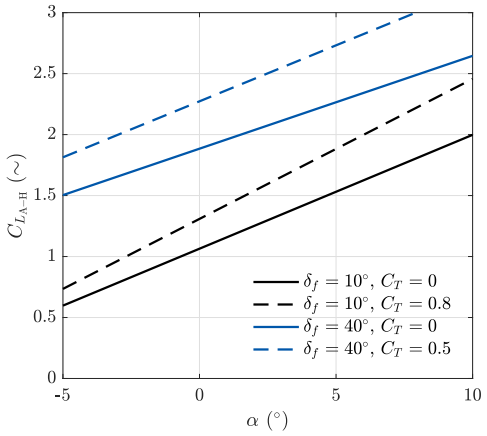

Figure 5.2: Aircraft minus tail lift coefficient versus angle of attack for ATR72-600(I)

Where two main characteristics are established regarding the effect of flaps and thrust. First of all, the increase of flap deflection results in a total increase in $C_{L_{\mathrm{A-H}}}$. Being the main point of including HLDs on the aircraft, this result is as expected. The largest effective increase is present for low values for the angle of attack as here the effective increase in wing chord and camber is dominant. When considering the power-on situation a number of interesting conclusion can be drawn. First of all, the absolute increase in $C_{L_{\mathrm{A-H}}}$ is larger for the landing condition at $C_T = 0.5$ as compared to the takeoff condition with $C_T = 0.8$. This can be explained as the total influence of the flaps is more dominant, increasing the lift of the surface.

The minute influence of the power-on case for small negative angles of attack in power-on can be contributed to the effect of the propeller thrust force which is effectively reducing the amount of wing lift. This is offset by the increased dynamic pressure to still result in a net increase, even for such negative angles of attack. This effect is less pronounced for the landing configuration for the same reason stated

above, the influence of the significant flap deflection is more dominant in the determination of the lift coefficient.

When analyzing the lift gradients C_{L_α}) in Figure 5.2 it is clear the increased C_T for the takeoff condition results in a larger lift gradient. C_{L_α} is increased by 25% for this takeoff condition where the increase in gradient is limited to 20% for the landing power-on situation. This means the power-on takeoff configuration is approaching the lifting capability of the power-off landing configuration, showing how influential the inclusion of the power-on effect is in determining aircraft performance.

Aerodynamic Center

The next property under investigation is the longitudinal position of the aircraft-minus-tail a.c.. A detailed breakdown of all contributions to the a.c. position is presented in Table 5.2.

Table 5.2: Breakdown of contributions to the aerodynamic center for the ATR 72-600(I) aircraft

Power	Flight phase	$\bar{x}_{ac_W}$	Δ_F	Δ_N	Δ_P	$\bar{x}_{ac_{A-H}}$
Off	Takeoff	0.25	-0.21	-0.012	-0.017	0.01
	Landing	0.25	-0.21	-0.013	-0.018	0.01
	Cruise	0.24	-0.22	-0.011	-0.017	0.01
On	Takeoff	0.24	-0.16	-0.009	0	0.08
	Landing	0.24	-0.18	-0.010	0	0.06
	Cruise	0.24	-0.20	-0.011	0	0.04

One sees how $\bar{x}_{ac}$ is almost constant for all power-off situations. In power-on, the aft shift of the aerodynamic center is strongest for the take-off condition. This is because the lift gradient of the aircraft is shown to increase most in this situation, decreasing the destabilizing effects of the fuselage and shifting the a.c. aft. The contribution of nacelle and feathered propeller both shift the a.c. position forward due to the engines being mounted on the main wing in a tractor configuration.

Tail Sizing Coefficients

All ATR72-600(I) parameters influencing tail sizing are presented in Table 5.3 where the influence of power-on on the lift coefficient (gradient) and the aircraft a.c. has been shown before, as was the absence of influence on the stabilizer between power-off and power-on. A parameter of interest is the

Table 5.3: ATR 72-600(I) horizontal tail sizing parameters per flight phase, including and excluding propeller and slipstream effects.

Flight phase	Power	M_∞	$\bar{x}_{ac}$	C_{L_α}	$C_{L_{\alpha,H}}$	V_H/V	$C_{m_{ac}}$	$C_{L_{A-H}}$	$C_{L_{H,fwd}}$	$C_{L_{H,aft}}$
Takeoff	0 kW	0.16	0.01	6.0	4.1	1.0	-0.84	2.2	-0.8	-0.5
Landing	0 kW	0.10	0.01	5.6	4.1	1.0	-1.58	3.0	-0.7	0.0
Cruise	0 kW	0.45	0.01	6.1	4.4	1.0	-0.32	1.3	-0.1	0.3
Takeoff	4,050 kW	0.16	0.08	7.6	4.1	1.0	-0.70	2.2	-0.8	-0.5
Landing	4,050 kW	0.10	0.06	6.9	4.1	1.0	-1.39	3.0	-0.6	0.0
Cruise	4,050 kW	0.45	0.04	6.6	4.4	1.0	-0.32	1.3	-0.1	0.2

pitching moment $C_{m_{ac}}$ which is negative (nose-down) for all flight phases. The total pitching moment is decreasing in power-on as the position of the aerodynamic center is shifted aft, reducing the effective arm of the lift force. The maximum lift coefficient of the aircraft $C_{L_{A-H}}$ is a setting of the Aircraft Design Initiator.

The final horizontal tail lift coefficient is determined using Equation 4.13 from Chapter 4 using the horizontal tail aspect ratio $A_H = 5$. The preference for a non-symmetrical installation of the tail plane is present here as the requirement for tail downforce is larger than that of tail lift. These limits are

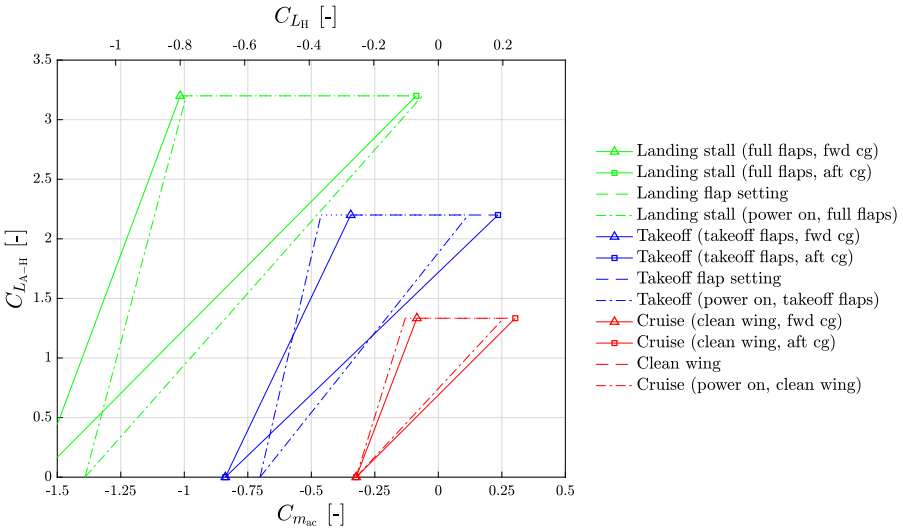

Figure 5.3: ATR72-600(I) trim diagram

graphically presented in the trim diagram of Section 5.1.1, showing the maximum values required for tail lift by the most leftward and rightward combination of aircraft c.g. and wing lift, requiring the tail to compensate for the total pitching moment.

Scissor Plot

With all coefficients determined and accounting for the influence of the slipstream and propeller forces on these, the scissor plot for this design can be created. The scissor plot for the ATR72-600(I) is shown in Figure 5.4.

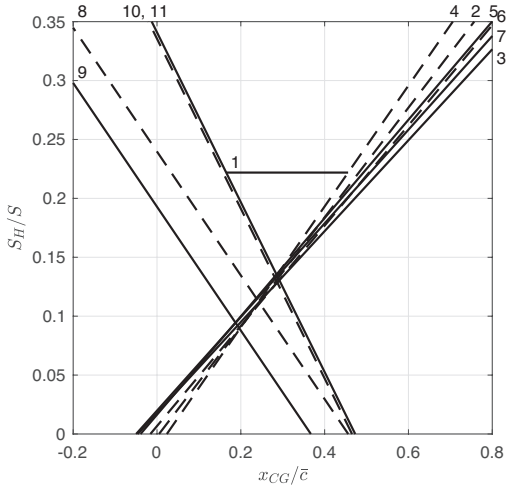

Figure 5.4: ATR72-600(I) scissor plot

The limiting cases are the power-on takeoff stability and the power-off landing equilibrium. In the determination of the stability limits a static margin (SM) is set to 5% mac. One can see that both power-on and power-off lines in the scissor plot are closely tied and the power-on effects on tail sizing are minor. This aligns with expectations knowing the absence of propeller forces and slipstream on the horizontal stabilizer. The power-on effects negatively impact the longitudinal stability limit as the ratio of lift gradients, tail over aircraft-minus-tail, will decrease. As a result the slope of the limit increases as shown in Figure 5.4. This effect is most pronounced for the low-speed and high-thrust conditions of landing and take-off. The limiting case is in takeoff power-on as this is consistent with the largest value for C_{L_α},

increasing the slope of the limit the most. The aft change in a.c. does not prove sufficient in accounting for this increase in aircraft-minus-tail lift gradient.

The equilibrium limit in landing shown in Figure 5.4 is a very close match between the power-off and power-on situation. This is because the slopes are in fact identical, shown through the aircraft minus tail lift coefficient $C_{L_{A-H}}$ in Table 5.3. The slight offset for power-on is present because the a.c. shift rearward is compensated by a decreased pitching moment coefficient $C_{m_{ac}}$, effectively canceling out in the determination of the limit according to Equation 4.6.

The rotation rate for take-off, set to a Torenbeek default of 0.052 deg/s^2, is more limiting in power-on.[27] This can be explained by means of Equation 4.11 where most parameters are equal in the power-on and power-off situation. The main exception is the inclusion of the thrust force which, for this aircraft configuration, is hindering rotation by means of the nose-down pitching moment generated by the engines. The fact that $C_{m_{ac}}$ increased in power-on is not enough to counteract this thrust force moment. Furthermore, the limit is starting further to the right in the scissor plot of Figure 5.4 which can be explained by the aft movement of the aircraft a.c. in power-on.

Generally speaking the influence of power-on effects on the stabilizer sizing of the ATR72-600(I) is minimal. The increase in lift gradient for the aircraft minus tail is limiting the design space more in case of power-on since the horizontal stabilizer is unaffected. The limits for the most forward c.g. are largely unaffected by the power-on conditions as most beneficial effects are compensated by a more forward a.c. position.

5.1.2. Fokker 50(I) Analysis

The Fokker 50 is the second aircraft for which the data is assessed to determine correct implementation of theory and methods in the Aircraft Design Initiator. An overview of this aircraft geometry is shown in Figure 5.5, comparing the Fokker 50 with the Fokker 50(I).

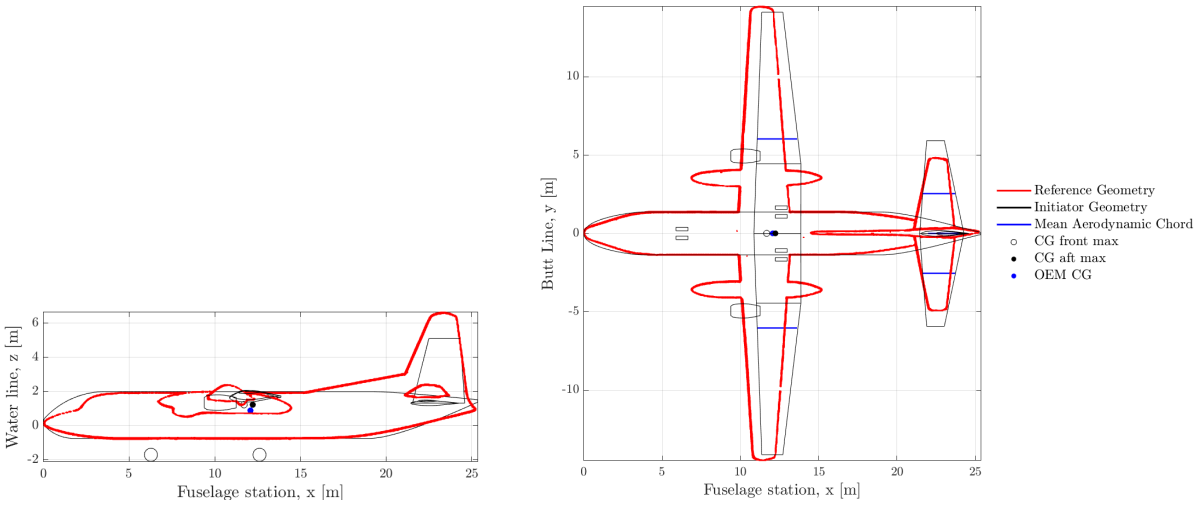

(a) Top View (b) Side View

Figure 5.5: Fokker 50 geometry comparison

Main discrepancies in design are the fuselage nose shaping, the inclusion of the engine and landing gear fairing and the positioning of this landing gear. All of these are affecting the final design, resulting in a deviation from the reference. Despite this the longitudinal stability and equilibrium limits stemming from the aerodynamic analysis are still of interest.

Slipstream Geometry

As done for the ATR72-600(I) the slipstream affected geometry for the Fokker 50(I) is determined, the result of which is shown in Table 5.4. The main conclusion made for the ATR72-600(I) holds true,

Table 5.4: Slipstream presence on lifting surfaces of Fokker 50(I) aircraft

Flight phase	V_∞ (m/s)	V_S (m/s)	D_S (m)	b_S (m)	S_S (m^2)	$b_{S,H}$ (m)	$S_{S,H}$ (m^2)
Takeoff	35	84	3.4	3.3 (23%)	8.9 (27%)	2.7 (45%)	4.1 (35%)
Landing	37	83	3.4	3.3 (24%)	9.0 (28%)	2.7 (46%)	4.1 (35%)
Cruise	146	154	3.9	3.9 (28%)	10.4 (31%)	3.0 (51%)	4.6 (39%)

showing a strong slipstream flow velocity increase for takeoff and landing. The main wing span fraction is around the 25% mark, with the total wing area affected close to 30%. The main difference with the ATR72-600(I) is that the horizontal stabilizer of the Fokker 50(I) is affected to a significant degree. The submerged span fraction is approaching half of the total stabilizer span. As the span covered is the outer section of the horizontal stabilizer where the chord is reduced the total slipstream surface area is changing from 35% in takeoff to almost 40% in cruise.

Tail Sizing Coefficients

The determination of the a.c. position for each flight phase and power setting is very similar for the Fokker 50(I) as compared to Table 5.2, which is why only the final value is provided here in Table 5.5.

Table 5.5: Fokker 50(I) horizontal tail sizing parameters per flight phase, including and excluding propeller and slipstream effects

Flight phase	**Power**	M_∞	$\bar{x}_{ac}$	C_{L_α}	$C_{L_{\alpha,H}}$	V_H/V	$C_{m_{ac}}$	$C_{L_{A-H}}$	$C_{L_{H,fwd}}$	$C_{L_{H,aft}}$
Takeoff	0 kW	0.14	0.05	6.0	4.4	0.85	-0.74	2.2	-0.5	0.0
Landing	0 kW	0.10	0.04	5.6	4.4	0.85	-1.24	2.6	-0.8	-0.2
Cruise	0 kW	0.46	0.04	6.1	4.6	0.85	-0.26	1.2	0.0	0.3
Takeoff	3,150 kW	0.14	0.10	7.8	4.5	2.4	-0.62	2.2	-0.4	0.0
Landing	3,150 kW	0.10	0.09	7.2	4.4	2.2	-1.09	2.6	-0.7	-0.2
Cruise	3,150 kW	0.46	0.07	6.6	4.8	1.1	-0.26	1.2	-0.1	0.2

The conventional tail position of the Fokker 50 shows in the parameters by means of the tail velocity ratio V_H/V. Where the power-off situation shows a value less than unity, the power-on shows the real effect of a fast-flowing slipstream over the stabilizer surface. The velocity ratio exceeds 1.0 in cruise and shows values over 2.0 for the low-speed flight phases of take-off and landing. Similar effects as discussed for the ATR72-600(I) are observed for the Fokker 50(I). These effects are the power-on increase in $C_{m_{ac}}$, $\bar{x}_{ac}$ and C_{L_α}. Other than for the T-tail ATR aircraft, here the tail lift gradient $C_{L_{\alpha,H}}$ shows an increase in power-on as compared to the power-off situation.

The limiting cases for the requirement of horizontal stabilizer lift are presented by the extremes in the last two columns of Table 5.5. These values are presented again in the aircraft trim diagram of Section 5.1.2.

Scissor Plot

The final scissor plot is presented in Figure 5.7 where the influence of the increased tail dynamic pressure is clearly identifiable.

The increased velocity ratio influences all limits in the scissor plot: longitudinal stability, equilibrium at stall and the take-off rotation requirement. For each of these limits an increase in velocity ratio is beneficial, increasing the stabilizer effectiveness. This means the tail sizing of the Fokker 50(I) has been limited by power-off conditions only. The forward bound of the c.g. is presented by the control at

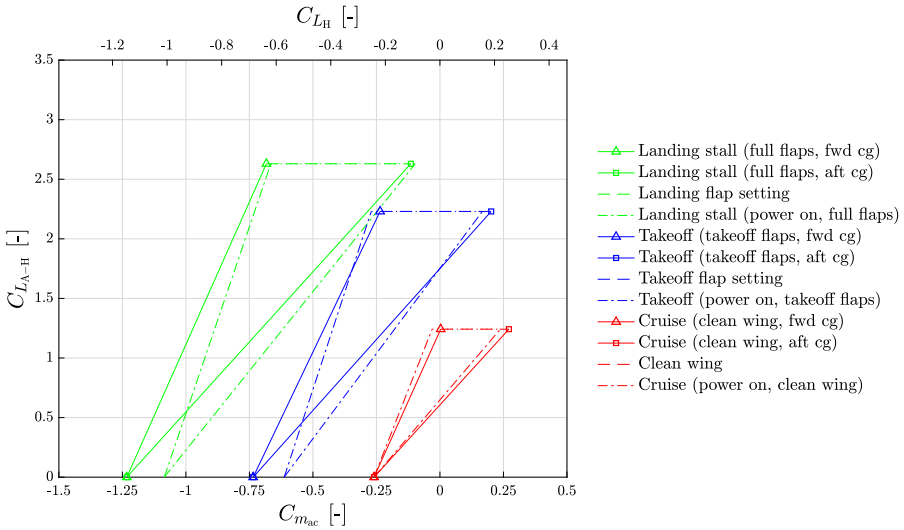

Figure 5.6: Fokker 50(I) trim diagram

stall configuration where the aft c.g. is restricted by the stability limit in takeoff. Again, takeoff is critical due to the largest ratio of lift gradients as presented in Table 5.5.

One sees expected behavior of the methods for the power-on situation, showing significant differences between the T-tail ATR72-600(I) and the conventional tail layout of the Fokker 50(I). The power-on limits are generally more allowing, specifically in the case of the Fokker 50(I) where the horizontal stabilizer could, in theory, profit from the presence of the slipstream. The drawback for aircraft design is that power-off limits are still to be met. The implementation of power-on limits are expected to be of great importance in the creation of those unconventional designs where power-effects are present only for the stabilizer.

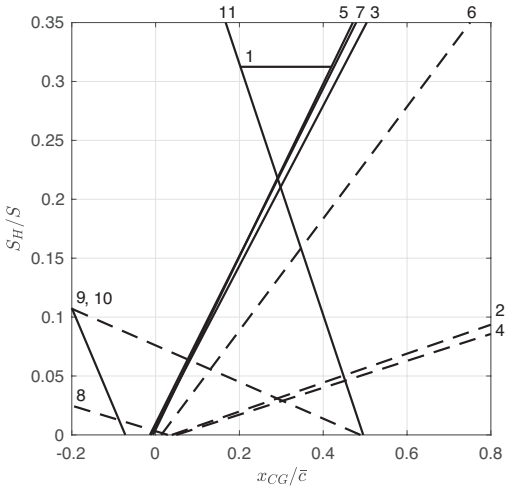

1 - CG excursion
2 - Stability limit (LA, power on)
3 - Stability limit (LA, power of)
4 - Stability limit (TO, power on)
5 - Stability limit (TO, power off)
6 - Stability limit (CR, power on)
7 - Stability limit (CR, power off)
8 - Rotation limit (TO, power on)
9 - Rotation limit (TO. power off)
10 - Equilibrium limit (LA, power on)
11 - Equilibrium limit (LA, power off)

Figure 5.7: Fokker 50(I) scissor plot

5.2. Validation of Initiator Design

The previous section verified the implementation of the methods for sizing the tail surface. This section will compare the converged Aircraft Design Initiator results to performance estimates for modified DC-9 Super 80 propfan configurations. This reference aircraft study focused on the performance of a Douglas DC-9 Super 90 aircraft when outfitted with propfan engines. These engines can be seen as a potential hybrid between propeller and turbofan engines, allowing for high propulsive efficiency at high altitude and cruise velocity.

5.2.1. Configurations

The research focuses on the effect of engine placement and considers three engine configurations with the main wing, the aft fuselage and the horizontal stabilizer to be the most promising based on performance estimates for aerodynamics, weight and acoustics. These configurations are presented in Table 5.6. [19]

Table 5.6: Layout configurations for DC-9 Turboprop Modifications

Modification	Main wing	Engine	Hor. Stabilizer
1	Low	Above	T-Tail
2	Low	Aft Fuselage	T-Tail
3	Low	Hor. Stabilizer	Conventional

The resulting aircraft from Goldsmith's research have been reverse-engineered to obtain feasible designs meeting the top-level requirements of the aircraft. For this reverse engineering, most of the data was obtained directly from the report by Goldsmith. Where data was missing, the DC-9 Super 80 specifications were used. [4] One major remark to be made here is that currently the Aircraft Design Initiator is not capable of analyzing propfan engines, requiring one to employ turboprop engines on the designs.

This has major consequences for the performance comparison as turboprop powered aircraft are limited in altitude and cruise Mach number due to the required increase in propeller power exceeding the capabilities of the engine. This results in a rapid increase in propeller diameter, causing supersonic tip velocities which challenge the structure and result in performance degradation. As such the Goldsmith design Mach number of 0.8 is not attainable and the Mach number in cruise was lowered to an allowable 0.6, equivalent to the specification of the RTP aircraft. For this free stream velocity the propeller was sized to match the diameter of the propfan equal to $D_P = 3.4$m.

For each design the settings of Table 5.7 have been used in creating and assessing the configuration of the Aircraft Design Initiator. The 155-passenger aircraft modifications feature a 2-3 seating layout and double-slotted Fowler flap geometry spanning 60% of the main wing trailing edge span. The resulting geometries are shown in Figures 5.8 to 5.10.

5.2.2. Performance Comparison

The Aircraft Design Initiator is capable of replicating the designs proposed by Goldsmith based on the geometries presented. More important is the match in performance with the values presented by Goldsmith as to validate the capabilities of the Aircraft Design Initiator to generate and assess a 155-pax turboprop powered aircraft.

Before this comparison is presented it is important to state the difference in the design routine between Goldsmith and this thesis. The first fixes the aircraft MTOM resulting in a change in operational range for a changing configuration. The resulting range is used as an input in the Aircraft Design Initiator which will cause the MTOM to change from the value provided by Goldsmith.

Results are presented in Table 5.8 where the harmonic mission range of the modified DC-9 aircraft is closely matched by the Aircraft Design Initiator. The main discrepancy is the significantly lower MTOM for the Initiator-analyzed aircraft. The comparison shows the fuel mass mission fuel mass (MFM) of

Table 5.7: Aircraft Design Initiator input settings - DC-9 Modifications

Propery	Value
seat pitch (m)	0.86
passenger mass (kg)	80
luggage mass (kg)	25
no. of propeller blades (~)	10
M_{tip} (~)	0.92
l_{takeoff} (m)	1350
l_{landing} (m)	1350
$C_{L_{\text{max}}}$ (clean) (~)	1.2
$C_{L_{\text{max}}}$ (takeoff) (~)	2.0
$C_{L_{\text{max}}}$ (landing) (~)	2.8
δ_{HLD} (takeoff) (°)	18
δ_{HLD} (landing) (°)	40
SM (% mac)	7.8%
SFC (lb/lbf/h)	0.5

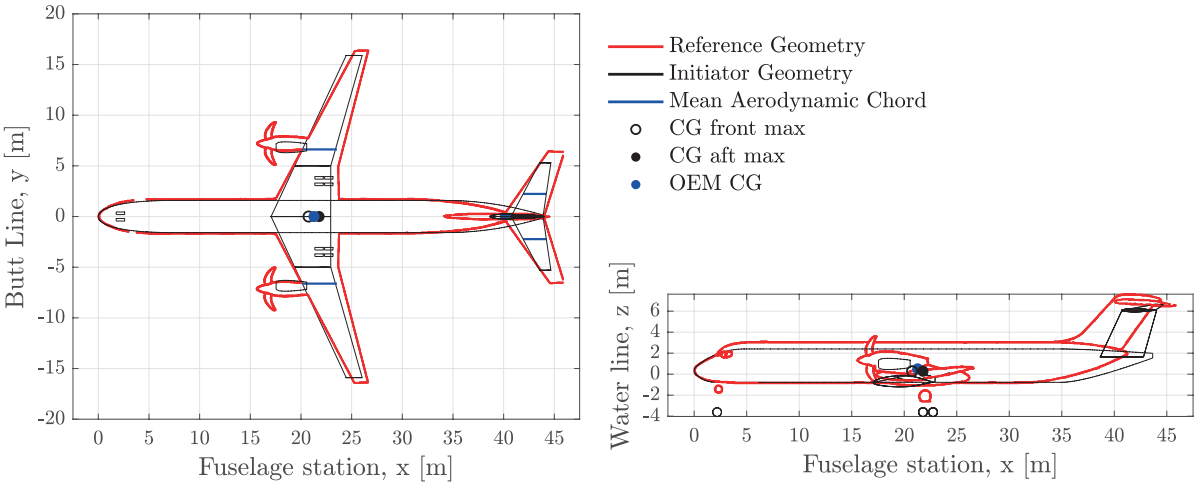

Figure 5.8: DC-9 Super 80 Mod.1 geometry

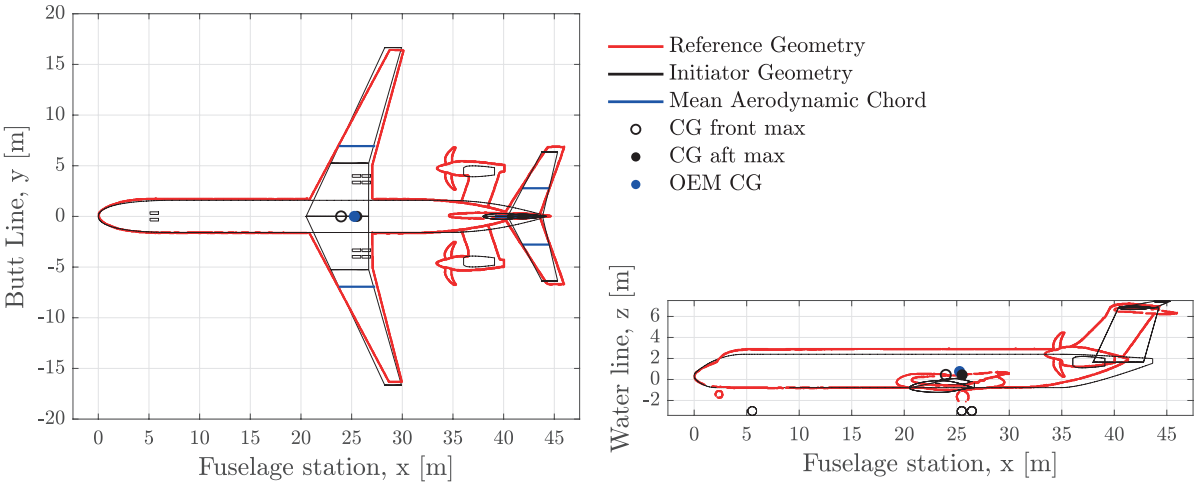

Figure 5.9: DC-9 Super 80 Mod.2 geometry

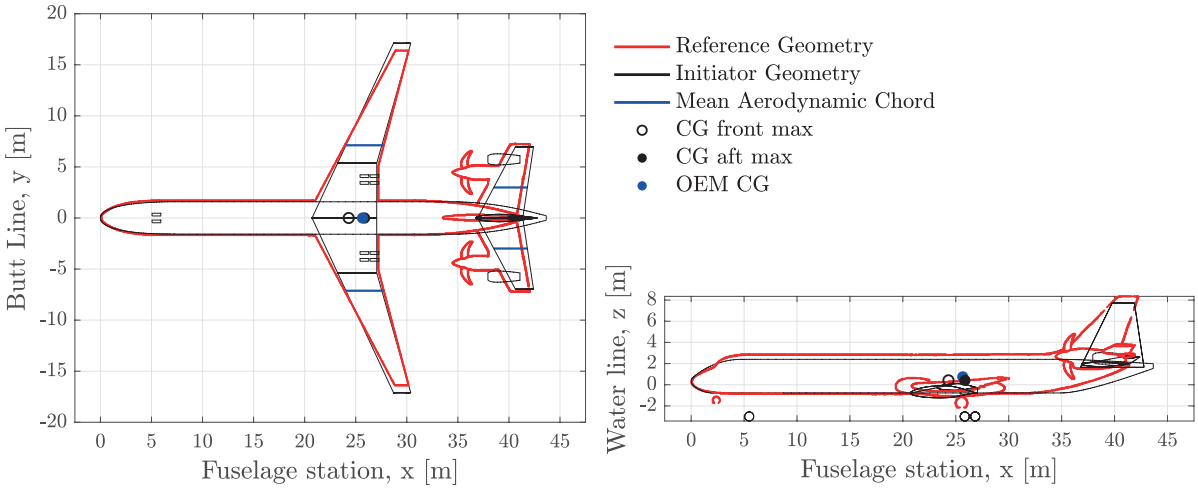

Figure 5.10: DC-9 Super 80 Mod.3 geometry

Table 5.8: Overview of properties for Goldsmith modified DC-9 Super 80 and validation aircraft [19]

	DC-9 Super 80			Initiator aircraft		
	Mod. 1	Mod.2	Mod. 3	Mod.1(I)	Mod.2(I)	Mod.3(I)
Range (km)	2739	2295	2869	2740	2295	2871
MTOM (t)	63	63	63	55	56	60
OEM (t)	38	38	39	30	31	33
MFM (t)	8.9	7.5	9.1	8.2	7.2	9.5
C.G. Exc. (%mac)	25%	36%	34%	29%	41%	40%
$x_{\bar{c}/4}$ (%l_F)	51%	57%	58%	48%	56%	57%
l_H (m)	22	18	14	22	18	14
S (m^2)	112	112	112	103	113	119
S_H (m^2)	33	36	47	23	32	43
S_H/S (~)	0.29	0.32	0.42	0.22	0.28	0.37
V_H (~)	1.6	1.6	1.5	1.30	1.65	2.12

the configurations is closely approximated by the Initiator, eliminating this as the cause of the mass difference. Since payload mass is equal between the reference data and created aircraft, the reduction of MTOM is fully due to the estimation for aircraft OEM.

Weight estimation methods included in the Aircraft Design Initiator have been shown to underestimate the values for OEM and MTOM by more than 10% for specific configurations, especially larger aircraft.[16]. The ratio OEM over MTOM has been named by Elmendorp as a more accurate metric for Initiator performance in comparing to reference aircraft. Doing so for the values in Table 5.8 shows Initiator ratios of 55% OEM of MTOM. Compared to the Goldsmith ratio of 60% this would fall within the potential 10% underestimation of Initiator mass methods.

The resultt is a positive feedback loop as any underestimation of components will further introduce weight reductions in other parts of the aircraft sizing, decreasing the total aircraft weight further. Potential risks in the Aircraft Design Initiator for inaccurate mass predictions feature the components determined using a Class II weight estimation only. These component masses rely on data present from other aircraft which influences the sizing in case the configuration is unconventional. However, as all Initiator-generated modifications are underestimated the mass estimation appears to be inaccurate for all, denoting a more significant limitation in the Aircraft Design Initiator.

When analyzing the general trends in moving the propeller further aft one can take the DC-9 Mod.1 and Initiator Mod.1(I) as baseline designs, representing the most conventional layout of main wing mounted engines. The excursion of the c.g., represented as percentage mac in Table 5.8, is greatly increased by introducing the engines further backwards. This is in line with the expected behavior and is shown for both the DC-9 modifications and the Initiator aircraft. The c.g. excursion comparison between Goldsmith and the Initiator show the range is four to six percent point larger for the Initiator. The main reason for this is the fact that the Aircraft Design Initiator limits the c.g. at the extremities of the loading diagram as presented in Chapter 4. Typically aircraft sizing includes less restrictive limits, imposing limits in loading and operation of the aircraft. However, such limits could not be obtained from the research of Goldsmith directly and as such the discrepancy between the excursion of c.g. remains.

The introduction of the aft weight results in a shift aft of the main wing apex to re-position the aircraft a.c. relative to the c.g.. This is captured by the value presented for the quarter-chord mac of the main wing as a percentage of fuselage length l_F. The most conventional layout, Modification 1, shows this to be 51% (Goldsmith) and 48% (Initiator). For the aft engine layouts this position approaches 60%. This in turn results in a decrease in available tail arm l_H, the distance from wing to tail quarter-chord mac. The DC-9 Mod.2 shows a reduction of l_H of 15% with horizontal stabilizer mounted engines (Mod.3) totaling a l_H reduction of almost 35%. The reduction of l_H for the Initiator aircraft is equal, showing a very close match in tail arm. This decreased tail arm affects the tail sizing of the aircraft showing an increase from Mod.1 through Mod.3.

5.2.3. Horizontal Stabilizer Sizing

The tail sizing data presented by Goldsmith is combined with the DC-9 scissor plots generated by the Aircraft Design Initiator. In general, the tail area is underestimated by the Initiator. This does not aid the aforementioned issue with mass underestimation as a decrease in stabilizer area is expected to reduce the mass, introducing the previously mentioned positive feedback on glsoem.

These three tail sizing diagrams allow a direct comparison of c.g. excursion, the forward and aft c.g. limits and the binding limits for the configuration. Goldsmith chose to size according to tail volume coefficient V_H which is presented together with the tail area ratio S_H/S in Table 5.8. In general the Aircraft Design Initiator shows an underestimation of the horizontal stabilizer area relative to the Goldsmith data.

Modification 1

For Mod.1 in Figure 5.11 the forward c.g. is less forward for the Initiator and is bounded by the equilibrium in landing condition, power-off. The same limit is present for the Goldsmith sizing but, as expected, this limit is further forward with the c.g. position. The aft limit in Goldsmith was presented to be the power-off stability in cruise, which for the Initiator was not limiting. In fact, the power-on situation was

calculated to be more restrictive, limiting the aft c.g. position. This might show the importance in including power-on effects as the design features a T-tail which will not be influenced by the propeller slipstream. In general the sizing for Mod.1(I) does not match the data and the shift in c.g. excursion indicates the issue in mass estimation is influencing the sizing for the stabilizer negatively.

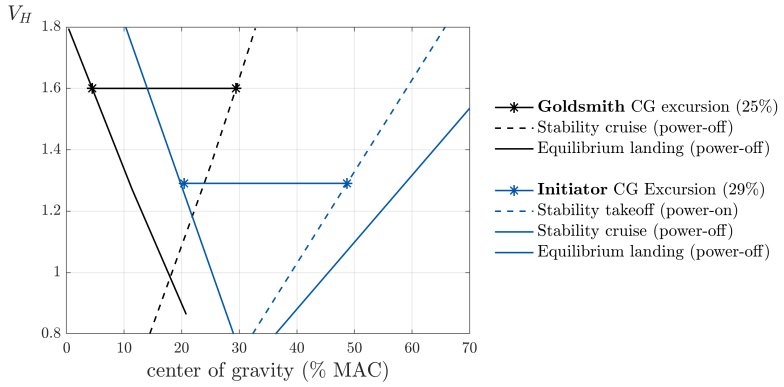

Figure 5.11: DC-9 Super 80 Mod.1 scissor plot. Partly adapted from Goldsmith [19, p. 68]

Modification 2

Modification 2 in Figure 5.12 shows a close match between Goldsmith and Initiator sizing. The forward c.g. limits are close together and are limited by power-off landing equilibrium. The limit on the aft c.g. by Goldsmith is an operationally imposed tip-over limit and is therefore not sized in the Initiator scissor plot.

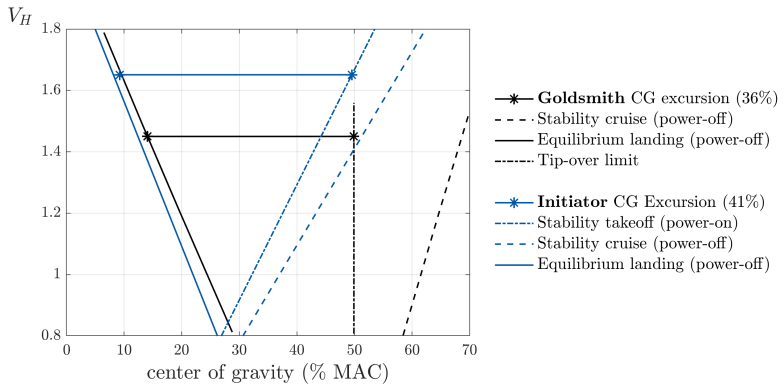

Figure 5.12: DC-9 Super 80 Mod.2 scissor plot. Partly adapted from Goldsmith [19, p. 69]

Important to note is that the aircraft mean gear position is always aft of the aft c.g. limit. As a result the tip-over for far aft c.g. positions is not experienced for the Mod.2(I) and sizing is performed on aerodynamic limits only. The c.g. is limited at the rear by the power-on takeoff stability limit. The final result is a close match with the Goldsmith design showing similar c.g. excursions and tail volume coefficients.

Modification 3

Figure 5.13 shows the Modification 3 tail sizing where both the Initiator and Goldsmith limits are the power-off cruise stability and landing equilibrium. The power-off condition was predicted to be limiting afor Mod.3(I) as the presence of the stabilzier-mounted engines results in the increase of dynamic pressure mentioned in verification of the methods, Section 5.1. The resulting limits show similar trends with the note that the landing equilibrium is more restrictive, according to the Aircraft Design Initiator. The result is a larger tail volume coefficient for comparable c.g. excursions.

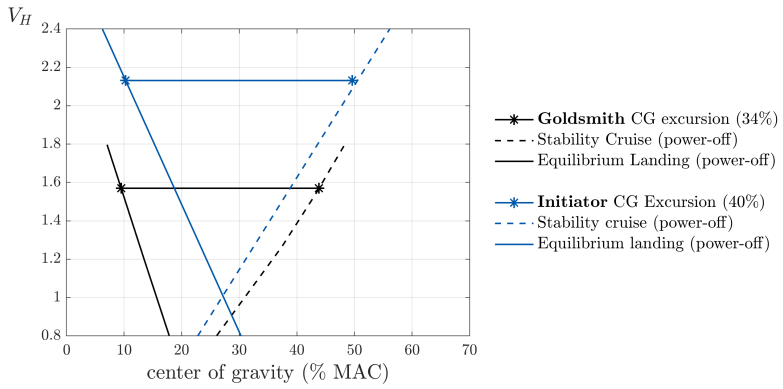

Figure 5.13: DC-9 Super 80 Mod.3 scissor plot. Partly adapted from Goldsmith [19, p. 68]

In general, the two more exotic configurations of aft-fuselage and stabilizer mounted engines (Mod.2 & Mod.3) show a better correspondence between Initiator and Goldsmith sizing methods with the more conventional design (Mod.1) showing too major a difference to conclude an accurate reproduction was achieved. The verification & validation of the methods and Initiator proved a variety of engine placements and stabilizer configurations are possible. The Initiator is able to adequately incorporate power-on effects as shown for Mod.2, where the take-off limit was critical for power-on. Whilst the reverse-engineered results are not perfect, the presented results allow for a continuation towards a new design with confidence in the presented methods and the incorporation of these in the Aircraft Design Initiator.

6 Results

After verification & validation of the Aircraft Design Initiator the main research goal can be studied: the creation of a feasible RTP aircraft design. The feasibility and competitiveness of the RTP is assessed by investigating the design options presented in Chapter 2. Section 6.1 is concerned with the performance of these designs and will study the most competitive design configuration for the mission where Section 6.2 includes a sensitivity analysis for a single RTP configuration.

6.1. Regional Turboprop Aircraft

The designs that are to be assessed by the Aircraft Design Initiator on mission performance and market competitiveness are created using the capabilities of this very same tool. To obtain feasible results the inputs of the Initiator need to be carefully selected.

6.1.1. Settings and Design Choices

These input settings are the same for all configurations and shown in Table 6.1. The selected seat pitch of the aircraft is equal to that of the Bombardier CS100 all-economy cabin seat pitch. Other properties obtained from this aircraft are the takeoff field length l_{takeoff} and landing field length l_{landing}. Estimations of the cruise lift-over-drag ratio $(L/D)_{\text{cruise}}$ stem from the wing aspect ratio and predicted zero-lift drag coefficient of the aircraft and have been decided after an iterative attempt to create the feasible aircraft. The same method holds true for the definition of the maximum lift coefficients presented in Table 6.1.

Table 6.1: Input settings for conceptual RTP

Setting	Value	Unit
seat pitch	0.73	(m)
passenger mass	80	(kg)
luggage mass	25	(kg)
M_{tip}	0.92	(∼)
l_{takeoff}	1350	(m)
l_{landing}	1350	(m)
$(L/D)_{\text{cruise}}$(min)	18	(∼)
$C_{L_{\text{max}}}$ (clean)	1.6	(∼)
$C_{L_{\text{max}}}$ (takeoff)	2.2	(∼)
$C_{L_{\text{max}}}$ (landing)	3.0	(∼)
δ_{HLD} (takeoff)	10	(°)
δ_{HLD} (landing)	32	(°)
$\dot{\theta}$	0.052	(deg/s^2)

Table 6.2: Design choices for conceptual RTP

Choice	Value	Unit
A	11	(∼)
A_H	6	(∼)
A_V (conventional)	1.6	(∼)
A_V (t-tail)	1.2	(∼)
no. of propeller blades	10	(∼)
$P_{\text{max,cont.}}$	$0.95P_{\text{max}}$	(∼)
spinner ratio	0.15	(∼)
SFC	0.5	(lb/lbf/h)
SM	2%	(% mac)
λ_H	0.6	(∼)
λ_V (conventional)	0.4	(∼)
λ_V (t-tail)	0.8	(∼)

Apart from these settings a number of design decisions have been made. These design choices influence the final design and as such should ideally be equal for each configuration. Some design choices

have been named before as the application of two turboprop engines and the type of horizontal stabilizer Due to the significant design deviations between the configurations proposed, some parameters are changed from aircraft to aircraft to ensure the end result is feasible, showing the list as presented in Table 6.2.

The number of propeller blades is such that a rotor of high solidity is present, similar to that of the propeller installed on the current aircraft featuring the TP400-D6 turboprop engine: the Airbus A400M military transport. [5] The aircraft specific fuel consumption (SFC) is set to the default for the Aircraft Design Initiator as a proper turboprop engine sizing, including fuel efficiency, is currently not implemented. A maximum continuous power setting is defined as 95% of maximum rated shaft power, this power setting is used in the power-on analysis of the aircraft.

For the lifting surfaces a number of choices are shown in Table 6.2. The main wing features a high-aspect ratio A to benefit aerodynamic performance. Horizontal stabilizer taper ratio λ_H and aspect ratio A_H are set to upper limits obtained from Obert summarizing design of fixed stabilizers. [24] A similar approach was taken for the vertical stabilizer where the choice was made to differentiate between a conventional tail layout and a T-tail configuration. The latter is designed using a lower aspect ratio and taper ratio vertical stabilizer to accommodate such configuration. The airfoils used on the main wing are NACA 6-series laminar flow profiles with decreasing thickness towards the wing tip. The vertical and horizontal stabilizer feature symmetrical NACA 4-series airfoils of moderate thickness. The set of settings and design choices form, together with the top level requirements described in Chapter 2, the full definition of the configurations of Table 2.3.

The converged design geometries of the RTP aircraft are presented in Figures 6.1 and 6.2. The distinct engine and wing placement is visible for all turboprop aircraft. The length and position of the wing & stabilizer mac is included for reference. Furthermore the OEM c.g. position is indicated, together with the most forward and aft c.g. limits.

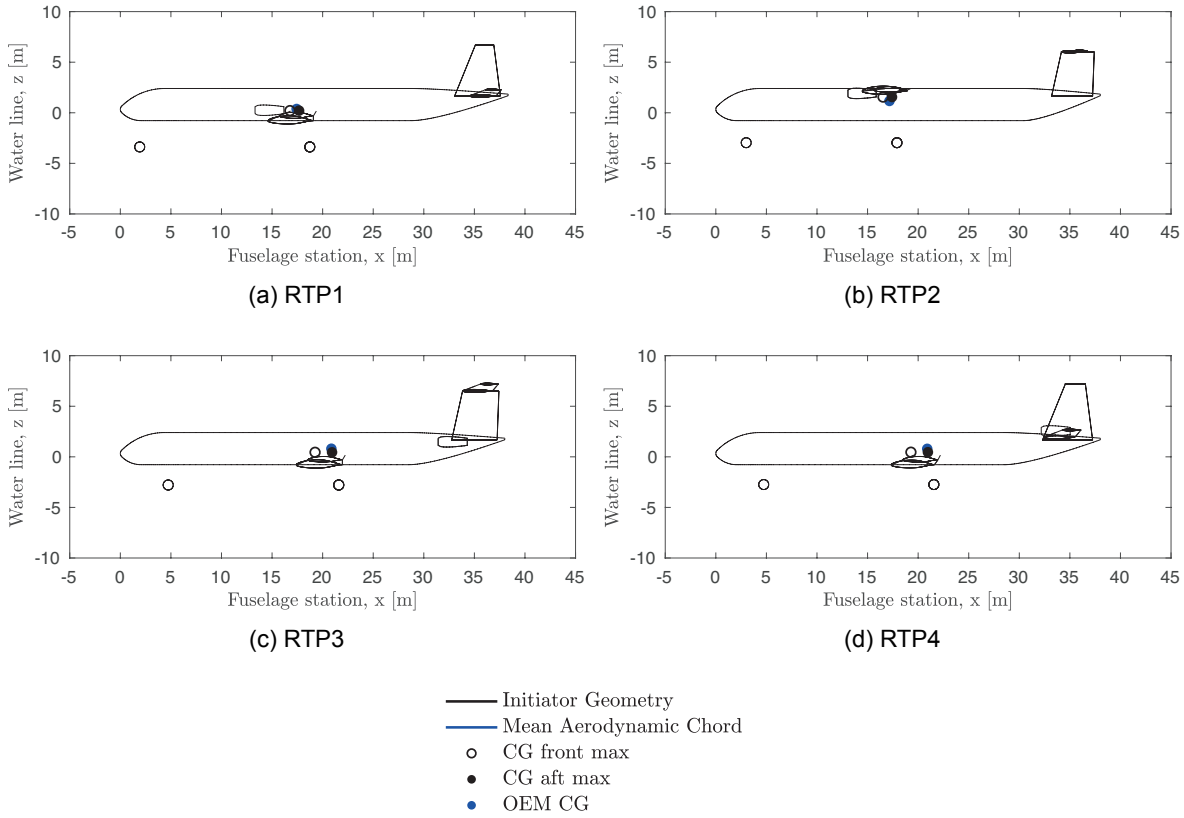

(a) RTP1 (b) RTP2

(c) RTP3 (d) RTP4

Figure 6.1: Side view of RTP aircraft configurations

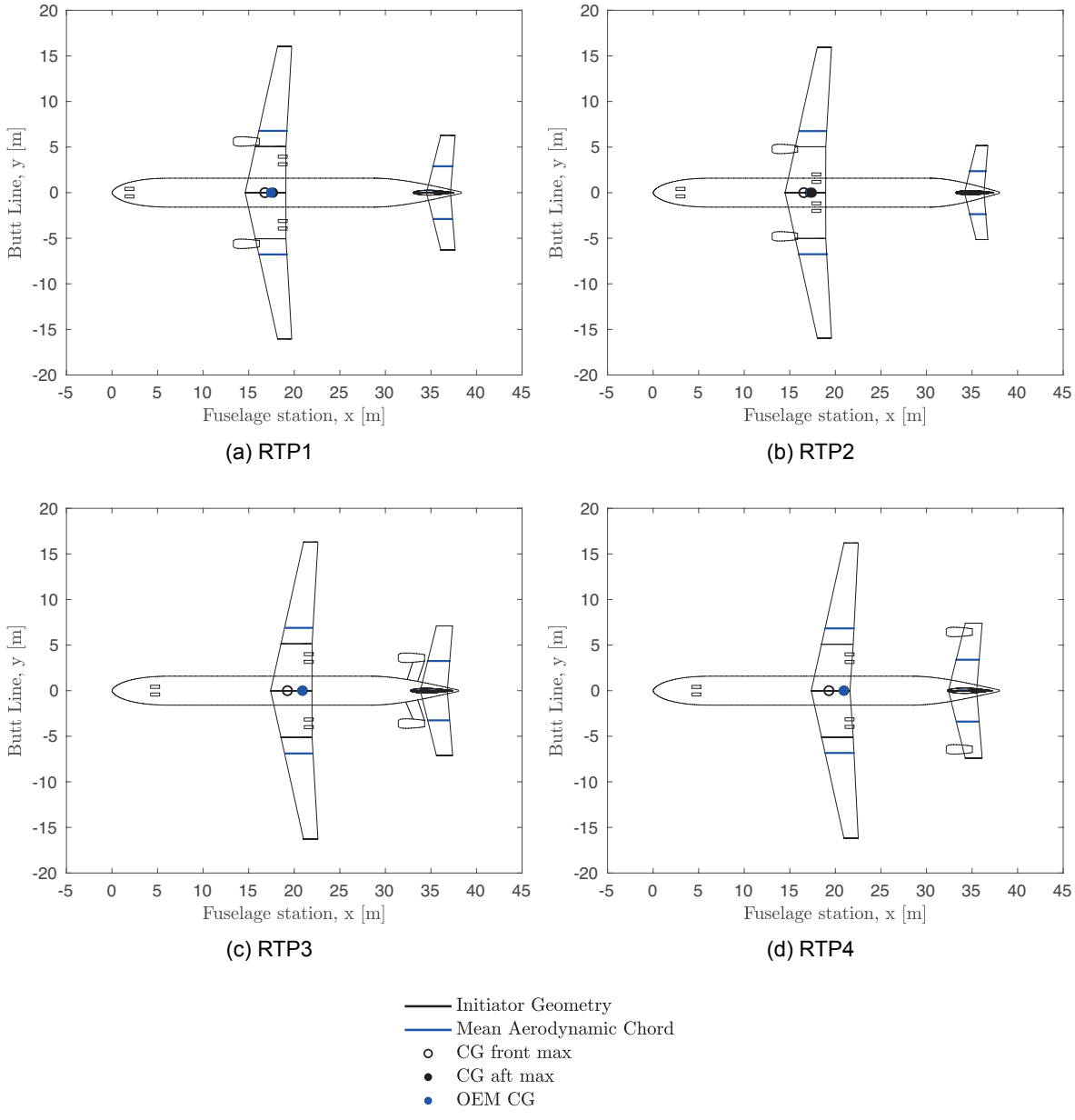

(a) RTP1

(b) RTP2

(c) RTP3

(d) RTP4

Figure 6.2: Top view of RTP aircraft configurations

6.1.2. Horizontal Stabilizer Sizing

The first results presented for the RTP are the loading diagrams, displaying all c.g. excursions in Figure 6.3. Two main sets can be identified in the set of RTP configurations. The first is showing a centering of the c.g. for RTP1 and RTP2 as is clear from Figures 6.3a and 6.3b. The resulting total c.g. excursion of almost 30%mac is relatively small when compared to the excursion for the other set. This set, consistent of the RTP3 and RTP4 configurations, has a strong c.g. shift forward during the loading of the aircraft as shown in Figures 6.3c and 6.3d. Resulting is a 60%mac c.g. excursion for these configurations.

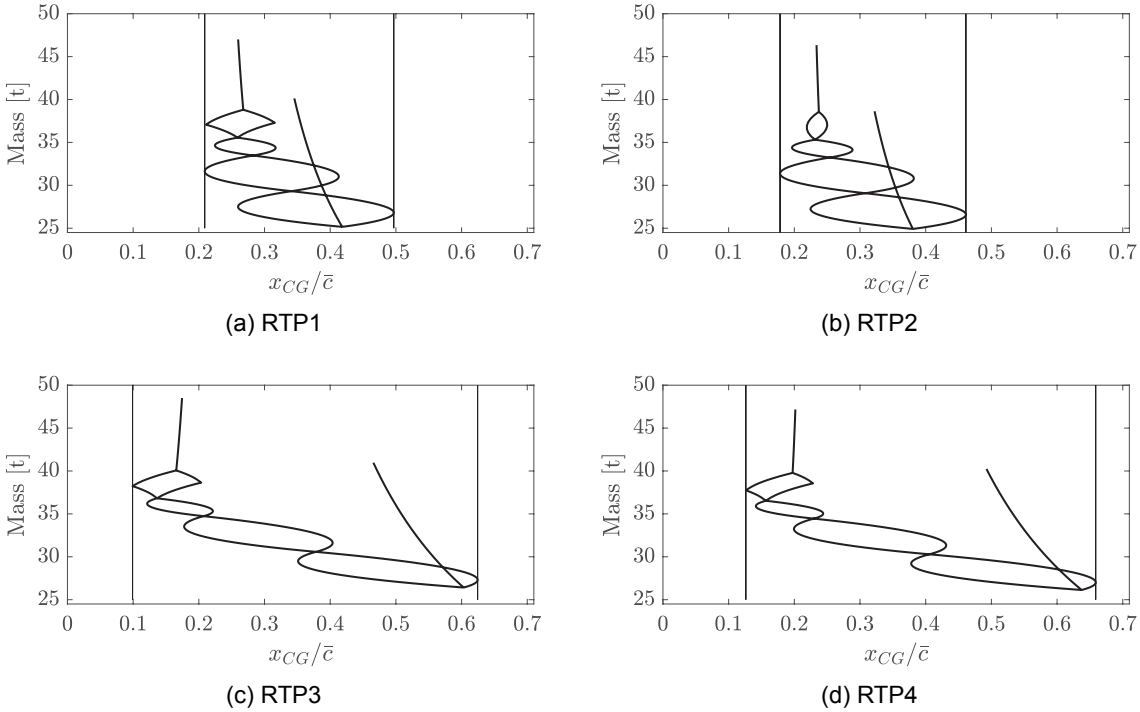

(a) RTP1 (b) RTP2

(c) RTP3 (d) RTP4

Figure 6.3: RTP aircraft loading diagrams showing forward and aft c.g. limits as fraction of mac

Note that for all configurations the harmonic mission fuel c.g. position is (close to) vertical at about 20% to 25% mac. This is expected as the centering of fuel weight means the total shift in c.g. during the fuel burn of the harmonic mission is minimal. The excursions presented are used to size the horizontal tail using the implemented tail sizing method. The resulting scissor plots are presented in Figure 6.4 for all four configurations.

The scissor plots show design feature expectations as discussed for method verification in Chapter 5. For all except RTP4 the aft c.g. limit is provided by the stability limit in power-on. For the RTP1 this is the cruise condition where RTP2 and RTP3 are limited in the take-off equilibrium. These are limiting due to the absence of direct slipstream influence on the horizontal tail for all three configurations, resulting in the decrease of the lift gradient ratio of the stability limit as compared to the power-off case. The lack of slipstream over the horizontal tail means the tail velocity ratio is not beneficial to the performance of the horizontal stabilizer.

Absence of this slipstream for RTP1 might seem counter-intuitive with a low wing and conventional tail design. However, the combination of the propeller normal force and wing downwash effect increase the slipstream deflection downwards, steering the circular contour of high dynamic pressure clear of the horizontal stabilizer. Note that for low-altitude situations as the take-off run this downward deflection of the slipstream will in reality be limited by the presence of the ground. In such a case the deflected slipstream might affect the stabilizer directly. Speaking specifically for the case of the RTP1 aft c.g. limit in Figure 6.4a this will not affect the power-on cruise limit and as such will not allow for a reduction in required tail surface area.

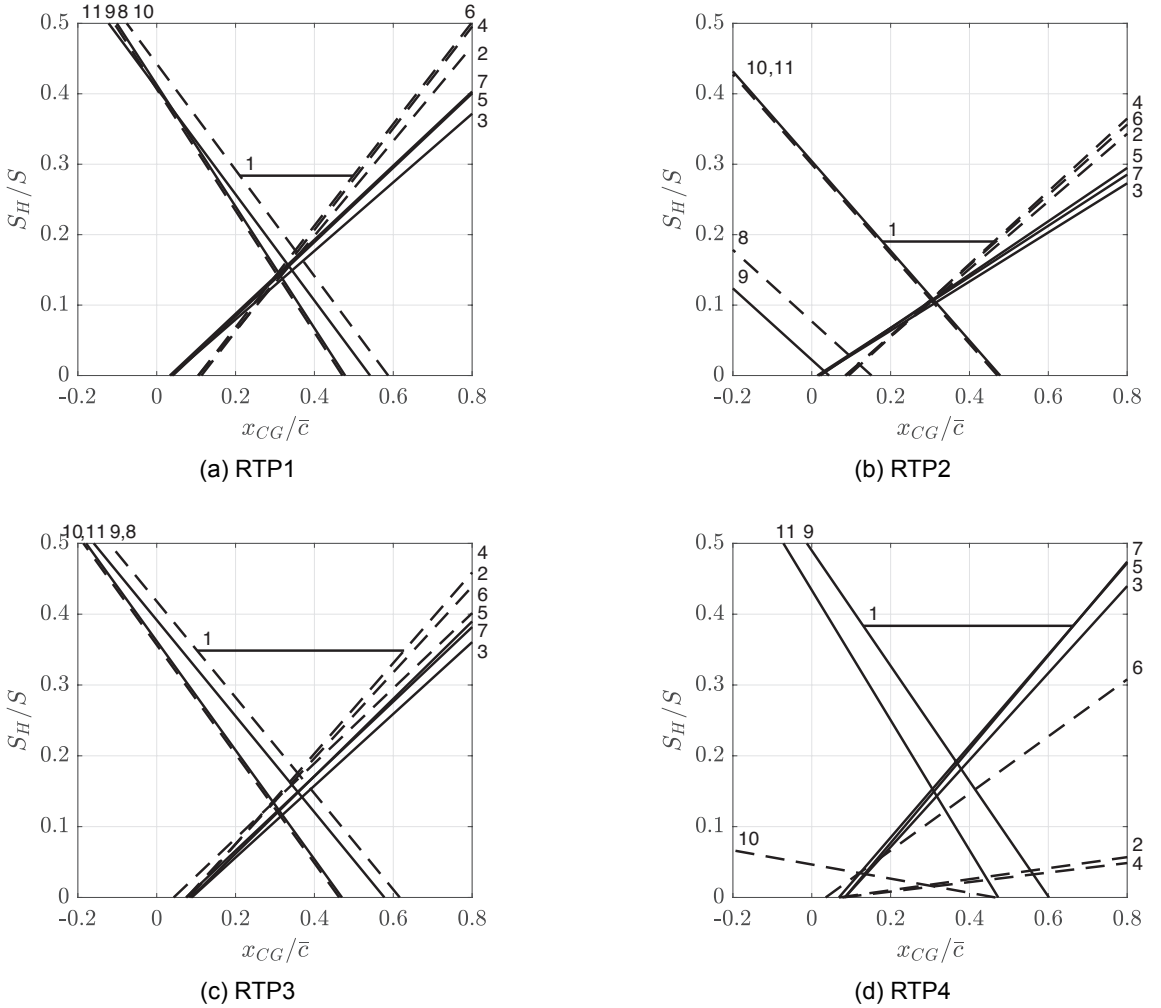

1 - CG excursion
2 - Stability limit (LA, power on)
3 - Stability limit (LA, power of)
4 - Stability limit (TO, power on)
5 - Stability limit (TO, power off)
6 - Stability limit (CR, power on)
7 - Stability limit (CR, power off)
8 - Rotation limit (TO, power on)
9 - Rotation limit (TO. power off)
10 - Equilibrium limit (LA, power on)
11 - Equilibrium limit (LA, power off)

Figure 6.4: RTP aircraft scissor plot relating horizontal stabilizer area ratio to c.g. excursion

Figures 6.4a and 6.4b show the scissor plots for RTP1 and RTP2 where the forward c.g. is limited by the equilibrium in landing configuration. These limits are defined by the strong nose-down pitching moment of these configurations due to the deflection the trailing edge HLDs. For the RTP1, power-on effects are dominating as the engines positioned atop the main wing will increase the effective nose-down pitching moment by means of the offset of thrust with the aircraft c.g. position. For RTP2 the power-off limit is limiting although the difference with the power-on limit is minimal. The engine vertical position aligning closely with the c.g. position prevents thrust from influencing the pitching moment coefficient significantly. As for the ATR72-600(I), the power-on situation is balanced as the offset in aircraft a.c. is compensated for by a reduction in the nose-down pitching moment coefficient.

For RTP3 and RTP4 in Figures 6.4c and 6.4d the most forward c.g. is limited by the take-off rotation requirement. This is a consequence of the required aft shift of the main wing in order to compensate for the engine placement at the rear of the aircraft. This is done to re-position the a.c. relative to the aircraft c.g.. With the main gear stowed in the main wing the system is forced further aft. Since the rotation limit is calculated using the moments about the main gear as point of rotation the aft shift of main gear is diminishing the influence of the horizontal stabilizer. The difference between RTP3 and RTP4 for this rotation limit is the power setting. For RTP3 the stabilizer is clear of the flow velocity effect. Furthermore, the engine thrust is counteracting rotation by the position above the c.g.. For the RTP4 the power-on dynamic pressure over the horizontal stabilizer is affecting the limit positively, showing the increase in tail lift capacity.

An interesting observation is made for the take-off rotation of RTP2 in Figure 6.4b. Just from the scissor plot one can identify the position of the main gear to be less tied to the wing position. In fact, this high-wing configuration integrates the landing gear in a ventral fairing, allowing for independent positioning of the wing. As such the rotation limits are not close to being limiting for this configuration.

Lastly the sole scissor plot for which slipstream effects did not influence tail sizing directly is shown, representing performance of RTP4 in Figure 6.4d. Here all limits are regarding the power-off conditions as power-on would result in the aforementioned beneficial effect of a strong increase in dynamic pressure over the horizontal tail. With a main wing clear of any propeller effect all limits are allowing for a decrease in tail area in power-on conditions. The lower the free stream velocity, the more the beneficial effects of this dynamic pressure are visible as shown by comparing cruise power-on stability to those depicting the same limit in take-off and landing. This is in line with the observations made for the Fokker 50(I) verification data of Figure 5.7.

The design insight a power-on scissor plot provides is invaluable in case the power-on case is restrictive on the horizontal tail design space but can be of great importance in future research for configurations restricted by the power-off scenario. The limit lines indicate a design can be improved if sized for the power-on case, allowing for a smaller horizontal tail surface area which will be beneficial in terms of aircraft mass and wetted area. As a result the power-on sized aircraft can show significant increases in performance relative to the current situation. As an example, if the 60% c.g. excursion in Figure 6.4d can be limited by power-on scenarios one can see the tail surface area can be significantly reduced without violating the limits on stability, equilibrium and rotation.

6.1.3. Performance Assessment

With the scissor plot sizing shown the basis for the RTP performance assessment is created. This performance is captured in a set of KPIs which are presented for the four RTP aircraft in Table 6.3. The KPIs allow for an equal comparison of the designs and relate to predicted performance of these aircraft.

The first of this is aircraft MTOM. The second is the fuel efficiency of the design, which is assessed using the fuel consumption per passenger per 100 kilometers. Any decrease in fuel consumption results in a decrease of direct operating cost (DOC) over the lifetime of the aircraft .[1] The drag area S_D is used as a dimensionless drag metric allowing comparison of different geometries. Finally the cruise lift-over-drag ratio and the values for trim drag during cruise are used as KPIs as these indicate the aerodynamic performance of the aircraft. Trim drag is determined for the most forward c.g. position which is the most unfavorable in terms of stabilizer lift requirement for aft stabilizers as presented in

Chapter 5. All drag coefficients are presented in drag counts with 1 drag count equaling $C_D \times 10^-5$.

Table 6.3: Key Performance Indicators for RTP configurations

Aircraft	**MTOM** $[t]$	**OEM** $[t]$	**MFM** $[t]$	**Fuel burn**	$\left(\frac{L}{D}\right)_{\max}$ $[-]$	S_D $[-]$	$C_{D_{trim}}$ * $[cts]$
RTP1	47	25	7.3	1.90	18.9	7.9×10^{-3}	7.9
RTP2	46	25	7.0	1.82	19.4	7.9×10^{-3}	8.4
RTP3	49	27	7.6	1.98	18.9	8.2×10^{-3}	26.1
RTP4	49	27	7.6	1.98	18.9	8.1×10^{-3}	19.6

*forward c.g. position, start of cruise

Mass Comparison

The first KPIs shown relate to the mass of the aircraft and a goal should be to minimize this for any aircraft design. All aircraft masses are comparable, with a minor increase in OEM for the two configurations with aft-placed engines, RTP3 & RTP4. The aircraft OEM is further broken down to show the component mass breakdown of Figure 6.5. For all aircraft positive feedback is responsible for a total increase in OEM where any mass addition requires an increase in structural strength. This increase in strength requires a lift increase which will result in additional wetted area and fuel burn. All these effects further increase the mass of the aircraft to satisfy the top level requirements and the harmonic mission.

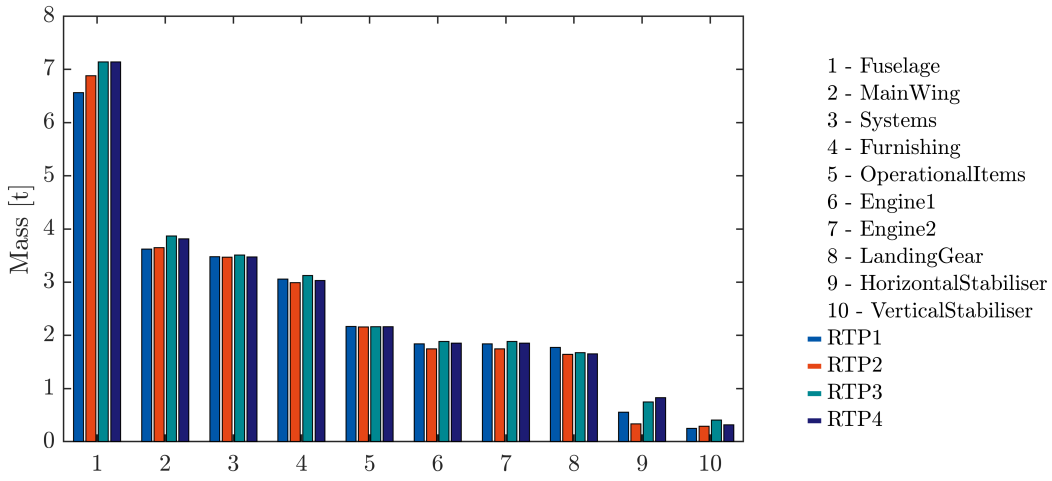

Figure 6.5: Class II component OEM breakdown for the RTP configurations

Standout differences in masses in Figure 6.5 are the 5% increase in wing weight for RTP3 and RTP4, relative to RTP1. This increase is resulting from the aft placement of the engines. As such the weight of these engines do not provide a wing bending relief, requiring a stronger and stiffer wing structure reflected in this component weight. Notable is also the mass decrease for the landing gear systems as compared to RTP1 for all other aircraft. The propeller ground clearance is the main reason RTP1 features a higher mass for this system with low wing mounted engines requiring a longer landing gear support. For fuselage masses, a high wing position and T-tail cause fuselage weight to increase for RTP2 compared to RTP1. For this high-wing configuration, the wing does not provide fuselage bending relief resulting in a strengthened fuselage.

A change in engine mass is directly related to the power requirement of this engine as the sizing of turboprop engines is performed using a reference database as depicted in Figure 6.6, showing the applicability of this database for the Europrop engine. As such any increase in engine weight is proportional to the values for the mission fuel mass MFM and fuel metric of Table 6.3: a higher power requirement for an equal mission profile results in an increase in fuel consumption. This power requirement scales up with the weight of the aircraft and the aerodynamic performance of the aircraft.

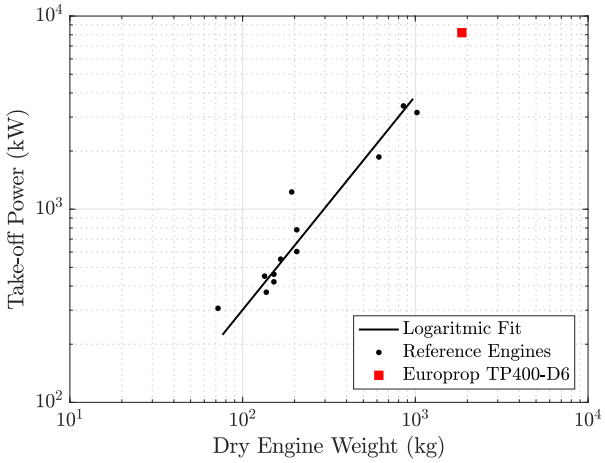

Figure 6.6: Aircraft Design Initiator turboprop engine weight fit

Aerodynamic Performance

This aerodynamic performance is presented by the maximum lift-over-drag ratio and drag area. As such the results show a relation between the aircraft mass, the fuel metric and the maximum lift-over-drag ratio. The cruise drag coefficient breakdown for all RTP aircraft is shown in Figure 6.7.

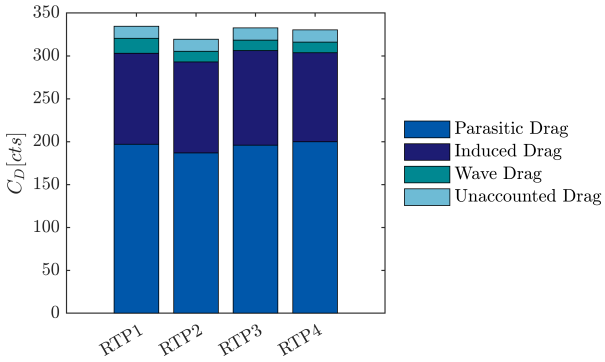

Figure 6.7: Drag area breakdown for the RTP configurations at the start of cruise

Here the values for parasitic drag C_{D0}, lift-induced drag C_{Di} and wave drag C_{Dw} are shown at the start of cruise. The final addition accounts for unaccounted sources of drag $C_{D0_{unacc.}}$ as contamination and roughness of the aircraft surface and is implemented as a fixed value setting in the Aircraft Design Initiator. In order to compare the set of RTP aircraft this drag coefficient is not sufficient as the geometry of the aircraft are incomparable. Therefore, the drag area S_D is used, a value defined in Equation 6.1.

$$S_D = C_D \frac{S_{wet}}{l_F^2} \tag{6.1}$$

The value for S_D in Table 6.3 shows that even for the lowest RTP2 C_D of Figure 6.7 the total drag area is comparable to that of the RTP1 configuration. Both RTP3 and RTP4 show a comparable drag coefficient breakdown when compared to RTP1 where their total drag area is increased. This is fully attributed to the increase in wetted area for these aircraft, most notably due to horizontal stabilizer area differences of these two configurations.

Trim Drag

The next KPI to consider is the trim drag in cruise ($C_{D_{trim}}$). The maximum trim drag is displayed in Table 6.3 for the four configurations, showing two clear trends for this parameter. The initial trend is shown between RTP1 & RTP2 versus RTP3 & RTP4. The latter show a large increase in $C_{D_{trim}}$ which

is a result of the large c.g. excursion of these aircraft. The second trend in $C_{D_{trim}}$ is the difference between a conventional tail and a T-tail configuration. The latter show higher trim drag values, which is believed to be due to the increased offset of the stabilizer. Within the analysis, this change in $C_{D_{trim}}$ is minor when compared to the first trend related to the c.g. excursion. With a trim drag amounting to over 5% of the drag counts at the start of cruise the RTP3 and RTP4 aircraft show that positioning the engines aft strongly affects aerodynamic efficiency in cruise and represent one of the main drawbacks of these aircraft.

Fuel Burn

Lastly the fuel burn for the maximum-passenger harmonic mission is investigated. The previously mentioned fuel burn metric of kilogram fuel burned per passenger per kilometer is presented in Table 6.3. From this it is clear the RTP2 configuration outperforms the RTP1 by 5% and the RTP3 & RTP4 by 10% for the same harmonic mission.

In order to put this number in perspective, the energy metric E_U of the aircraft per ASK of Chapter 2 is determined. For a specific energy for jet fuel of 43MJ/kg E_U is equal to 0.85MJ/ASK for RTP3 and RTP4 and is decreasing to a minimum of 0.78MJ/ASK for RTP2. This value is on par with the most energy-efficient turboprop designs presented by Babikian et. al. [6]. When comparing to the 130-passenger Bombardier CS100 aircraft this aircraft presents a E_U of 1.15MJ/ASK for a similar mission range, decreasing to 0.69 MJ/ASK on maximum harmonic range flights.

Taking this final harmonic mission fuel burn into account, the RTP should be a competitive design for the proposed harmonic range, outperforming existing turboprop aircraft by offering the capability to fly further with more passengers. The RTP is competitive with turbofan aircraft for distances up to the harmonic range of 3000km, providing a more than 30% fuel burn reduction for an increase in flight time of 25% due to the lower cruise velocity and altitude. In order to determine full competitiveness a more detailed analysis of the aircraft operational performance should be performed.

6.2. Sensitivity Analysis

Concluding the search for the competitive RTP a subset of the RTP4 configuration is assessed independently of the three other proposed RTP configurations, changing top level design parameters to identify sensitivities in aircraft sizing and assessment. Such a sensitivity analysis shows possible weaknesses in the converged results as high deviations in KPIs may be identified as substantial risks looking forward to a more detailed design phase. Apart from the basic RTP4 configuration as presented above, the following four reference designs are created:
RTP4$_{CG}$: The c.g. excursion in flight of this aircraft is limited in operation to offset the aft engine placement.
RTP4$_{NLF}$: The main wing friction drag coefficient in cruise is decreased with to show the impact of natural laminar flow (NLF) flow over this surface. Absence of wing-mounted engines allows for undisturbed flow over the main wing in the form of NLF, decreasing the friction drag on this surface.[1]
RTP4$_{SFC}$: The thrust-specific fuel consumption (SFC) of the turboprop engine is reduced to reflect a decrease in propulsive efficiency.
RTP4$_{SM}$: The static margin SM is increased from the allowing 2% to a more conventional value of 5%.

In the end, the sensitivity analysis covers both aerodynamic & propulsive advancements as well as the effect of imposing more stringent operational limits on the design. A robust design shows little deviation from the initial RTP4 design, future-proofing the configuration to allow for changes in technology over the lifetime of the aircraft. A low sensitivity also indicates the obtained results from the Initiator are expected to converge for the same design for a specific set of inputs, an invaluable feat of this conceptual design software. The resulting aircraft KPIs are shown in Table 6.4 with the RTP4 parameters from before present for reference. Note that all settings and design choices from Section 6.1.1 are still valid unless stated otherwise.

Table 6.4: Key performance indicators for converged Initiator RTP4 sensibility configurations

Aircraft	**MTOM** $[t]$	**OEM** $[t]$	**MFM** $[t]$	**Fuel burn**	$\left(\frac{L}{D}\right)_{\max}$ $[-]$	S_D $[-]$	$C_{D_{trim}}$ * $[cts]$
RTP4	49	27	7.6	1.98	18.9	8.1×10^{-3}	19.6
$RTP4_{CG}$	49	27	7.6	1.98	18.9	8.1×10^{-3}	19.6
$RTP4_{NLF}$	48	26	7.4	1.92	19.2	8.0×10^{-3}	19.5
$RTP4_{SFC}$	49	27	7.6	1.98	18.9	8.1×10^{-3}	19.6
$RTP4_{SM}$	50	27	7.8	2.03	18.8	8.3×10^{-3}	19.6

*forward c.g. position, start of cruise

6.2.1. Operational Limit

The first modification was limiting the loading diagram of the RTP4 aircraft. The aft placement of engines results in a skewed loading diagram as was shown before. The limited loading diagram is presented in Figure 6.8.

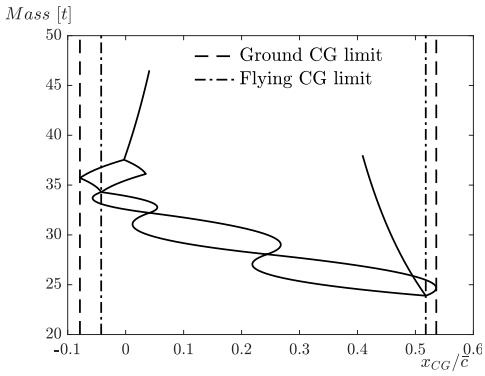

Figure 6.8: RTP4 loading diagram with imposed limits on the flying c.g. excursion

The minor result from limiting the aircraft c.g. relative to the original RTP4 is the c.g. excursion reduction from 61% mac to 56% mac. For the RTP4 the ground and flying limits coincided at the extremities of the loading diagram where now the flying excursion has been limited. This can be seen as a restriction on loading procedure which prevent the full theoretical forward or aft c.g.. The reduction of 5% c.g. excursion results in a slight reduction of tail area ratio S_H/S. This should result in a minor drag and weight reduction visible throughout the aircraft KPIs of Table 6.4.

In reality, the difference is minor and the rounded results obscure the advantages to be gained. Overall the design is still defined by the skewed loading diagram and a major flying c.g. limitation is expected to potentially affect the performance favorably, requiring further analysis for application of such limits.

6.2.2. Aerodynamic Performance

The second modification made is the reduction of main wing friction drag. This reduction is in place to simulate the effects ofNLF over this wing and shows the potential gains in aerodynamic performance to be gained here. It is important to state that NLF was not analyzed as such by the Initiator, instead the wing friction drag contribution was lowered by nine drag counts for the extent of the cruise phase. According to research by Paduano this reduction is the maximum achievable reduction of wing friction drag where no decrease in maximum lift capacity of the surface is occurring.[25]

The converged RTP_{NLF} shows the best results out of all sensitivity designs, represented directly in the lowered aircraft and fuel masses of Table 6.4. This reduction stems from increased aerodynamic performance where the S_D is decreased due to a combination of a reduction in parasitic drag $C_{D,0}$ and the overall lower aircraft mass, representing a decrease in wetted area. The final fuel burn metric and cruise trim drag are lowered for this design, showing the promise of employing NLF on future designs.

6.2.3. Propulsion System Performance

As a third property the effect of power-plant efficiency is determined. The Aircraft Design Initiator SFC for turboprop engines is lowered by a total of 20% for this RTP4 design. The result is an aircraft with equal KPIs to the original RTP4, leading to the conclusion the design is strongly insensitive to changes in SFC. The main reason for this is explained in the assessment criteria. Since the harmonic mission is taken as the design mission the fuel present is not equal to the maximum fuel capacity of the aircraft. In case of a change in engine SFC the amount of fuel required for this mission will change, however, this will not be driving the volume requirement of the main wing. This means aircraft geometry will be unaffected by this change, resulting in a similar OEM.

6.2.4. Change in Static Margin

The last sensitivity tested is the effect of the SM on the design. The RTP designs are all created with a more relaxed static stability margin of 2%mac which is increased to a more conventional value of 5%mac for RTP4$_{SM}$. This has a direct consequence in the scissor plot as all stability limits will be more restrictive for the aft c.g. in tail surface design space. As a result tail surface area is increased for this setting. The KPIs of Table 6.4 show that the increase in static margin relates directly in an increase in aircraft masses, requiring more fuel to fulfill the design mission. The aerodynamic efficiency of the design is shown to decrease with an increased drag area and lowered maximum lift-over-drag ratio, showing the influence of the SM. To benefit from this effect one would need to decrease the SM further for the presented RTPs which would venture into the application of relaxed static stability on these aircraft.

To conclude it is shown the sensitivity of the designed RTP4 configuration to the values investigated is low, resulting in consistent convergence with similar characteristics. Marginal changes in performance for changes in aerodynamic efficiency and top level design choices are present. The design method is considered robust and able to replicate aircraft KPIs for minor changes in the Initiator input settings. As a future opportunity the NLF design shows promising improvements over the baseline RTP4, reducing the fuel metric and increasing the aerodynamic efficiency of the design. A combination of the aforementioned design changes can be greatly beneficial to unconventional aircraft, where NLF and relaxed static stability, together with further operational c.g. restrictions, can produce a more competitive design for this tail-heavy configuration.

7

Conclusion & Recommendations

The closing chapter of this thesis shows the conclusions first after which recommendations towards future research and module development are presented.

7.1. Conclusion

The research objective for this thesis was to assess the top-level performance of a turboprop aircraft which features a substantial increase in passenger capacity relative to existing turboprop aircraft. In order to determine this top-level performance a horizontal stabilizer sizing method accounting for propeller forces and slipstream effects is included in the Aircraft Design Initiator. Another uncertainty was the capacity of the Aircraft Design Initiator to design for turboprop aircraft of over one hundred passengers as methods relying on existing databases could show strong discrepancies for such increase in aircraft size.

For the longitudinal stability, equilibrium and rotation takeoff limits the influence of the propeller forces and slipstream manifests itself mostly in the presence of a strong increase in dynamic pressure aft of the propeller. The increased flow velocity impacts lifting surfaces to such an extent that submerging the horizontal stabilizer in this slipstream is shown to be favorable to the limits constraining tail sizing using the implemented scissor plot method. In case such effect is absent on the horizontal stabilizer the influence on the sizing limits is minor. The main manifestation on these limits is present in case the main wing is experiencing high local velocity changes due to presence of the slipstream, a situation present for low-speed flight phases only. For the case of the ATR72-600 aircraft this effect caused the tail sizing to be defined by the stability limit in takeoff condition, slightly increasing the tail area requirement as compared to the conventional method of sizing for stability in cruise.

The capability of the Aircraft Design Initiator to create turboprop aircraft with a passenger capacity over one hundred is shown by the validation case where reverse-engineering of theoretical propfan aircraft was shown attainable. The accuracy of the Aircraft Design Initiator was limited in estimation component and aircraft masses, resulting in an underestimation of total aircraft mass. However, the designed mission was converged to with a similar amount of fuel burn shown for both the reference and the reverse-engineered aircraft. Also, the presented tail sizing limits show a good correspondence for two out of three aircraft. Only the most conventional design of wing-mounted engines showed a significant deviation from the reference.

The effect of engine position on the top-level performance of the aircraft is assessed for the set of RTP aircraft. The set was chosen such that changes in main wing position, tail geometry and engine position are included to derive general design guidelines. The first of these is that engines further aft result in a non-centered aircraft loading diagram. As a result a larger c.g. excursion is present and the horizontal stabilizer area requirement is increased. This further adds mass aft of the aircraft c.g., introducing a positive feedback loop of mass gain in aft-engined aircraft. The results show that these configuration are therefore heavier than configurations with wing-mounted engines for the equal mission performance, requiring additional fuel burn. Furthermore the decrease in tail arm length is resulting in a strong increase in trim drag during cruise relative to wing-mounted engine configurations.

As a result the conclusion is that for the 130-passenger RTP a wing-mounted engine configuration is favored over the other investigated configurations. The normalized fuel burn shows to be on-par with the more efficient existing turboprop designs and is highly competitive with large turbofans on the same harmonic mission. The main difference between the low wing and high wing aircraft stem from the c.g. excursion and landing gear design. The first requires the cargo compartments to be separate in the forward and aft fuselage section, clearing the center section for the main wing box. A low wing configuration also introduces an increase in landing gear length to account for the propeller ground clearance, adding weight to this component. The high-wing with wing-mounted engines is presented as the most promising configuration.

Lastly a design sensitivity study accounting for a change in aerodynamic efficiency, propulsive efficiency and operational limits. The application of NLF shows to be most promising but may suffer from the same limitations on stabilizer sizing for power-on. The aircraft should always be satisfying requirements, even for the off-design condition. Overall the process to create and assess the RTP aircraft is proven to be robust and reliable with the change in inputs showing only minor changes relative to the initially generated result.

7.2. Recommendations

The design considerations shown in this thesis form a basis to perform subsequent research which should focus first and foremost on collecting aerodynamic data regarding the power-on situation of large-scale turboprop aircraft with a specific interest in slipstream effects on lifting surfaces. This data should then be used to perform an extensive verification of the implemented methods.

Another recommendation is to investigate the possibility of the sizing for power-on only which would allow for a significant reduction in horizontal stabilizer sizing. One design where the absence of power-off limits may be accounted for is that of an aircraft with a distributed propulsion system.

Lastly the following recommendations are made for future improvement of the Aircraft Design Initiator:

- The horizontal stabilizer sizing method should in the future be expanded with limiting conditions for non-conventional aircraft configurations as to provide an all-in-one preliminary tool to identify risks regarding longitudinal aircraft performance early in the design process. The existing implementation can be easily adopted for canard and three-surface aircraft by applying the same principles as for conventional aircraft. Sizing for more exotic configuration can be implemented by means of surrogate sizing, relating the tail area ratio result of the sizing method to any aircraft component acting as horizontal stabilizer.
- The engine and propeller design method could be expanded upon to include the capability of creating propfan or high-solidity turboprop engines. The current implementation limits the design freedom for the propeller especially by considering the propeller velocity limits only.
- Class II.V weight estimation should be expanded to include all lifting surfaces of the aircraft, not solely the main wing. This is expected to influence the component mass of for instance the horizontal stabilizer in case engines are mounted to this surface. The inclusion of such methods could compensate the presented underestimation of conventional aircraft OEM.
- A close-coupling of landing gear design and horizontal stabilizer sizing could prove beneficial as both require a shift in main wing position to comply with requirements on sizing. As such a certain wing shift routine could be set up which would eliminate the wing optimization routine within horizontal stabilizer sizing.
- The application on operational limits on the aircraft have been briefly investigated by the restrictions imposed on the c.g. excursion. Such operational limits could increase the aircraft KPIs significantly to the point where aircraft that are currently not of interest could become viable. A detailed study into existing limits on commercial aircraft could provide the foundation of implementing these more thoroughly. This could include the operation of the aircraft as an asset for the airliner, incorporating the mission flight time as an important indication of the feasibility to prefer large turboprop configurations over turbofan designs.

- Inclusion of a noise model can be valuable as it introduces another KPI to the Aircraft Design Initiator. For the future, environmental regulations and a high expected customer comfort level could drive the design to specific sound levels, both perceived from outside and in the aircraft cabin.

Bibliography

[1] A. Abbas, J. De Vicente, and E. Valero. Aerodynamic technologies to improve aircraft performance. *Aerospace Science and Technology*, 28(1):100–132, 2013. doi: 10.1016/j.ast.2012.10.008.

[2] C. Alba, A. Elham, B. German, and L.L. Veldhuis. A Surrogate-Based Multi-Disciplinary Design Optimization Framework Exploiting Wing-Propeller Interaction. *AIAA/ISSMO Multidisciplinary Analysis and Optimization Conference*, 18(June):1–25, 2017. doi: 10.2514/6.2017-4329.

[3] Anonymous. *Aerodynamic centre of wing-fuselage combinations*. Data item, Engineering Sciences Data Unit (ESDU), 1976.

[4] Anonymous (IHS Markit). Bombardier CSeries, 2018. URL https://janes.ihs.com/JAWADevelopmentProduction/Reference#. Accessed 15-03-2018.

[5] Anonymous (IHS Markit). Europrop TP400-D6, 2018. URL https://janes.ihs.com/AeroEngines/Reference#. Accessed 09-01-2018.

[6] R. Babikian, S.P. Lukachko, and I.A. Waitz. The historical fuel efficiency characteristics of regional aircraft from technological, operational, and cost perspectives. *Journal of Air Transport Management*, 8(6):389–400, 2002. doi: 10.1016/S0969-6997(02)00020-0.

[7] Boeing Commercial Airplanes. Current Market Outlook 2015-2034, 2015. URL http://www.boeing.com/resources/boeingdotcom/commercial/about-our-market/assets/downloads/Boeing_Current_Market_Outlook_2015.pdf. Accessed 18-01-2018.

[8] Bombardier Commercial Aircraft. CS100 Fact Sheet, 2016. URL http://commercialaircraft.bombardier.com/en/cseries/Literature.html.

[9] T. Bouquet. *Modelling the Propeller Slipstream Effect on the Longitudinal Stability and Control*. Master's thesis, Delft University of Technology, 2016.

[10] T. Bouquet and R. Vos. Modeling the Propeller Slipstream Effect on Lift and Pitching Moment. *AIAA Aerospace Sciences Meeting*, 55(January):1–15, 2017. doi: 10.2514/6.2017-0236.

[11] M.T.H. Brown. *Conceptual Design of Blended Wing Body Airliners*. Master's thesis, Delft University of Technology, 2017.

[12] J.P. Campbell and M.O. McKinney. Summary of Methods for Calculating Dynamic Lateral Stability and Response and for Estimating Lateral Stability Derivatives. Technical report, National Advisory Committee for Aeronautics, Langley Field, 1951.

[13] F.M. Catalano and F.M. Costanzo. Theoretical and experimental analysis of the fuselage influence on the wing aerodynamic center position at low speed conditions. In *International Congress of Mechanical Engineering*, number 22, pages 2089–2100. ABCM, 2013.

[14] J. De Young. Propeller at High Incidence. *Journal of Aircraft*, 2(3):241–250, May 1965. doi: 10.2514/3.43646.

[15] M. Drela and H. Youngren. AVL (Athena Vortex Lattice), 2017. URL http://web.mit.edu/drela/Public/web/avl/.

[16] R. J. M. Elmendorp. *Synthesis of Novel Aircraft Concepts*. Master's thesis, Delft University of Technology, 2014.

[17] Anonymous (European Aviation Safety Agency). Certification Specifications and Acceptable Means of Compliance for Large Aeroplanes CS-25, 2016. URL https://www.easa.europa.eu/document-library/certification-specifications/cs-25-amendment-20. Accessed 14-12-2017.

[18] R.D. Finck. *USAF (United States Air Force) Stability and Control DATCOM (Data Compendium)*. Technical report, McDonnell Aircraft Co., St. Louis, 1978.

[19] I. M. Goldsmith. *A study to define the research and technology requirements for advanced turbo/propfan transport aircraft*. Technical report, McDonnell Douglas Corporation, 1981.

[20] Q. Jansen. *Relaxed Static Stability Performance Assessment on Conventional and Unconventional Aircraft Configurations*. Master's thesis, Delft University of Technology, 2015.

[21] A.K. Kundu. *Aircraft Design*. Cambridge University Press, Cambridge, 1st edition, 2010. ISBN 9780511844652.

[22] B.W. McCormick. *Aerodynamics, aeronautics, and flight mechanics*. John Wiley, New-York, 1995. ISBN 978-0471110873.

[23] E. Obert. *A Method for the Determination of the Effect of Propeller Slipstream on the Static Longitudinal Stability and Control of Multi-Engined Propeller Aircraft*. Delft University Press, Delft, 1997. ISBN 90-407-1577-7.

[24] E. Obert. *Aerodynamic Design of Transport Aircraft*. IOS Press, Delft, The Netherlands, 1st edition, 2009. ISBN 978-1-58603-970-7.

[25] C. Paduano. *Aerodynamic Shape Optimization of a Natural-Laminar Flow Wing*. Master's thesis, Università Degli Studi di Napoli Federico II, Napoli, 2015.

[26] J. Roskam. Part II: Preliminary configuration design and integration of the propulsion system. In *Airplane design*, page 324. DARcorporation, Ottowa, KS, 1985. ISBN 978-1884885433.

[27] E. Torenbeek. *Synthesis of subsonic airplane design*. Delft University Press, 1976. ISBN 90-298-2505-7.

[28] N.H.M. Van den Dungen. *Synthesis of an Aircraft Featuring a Ducted-Fan Propulsive Empennage*. Master's thesis, Delft University of Technology, 2017.

[29] L.L.M. Veldhuis. *Propeller wing aerodynamic interference*. Dissertation, Delft University of Technology, 2005.

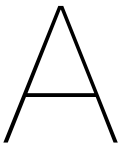

Initiator Code Changes

This appendix summarizes the changes that were made to the Aircraft Design Initiator. The changes are listed as a removal, change or addition per module of the main trunk. The order is presented alphabetically in order of folder - module - function.

For a detailed syntax of functions and their role in the determination of the turboprop sizing the reader is referred to the additional information present in the module `run.m` files. These files also include further recommendations based on existing limitations of the implementation.

AnalysisModules

@Class2WeightEstimation

Modified

- `getLoadingCGRange.m` - included optional setting trigger to limit flying c.g.

@DigitalDatcom

Modified

- `run.m` - path definition independent of operating system

@EngineModel

Modified

- `run.m` - changed hardcoded SFC to use setting file SFC

@WaveDragEstimation

Modified

- `ADFuselageFairingEst.m` - path definition independent of operating system
- `ESDUcorrelations.m` - path definition independent of operating system
- `FuselageWaveDragTransonic.m` - path definition independent of operating system

CleanInputFiles

Added

- `ATR72-600.xml` - Aircraft definition file of ATR72-600 with conventional tail geometry
- `DC9Mod1.xml` - Aircraft definition file of Goldsmith DC-9 Super 80 Modification 1
- `DC9Mod2.xml` - Aircraft definition file of Goldsmith DC-9 Super 80 Modification 2

- `DC9Mod3.xml` - Aircraft definition file of Goldsmith DC-9 Super 80 Modification 3
- `RTP1.xml` - Aircraft definition file of RTP1 configuration
- `RTP2.xml` - Aircraft definition file of RTP2 configuration
- `RTP3.xml` - Aircraft definition file of RTP3 configuration
- `RTP4.xml` - Aircraft definition file of RTP4 configuration
- `RTP4_CG.xml` - Aircraft definition file of RTP4 configuration for sensitivity study
- `RTP4_NLF.xml` - Aircraft definition file of RTP4 configuration for sensitivity study
- `RTP4_SFC.xml` - Aircraft definition file of RTP4 configuration for sensitivity study
- `RTP4_SM.xml` - Aircraft definition file of RTP4 configuration for sensitivity study
- `settings_ATR72-600LT.xml` - Settings file of ATR72-600 with conventional tail geometry
- `settings_DC9Mod1.xml` - Settings file of Goldsmith DC-9 Super 80 Modification 1
- `settings_DC9Mod2.xml` - Settings file of Goldsmith DC-9 Super 80 Modification 2
- `settings_DC9Mod3.xml` - Settings file of Goldsmith DC-9 Super 80 Modification 3
- `settings_RTP1.xml` - Settings file of RTP1 configuration
- `settings_RTP2.xml` - Settings file of RTP2 configuration
- `settings_RTP3.xml` - Settings file of RTP3 configuration
- `settings_RTP4.xml` - Settings file of RTP4 configuration
- `settings_RTP4_CG.xml` - Settings file of RTP4 configuration for sensitivity study
- `settings_RTP4_NLF.xml` - Settings file of RTP4 configuration for sensitivity study
- `settings_RTP4_SFC.xml` - Settings file of RTP4 configuration for sensitivity study
- `settings_RTP4_SM.xml` - Settings file of RTP4 configuration for sensitivity study

Modified

- `ATR72-600.xml` - Aircraft definition file of ATR72-600
- `F50.xml` - Aircraft definition file of Fokker 50
- `settings_ATR72-600.xml` - Settings file of ATR72-600
- `settings_F50.xml` - Settings file of Fokker 50

DesignModules

@HorizontalStabilityEstimation

Added

- `CreateFlightCases.m` - sets flight conditions and configuration for later analysis
- `DownWash.m` - cycles through flight cases to determine affected lifting surface geometry
- `ESDU76015F1.m` - ESDU76015 carpet plot to determine factor F
- `ESDU76015F2.m` - ESDU76015 carpet plot to determine factor G
- `ESDU76015F3A.m` - ESDU76015 carpet plot to determine factor K1A
- `ESDU76015F3B.m` - ESDU76015 carpet plot to determine factor K1B
- `ESDU76015F3C.m` - ESDU76015 carpet plot to determine factor K1C

- `ESDU76015F4.m` - ESDU76015 carpet plot to determine factor K2
- `LLT.m` - apply slipstream lift to lifting surface & determine downwash angle of slipstream
- `ProcessPowerOff.m` - process AVL data to power-off aerodynamics
- `ProcessPropPower.m` - process power-on effects & apply power-on affects to flight case
- `PropNormalForce.m` - determine propeller normal force gradient and slipstream deflection angle
- `SlipSection.m` - determine geometry of slipstream impacting lifting surface
- `LLT.m` - apply slipstream lift to lifting surface & determine downwash angle of slipstream

Modified

- `FlapLiftMoment.m` - included input check to allow for determination of power-on performance
- `FlowInterference.m` - included input check to use provided free stream Mach & added additional function output `Flow` containing AVL output struct
- `HorizontalStabilityEstimation.m` - included newly added functions to the class definition
- `InputVariables.m` - included optional setting for static margin with default fallback value & included K-factor for nacelle on horizontal stabilizer & calculate effective propeller power
- `NACAFIG1098.m` - previous version of digitized surface reworked to stand-alone function
- `run.m` - total rework of the 'turboprop' case using scissor plot sizing including power-on effects
- `StabilityAero.m` - inclusion of all power-on cases & fuselage contribution to a.c.
- `TailObjective.m` - inclusion of all power-on cases & aircraft-minus-tail lift gradient & newly derived takeoff rotation requirement & update of scissor plot and trim diagram plotting

Removed

- `PropNormForce.m` - undocumented implementation of propeller normal force calculation. Replaced with `PropNormalForce.m`

SizingModules

@GeometryEstimation

Modified

- `estimatePylons.m` - included swept pylon geometry to clear turboprop engine
- `positionEngines.m` - included option for horizontal stabilizer placement of engines

Validation

ReferenceImages

Added

- folder:`ATR72600` - top, front and side view of ATR72-600 (jpeg-format)
- folder:`F50` - top, front and side view of Fokker 50 (jpeg-format)

Modified

- `ImageScalingFactors.mat` - included scaling factors for ATR72-600 and Fokker 50

B

Aircraft Design Initiator Input Files

This appendix presents the `.xml` file used as input for the Aircraft Design Initiator. The example provided is valid for the RTP4 aircraft configuration which incorporates turboprop engines mounted to the horizontal stabilizer.

```
<?xml version="1.0" encoding="utf-8"?>
<initiator xmlns:xsi="http://www.w3.org/2001/XMLSchema-instance"
    xsi:noNamespaceSchemaLocation="initiator.xsd">
  <aircraft>
    <name>RTP4</name>
    <description>Empty Initiator file - Regional Turboprop 4 Configuration</description>
    <missions default="Max payload">
      <mission name="Max payload">
        <requirement>
          <name>Pax</name>
          <value>130</value>
        </requirement>
        <requirement>
          <name>PayloadMass</name>
          <value>13650</value>
        </requirement>
        <requirement>
          <name>CruiseMach</name>
          <value>0.6</value>
        </requirement>
        <requirement>
          <name>Altitude</name>
          <value>8500</value>
        </requirement>
        <requirement>
          <name>Range</name>
          <value>2960</value>
        </requirement>
        <requirement>
          <name>TakeOffDistance</name>
          <value>1350</value>
        </requirement>
        <requirement>
          <name>LandingDistance</name>
          <value>1350</value>
        </requirement>
        <requirement>
          <name>NumberOfFlights</name>
          <value>100000</value>
        </requirement>
        <requirement>
          <name>AirworthinessRegulations</name>
          <value>FAR-25</value>
        </requirement>
        <requirement>
          <name>TimeToClimb</name>
          <!-- Time to climb to a specified altitude -->
          <value mapType="vector">15;5500</value>
```

```
48            <!-- Time [minutes] ; Altitude [meter]      -->
49          </requirement>
50          <requirement>
51            <name>LoiterTime</name>
52            <value>30</value>
53          </requirement>
54          <requirement>
55            <name>DivRange</name>
56            <value>185.2</value>
57          </requirement>
58          <requirement>
59            <name>AirportClassification</name>
60            <value>FAA-VI</value>
61          </requirement>
62        </mission>
63      </missions>
64      <performance>
65        <parameter>
66          <name>LDmax</name>
67          <value>18</value>
68        </parameter>
69        <parameter>
70          <name>CruisePropEfficiency</name>
71          <value>0.9</value>
72        </parameter>
73        <parameter>
74          <name>ClimbPropEfficiency</name>
75          <value>0.9</value>
76        </parameter>
77      <parameter>
78          <name>TakeOffPropEfficiency</name>
79          <value>0.75</value>
80        </parameter>
81        <parameter>
82          <name>BSFC</name>
83          <value>300</value>
84        </parameter>
85        <parameter>
86          <name>SFC</name>
87          <value>0.5</value>
88        </parameter>
89        <parameter>
90          <name>FFStartUp</name>
91          <value>0.990</value>
92        </parameter>
93        <parameter>
94          <name>FFTaxi</name>
95          <value>0.990</value>
96        </parameter>
97        <parameter>
98          <name>CLmaxLanding</name>
99          <value>3.0</value>
100       </parameter>
101       <parameter>
102         <name>CLmaxTakeOff</name>
103         <value>2.4</value>
104       </parameter>
105       <parameter>
106         <name>CLmaxClean</name>
107         <value>1.6</value>
108       </parameter>
109     </performance>
110     <configuration>
111       <parameter>
112         <name>WingAspectRatio</name>
113         <value>11.0</value>
114       </parameter>
115     <parameter>
116         <name>HasKink</name>
117         <value>1</value>
118       </parameter>
```

```
119         <parameter>
120           <name>TEinboardSweep</name>
121           <value>4</value>
122         </parameter>
123         <parameter>
124           <name>WingLocation</name>
125           <value>Low</value>
126         </parameter>
127         <parameter>
128           <name>TailType</name>
129           <value>Cruciform</value>
130         </parameter>
131         <parameter>
132           <name>RootAirfoil</name>
133           <value>N663418</value>
134         </parameter>
135         <parameter>
136           <name>KinkAirfoil</name>
137           <value>N663418</value>
138         </parameter>
139         <parameter>
140           <name>TipAirfoil</name>
141           <value>N662415</value>
142         </parameter>
143         <parameter>
144           <name>Freight</name>
145           <value>true</value>
146         </parameter>
147         <parameter>
148           <name>FuselageTank</name>
149           <value>false</value>
150         </parameter>
151       <parameter>
152       <name>CompositeStructures</name>
153       <!-- Fuselage,Wing,Empennage-->
154       <value mapType="vector">0;1;1</value>
155       </parameter>
156       </configuration>
157       <parts mainPart="Fuselage">
158         <fuselage name="Fuselage" type="Conventional">
159           <paxDivision mapType="vector">1</paxDivision>
160           <!-- should sum to 1 -->
161           <!-- Dimensions: Seat width, arm rest width, seat pitch, seatbackspace, legspace
                (last 2 unused) -->
162           <cabins>
163             <cabin name="Cabin1">
164               <class>
165                 <name>EC</name>
166                 <seatingArr mapType="vector">2;3</seatingArr>
167                 <seatingDim mapType="vector">0.43;0.05;0.722;0.40;0.3</seatingDim>
168               </class>
169               <classDistribution mapType="vector">0;0;0;1</classDistribution>
170             </cabin>
171           </cabins>
172       </fuselage>
173       <wing name="Main Wing" type="MainWing">
174             </wing>
175       <wing name="Horizontal Stabiliser" type="HorizontalTail">
176             </wing>
177       <wing name="Vertical Stabiliser" type="VerticalTail">
178             </wing>
179       <engine name="Engine-1" type="TurboProp">
180         <location>Horizontal Stabiliser</location>
181       <!-- Fan (for turbofan,turboprop,ducted fan, etc.) -->
182       <fan>
183         <name>F568</name>
184         <NoBlades>10</NoBlades>
185       </fan>
186       </engine>
187      <engine name="Engine-2" type="TurboProp">
188         <location>Horizontal Stabiliser</location>
```

```
189         <!-- Fan (for turbofan,turboprop,ducted fan, etc.) -->
190         <fan>
191           <name>F568</name>
192           <NoBlades>10</NoBlades>
193         </fan>
194         </engine>
195       </parts>
196     </aircraft>
197     <runList>DesignConvergence,ReportWriter,PlotTool</runList>
198     <settings source="settings_RTP4.xml">
199       </settings>
200     <moduleInputs>
201       <input module="PlotTool">
202         <plotModules>Geometry,DesignConvergence</plotModules>
203       </input>
204     <input module="GeometryEstimation">
205         <WingTcRatios mapType="vector">0.18;0.16;0.13</WingTcRatios>
206       <WingSweep>12.5</WingSweep>
207       </input>
208     <input module="FuselageConfigurator">
209         <Circularity>0.80</Circularity>
210       </input>
211     </moduleInputs>
212 </initiator>
```

C

ATR72-600 (I) Report

The aircraft is a conventional aircraft with a wing aspect ratio of 11.95. The aircraft is designed to transport 68 passengers with a total payload mass of 7500kg over 1528km.

Specification

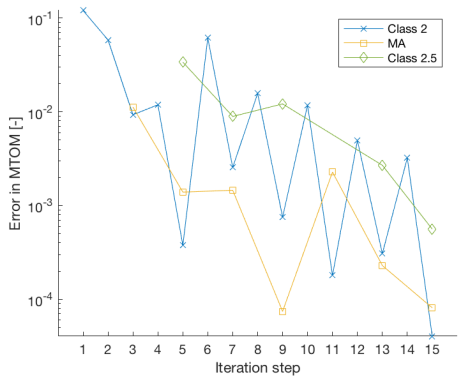

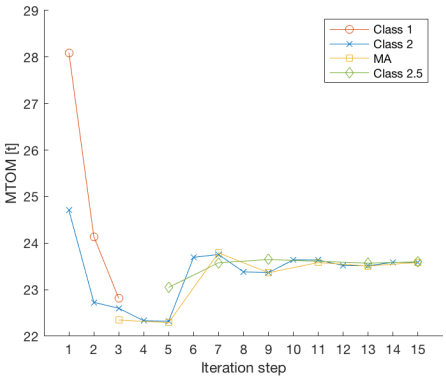

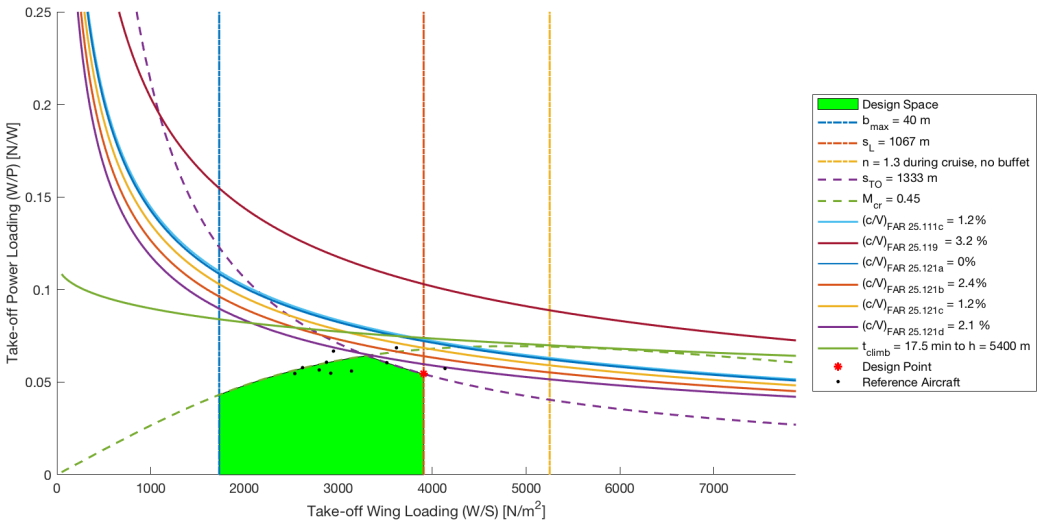

Pax	68	~
Payload Mass	7500	kg
Cruise Mach	0.45	~
Altitude	8000	m
Range	1528	km
Take Off Distance	1333	m
Landing Distance	1067	m
Wing loading (MTOM)	3913	N/m^2
Power Loading	0.0543	~

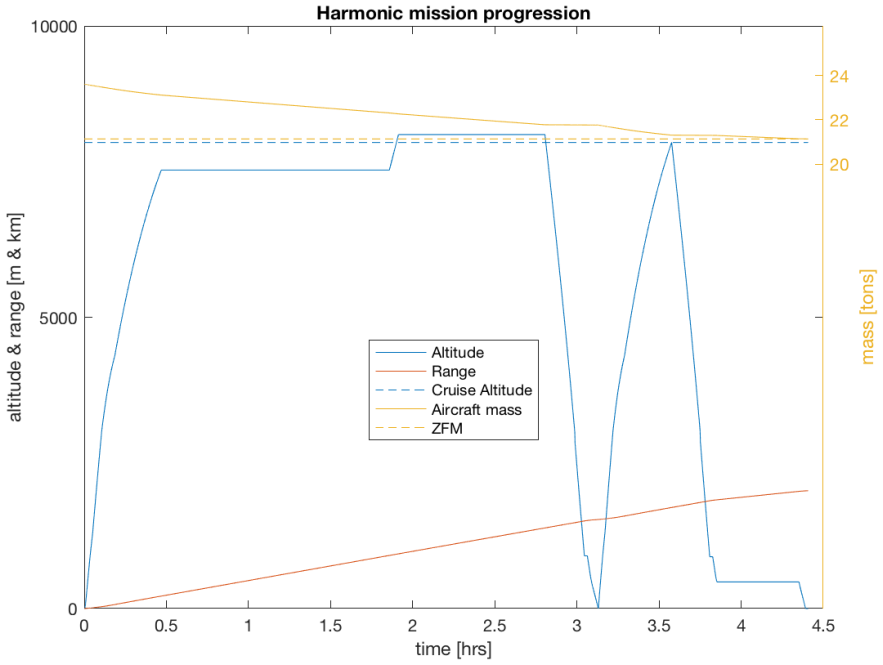

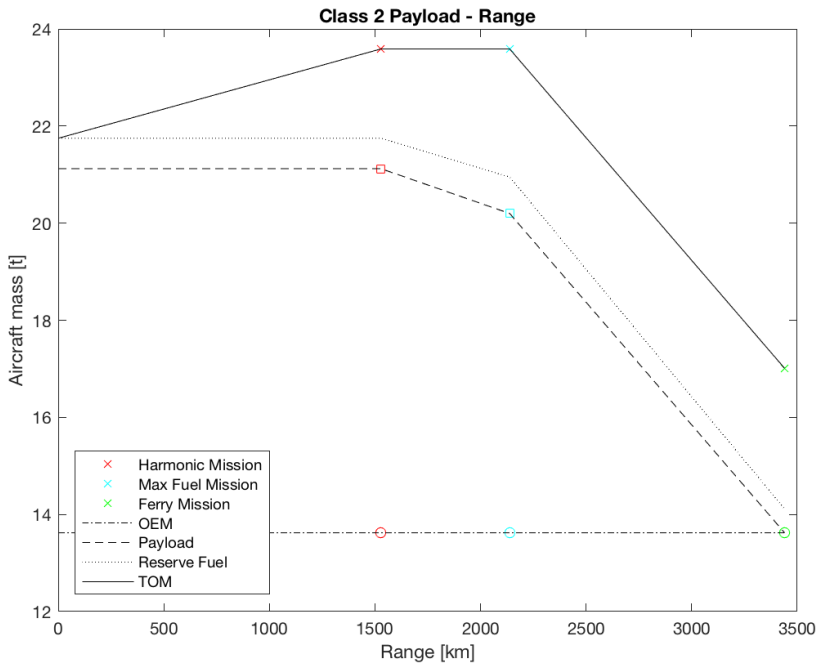

Weight Estimation

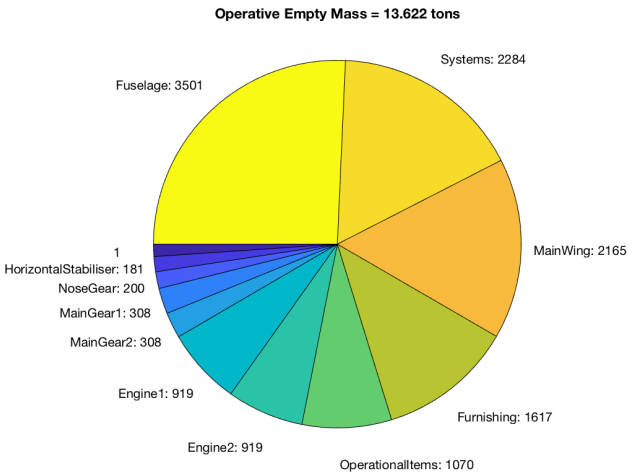

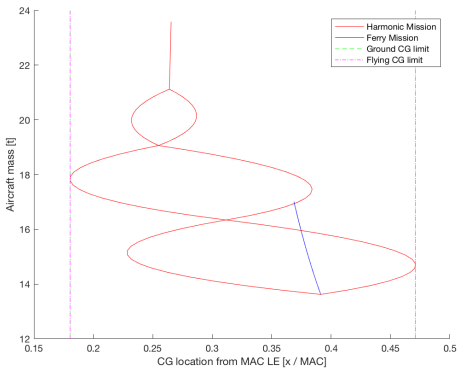

Table C.1: Mass Summary

Maximum take-off mass	23590	kg
Operational empty mass	13625.2199	kg
Design landing mass	21750	kg
Maximum landing mass	21620	kg
Maximum ramp mass	24070	kg
Maximum fuel mass (ferry)	3400	kg
Harmonic range mission:		
Payload mass	7500	kg
Total fuel mass	2.500	kg
Max payload mission:		
Payload mass	7500	kg
Total fuel mass	2.500	kg
Reserve fuel mass	700	kg

Table C.2: Centre-of-gravity locations

X_{cg} (MTOM)	12.3	m
X_{cg} (OEM)	12.6	m
X_{cg} (ZFM)	12.6	m
X_{np}	14.1	m

Aerodynamics

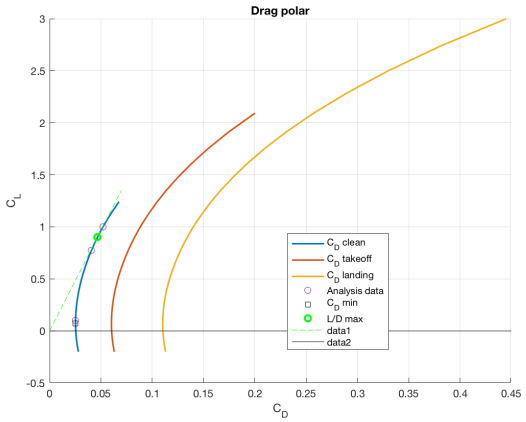

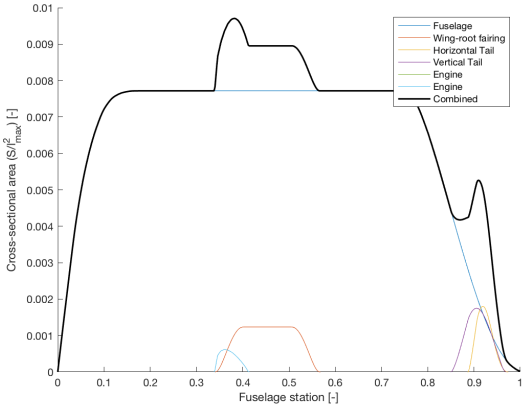

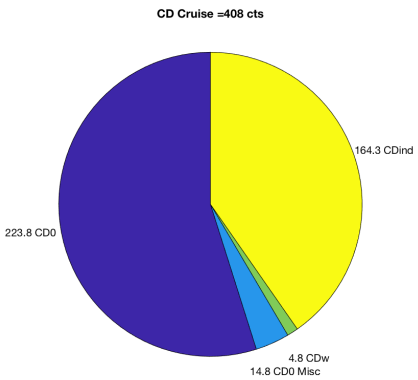

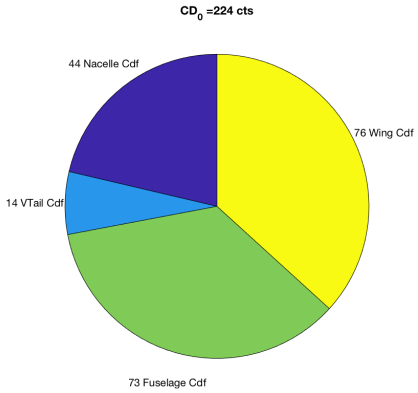

Table C.3: Aerodynamic Properties

$C_{L,\text{cruise}}$	0.78	~
$C_{D,\text{cruise}}$	412	cts
L/D_{cruise}	18.8	~
C_{D_0} (Clean)	255	cts
C_{D_0} (Take-Off)	604	cts
C_{D_0} (Landing)	1104	cts
Oswald factor (e) (Clean)	0.973	~
Oswald factor (e) (Take-Off)	0.923	~
Oswald factor (e) (Landing)	0.873	~
C_{L_α}	6.39	rad^{-1}
C_{m_α}	-4.81	rad^{-1}
$C_{L_{\text{max,clean}}}$	1.33	~
$C_{L_{\text{max,take-off}}}$	2.2	~
$C_{L_{\text{max,landing}}}$	3.2	~

Aircraft Geometry

Table C.4: Propulsion

Number of engines	2	~
SFC_{cruise}	0.513	h^{-1}
Fan diameter	3.91	m
Number of blades	6	~
Diameter	3.91	m
Length	2.34	m

Table C.5: Main Wing dimensions

Span	26.6	m
Planform area	59.57	m^2
MAC	2.54	m
MAC	2.39	m
Root Chord	3.24	m
Root t/c	0.18	~
Tip Chord	1.24	m
Tip t/c	0.13	~
Sections (root to tip)	NACA43018mod NACA43018mod NACA43015mod	
Sweep 0.25c	4.36	°
Taper ratio	0.382	~
Twist	0	°
Dihedral	1.2	°

Table C.6: Horizontal Stabilizer dimensions

Span	8.23	m
Planform area	13.55	m^2
MAC	1.75	m
Root Chord	2.35	m
Root t/c	0.1	~
Tip Chord	0.941	m
Tip t/c	0.1	~
Sections (root to tip)	N0012 N0012	
Sweep 0.25c	2.41	°
Taper ratio	0.4	~
Twist	0	°
Dihedral	1.2	°

Table C.7: Vertical Stabilizer dimensions

Span	4.3	m
Planform area	11.56	m^2
AC	2.74	m
Root Chord	3.36	m
Root t/c	0.12	~
Tip Chord	2.02	m
Tip t/c	0.12	~
Sections (root to tip)	N0012 N0012	
Sweep 0.25c	9.2	°
Taper ratio	0.6	~
Twist	0	°
Dihedral	0	°

Table C.8: Fuselage dimensions

Length	27.9	m
Diameter	2.77	m
Nose Shape Factor	0.15	~
Tail Shape Factor	0.25	~
Nose Length	3.35	m
Tail Length	8.38	~
Aft Ratio Width	0.05	~
Aft Ratio Height	0.05	~

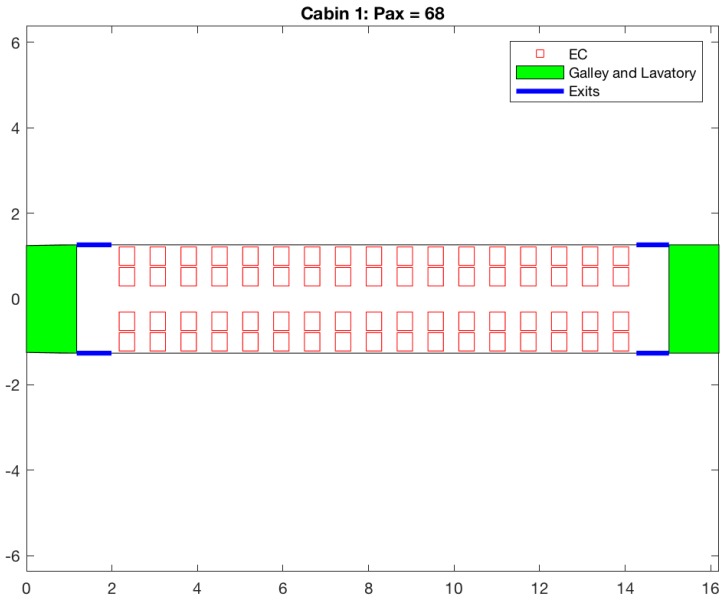

D

Fokker 50(I) Report

The aircraft is a conventional aircraft with a wing aspect ratio of 12. The aircraft is designed to transport 52 passengers with a total payload mass of 5460kg over 1713km.

Specification

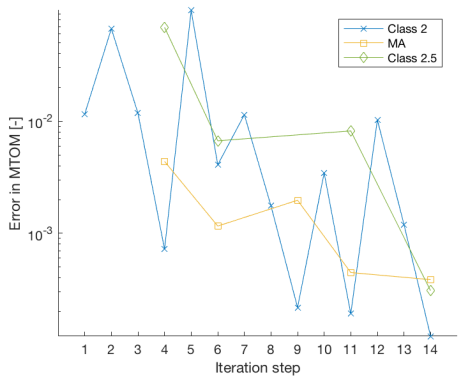

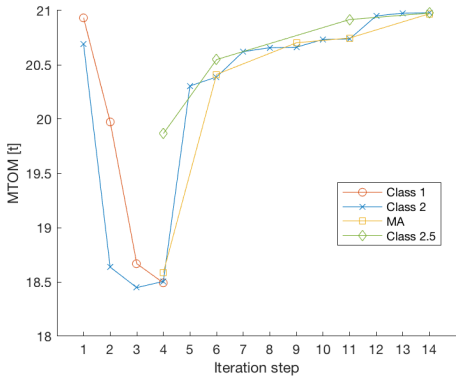

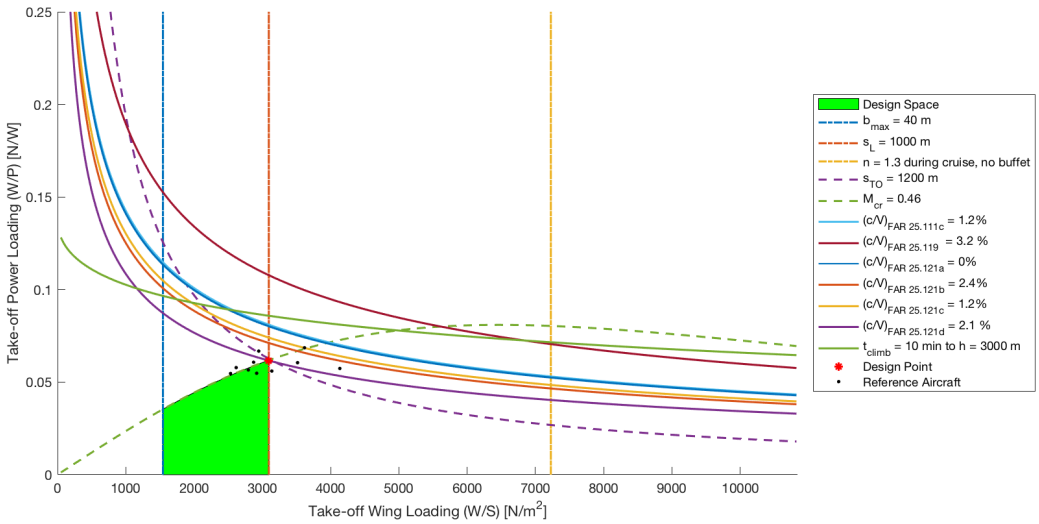

Pax	52	~
Payload Mass	5460	kg
Cruise Mach	0.46	~
Altitude	5970	m
Range	1713	km
Take Off Distance	1200	m
Landing Distance	1000	m
Wing loading (MTOM)	3095	N/m^2
Power Loading	0.0616	~

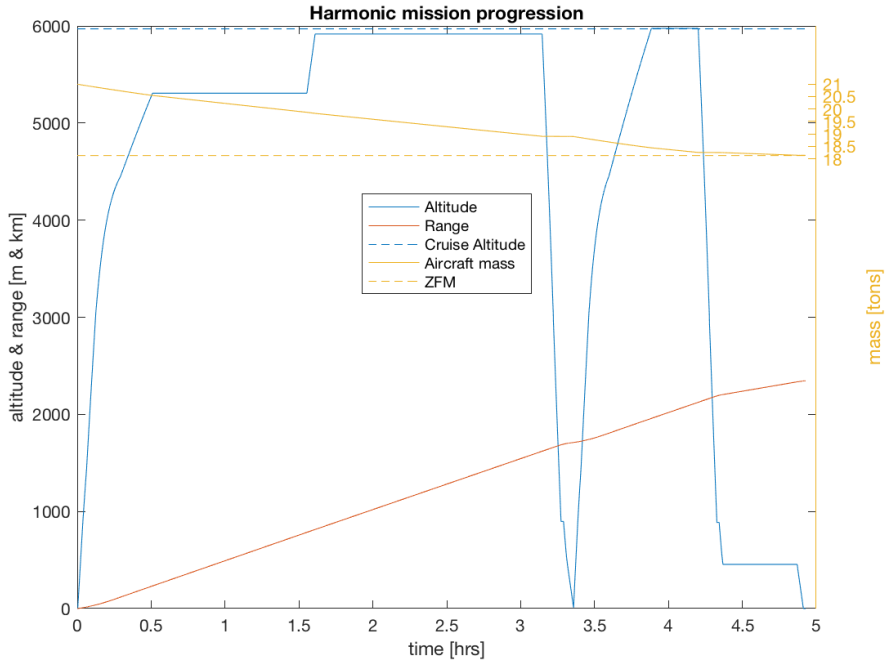

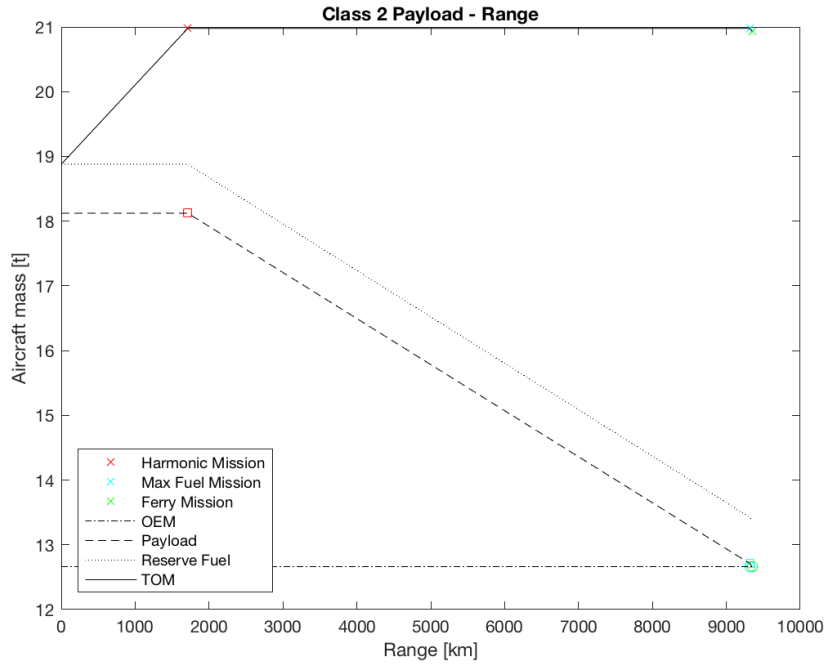

Weight Estimation

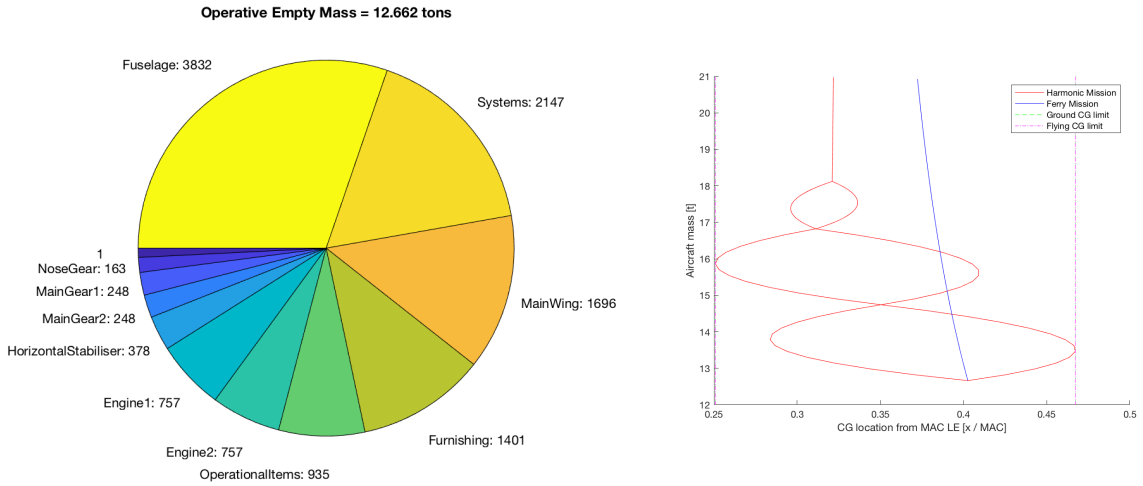

Table D.1: Mass Summary

Maximum takeoff mass	20980	kg
Operational empty mass	12662	kg
Design landing mass	18880	kg
Maximum landing mass	18690	kg
Maximum ramp mass	21400	kg
Maximum fuel mass (ferry)	8300	kg
Harmonic range mission:		
Payload mass	5460	kg
Total fuel mass	2900	kg
Max payload mission:		
Payload mass	5460	kg
Total fuel mass	2900	kg
Reserve fuel mass	880	kg

Table D.2: Centre-of-gravity locations

X_{cg} (MTOM)	11.9	m
X_{cg} (OEM)	12.1	m
X_{cg} (ZFM)	12.1	m
X_{np}	13.5	m

Aerodynamics

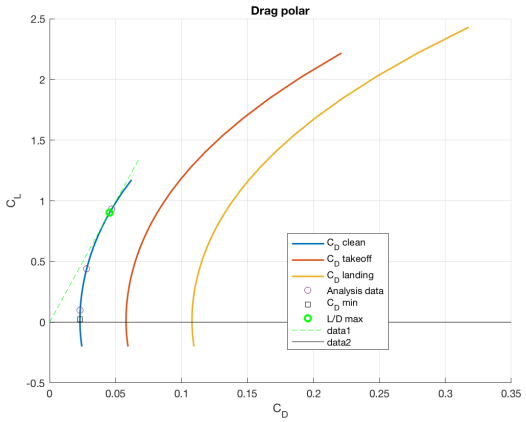

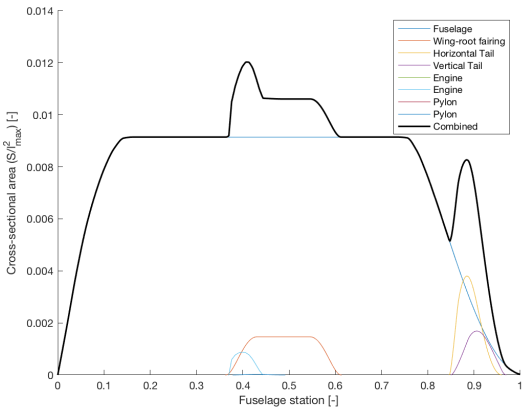

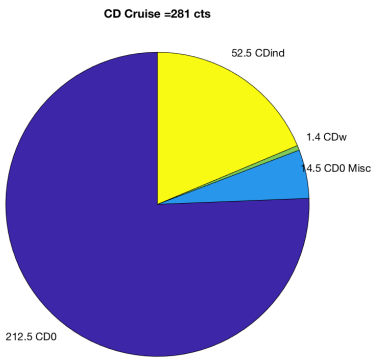

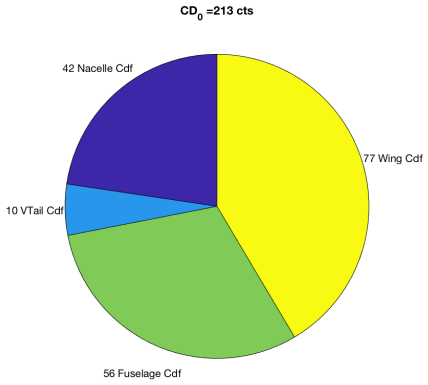

Table D.3: Aerodynamic Properties

$C_{L,\text{cruise}}$	0.44	~
$C_{D,\text{cruise}}$	291	cts
L/D_{cruise}	15.2	~
C_{D_0} (Clean)	230	cts
C_{D_0} (Takeoff)	579	cts
C_{D_0} (Landing)	1079	cts
Oswald factor (e) (Clean)	0.991	~
Oswald factor (e) (Takeoff)	0.941	~
Oswald factor (e) (Landing)	0.891	~
C_{L_α}	6.97	rad^{-1}
C_{m_α}	-4.71	rad^{-1}
$C_{L_{\text{max,clean}}}$	1.24	~
$C_{L_{\text{max,takeoff}}}$	2.23	~
$C_{L_{\text{max,landing}}}$	2.63	~

Aircraft Geometry

Table D.4: Propulsion

Number of engines	2	~
SFC_{cruise}	0.513	h^{-1}
Fan diameter	4.04	m
Number of blades	6	~
Diameter	4.04	m
Length	2.17	m

Table D.5: Main Wing dimensions

Span	28.3	m
Planform area	67.51	m^2
MAC	2.54	m
Root Chord	3.43	m
Root t/c	0.21	~
Tip Chord	1.35	m
Tip t/c	0.15	~
Sections (root to tip)	NACA64421 NACA64421 NACA64421	
Sweep 0.25c	-0.0709	°
Taper ratio	0.392	~
Twist	0	°
Dihedral	1.2	°

Table D.6: Horizontal Stabilizer dimensions

Span	11.9	m
Planform area	23.43	m^2
MAC	2.1	m
Root Chord	2.82	m
Root t/c	0.1	~
Tip Chord	1.13	m
Tip t/c	0.1	~
Sections (root to tip)	N0012 N0012	
Sweep 0.25c	0.206	°
Taper ratio	0.4	~
Twist	0	°
Dihedral	1.2	°

Table D.7: Vertical Stabilizer dimensions

Span	3.78	m
Planform area	9.211	m^2
MAC	2.49	m
Root Chord	3.05	m
Root t/c	0.12	~
Tip Chord	1.83	m
Tip t/c	0.12	~
Sections (root to tip)	N0012 N0012	
Sweep 0.25c	9.73	°
Taper ratio	0.6	~
Twist	0	°
Dihedral	0	°

Table D.8: Fuselage dimensions

Length	25.4	m
Diameter	2.74	m
Nose Shape Factor	0.15	~
Tail Shape Factor	0.25	~
Nose Length	3.8	m
Tail Length	6.85	~
Aft Ratio Width	0.05	~
Aft Ratio Height	0.05	~

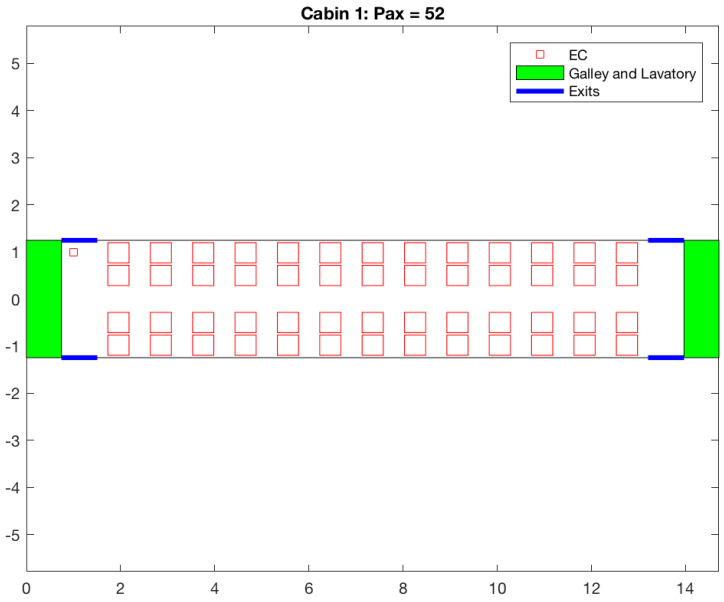

DC-9 Mod.1(I) Report

The aircraft is a conventional aircraft with a wing aspect ratio of 9.8. The aircraft is designed to transport 155 passengers with a total payload mass of 16275kg over 2740km.

Specification

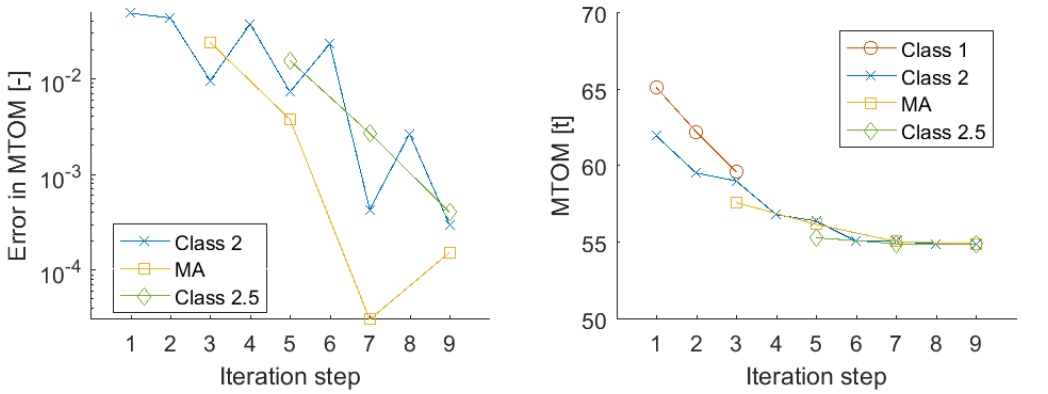

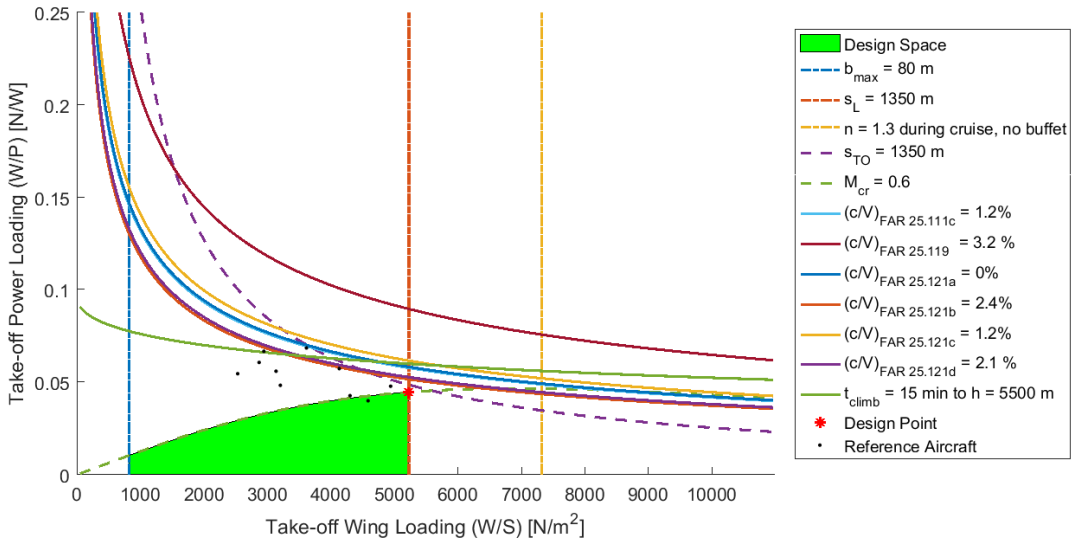

Pax	155	~
Payload Mass	16275	kg
Cruise Mach	0.6	~
Altitude	8500	m
Range	2740	km
Take Off Distance	1350	m
Landing Distance	1350	m
Cargo Mass	3875	kg
Wing loading (MTOM)	5233	N/m^2
Power Loading	0.0446	~

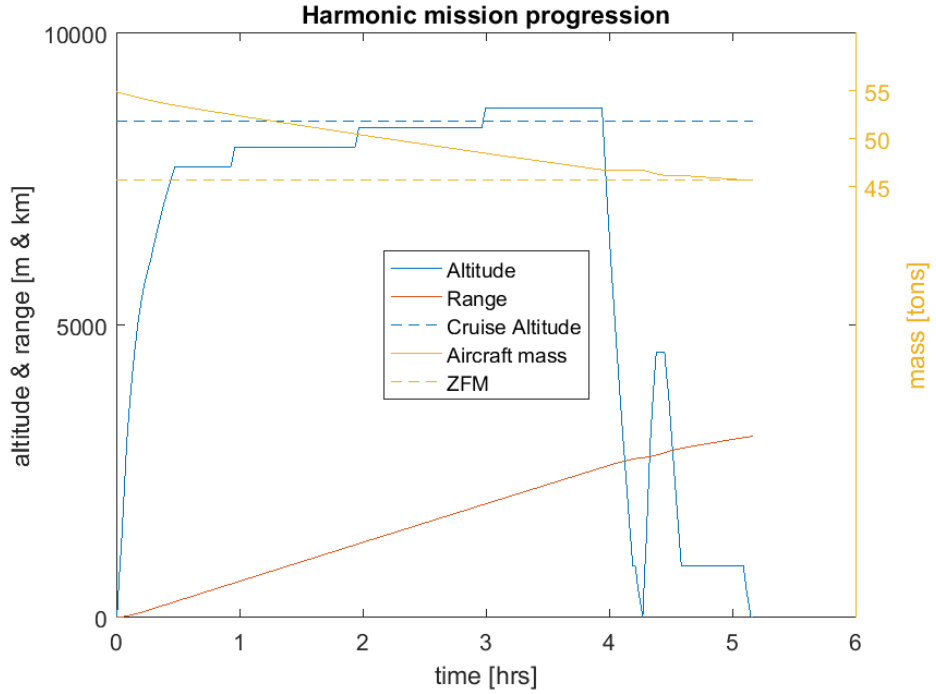

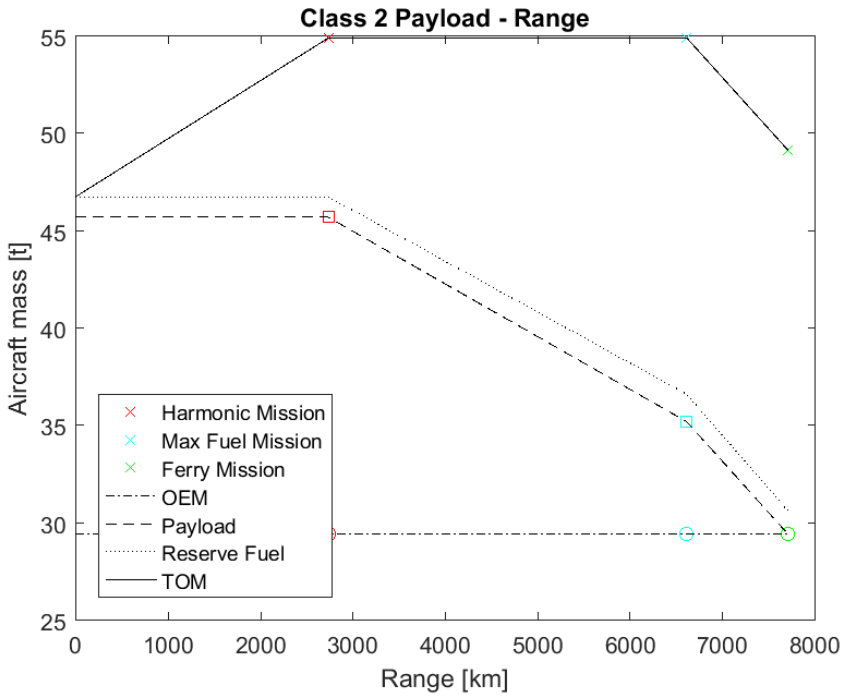

Weight Estimation

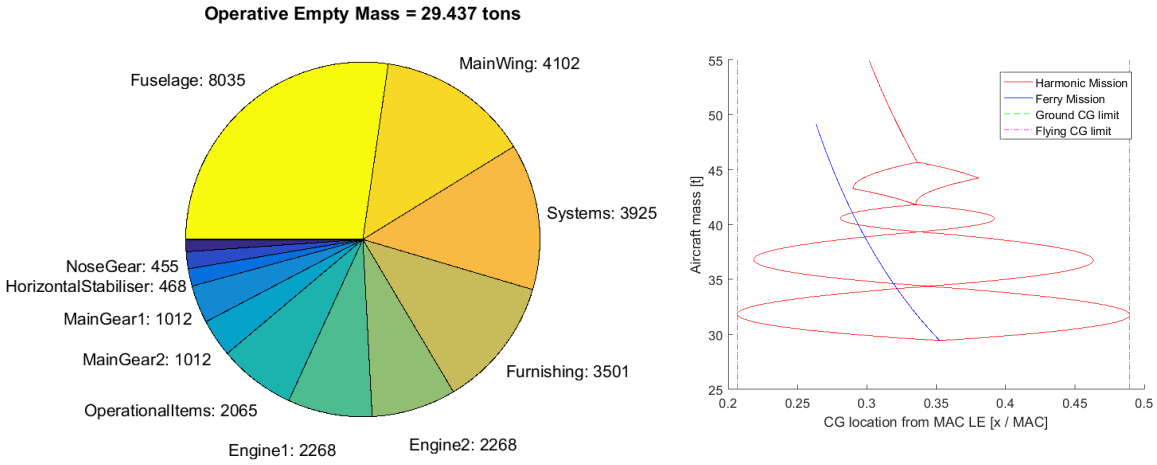

Table E.1: Mass Summary

Maximum take-off mass	54930	kg
Operational empty mass	29437	kg
Design landing mass	46760	kg
Maximum landing mass	47550	kg
Maximum ramp mass	56040	kg
Maximum fuel mass (ferry)	20000	kg
Payload mass	16280	kg
Total fuel mass	9200	kg
Payload mass	16275	kg
Total fuel mass	9200	kg
Reserve fuel mass	1300	kg

Table E.2: Centre-of-gravity locations

X_{cg} (MTOM)	21.1	m
X_{cg} (OEM)	21.3	m
X_{cg} (ZFM)	21.3	m
X_{np}	23.7	m

Aerodynamics

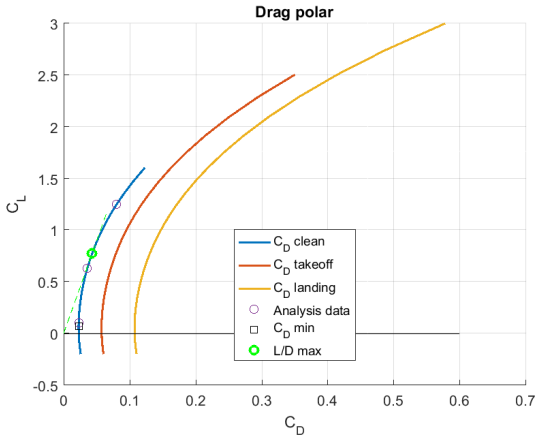

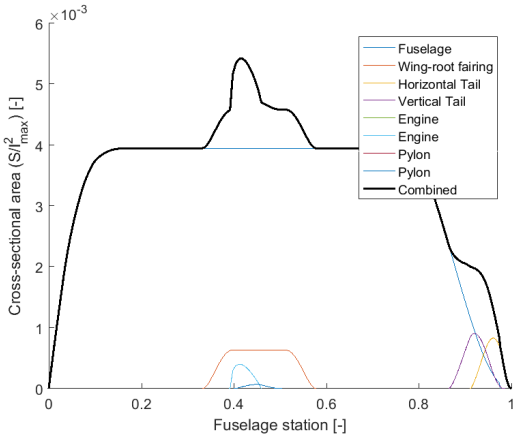

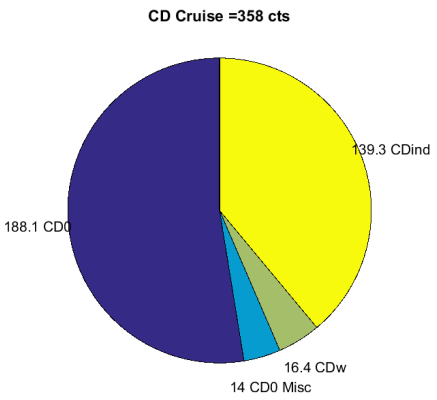

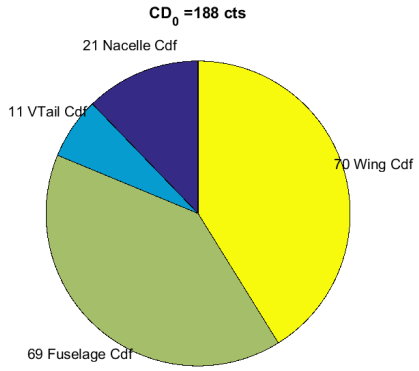

Table E.3: Aerodynamic Properties

$C_{L,\text{cruise}}$	0.63	~
$C_{D,\text{cruise}}$	365	cts
L/D_{cruise}	17.2	~
C_{D_0} (Clean)	229	cts
C_{D_0} (Take-Off)	576	cts
C_{D_0} (Landing)	1076	cts
Oswald factor (e) (Clean)	0.925	~
Oswald factor (e) (Take-Off)	0.875	~
Oswald factor (e) (Landing)	0.825	~
C_{L_α}	6.27	rad^{-1}
C_{m_α}	-4.50	rad^{-1}
$C_{L_{\text{max,clean}}}$	1.67	~
$C_{L_{\text{max,take-off}}}$	2.6	~
$C_{L_{\text{max,landing}}}$	3.2	~

Aircraft Geometry

Table E.4: Propulsion

Number of engines	2	~
SFC_{cruise}	0.5	h^{-1}
Fan diameter	3.37	m
Number of blades	8	~
Diameter	3.37	m
Length	3.27	m

Table E.5: Main Wing dimensions

Span	31.8	m
Planform area	100.1	m^2
MAC	3.41	m
Root Chord	4.72	m
Root t/c	0.18	~
Tip Chord	1.57	m
Tip t/c	0.16	~
Sections (root to tip)	N663418 N663418 N662415	
Sweep 0.25c	22.6	°
Taper ratio	0.333	~
Twist	0	°
Dihedral	5.5	°

Table E.6: Horizontal Stabilizer dimensions

Span	10.6	m
Planform area	22.59	m^2
MAC	2.29	m
Root Chord	3.15	m
Root t/c	0.1	~
Tip Chord	1.1	m
Tip t/c	0.1	~
Sections (root to tip)	N0012 N0012	
Sweep 0.25c	23.5	°
Taper ratio	0.35	~
Twist	0	°
Dihedral	5.5	°

Table E.7: Vertical Stabilizer dimensions

Span	4.45	m
Planform area	16.47	m^2
MAC	3.72	m
Root Chord	4.12	m
Root t/c	0.12	~
Tip Chord	3.29	m
Tip t/c	0.12	~
Sections (root to tip)	N0012 N0012	
Sweep 0.25c	22.8	°
Taper ratio	0.8	~
Twist	0	°
Dihedral	0	°

Table E.8: Fuselage dimensions

Length	43.7	m
Diameter	3.18	m
Nose Shape Factor	0.15	~
Tail Shape Factor	0.2	~
Nose Length	4.8	m
Tail Length	6.55	~
Aft Ratio Width	0.14	~
Aft Ratio Height	0.14	~

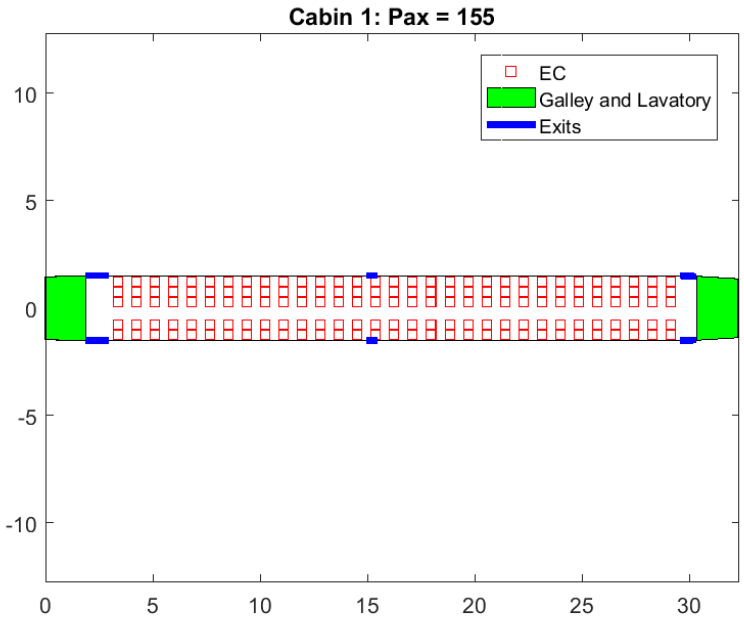

DC-9 Mod.2(I) Report

The aircraft is a conventional aircraft with a wing aspect ratio of 9.8. The aircraft is designed to transport 155 passengers with a total payload mass of 16275kg over 2295km.

Specification

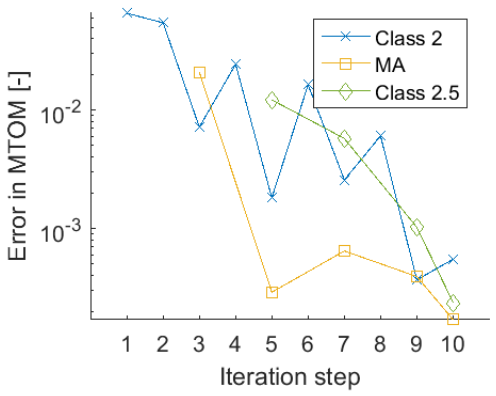

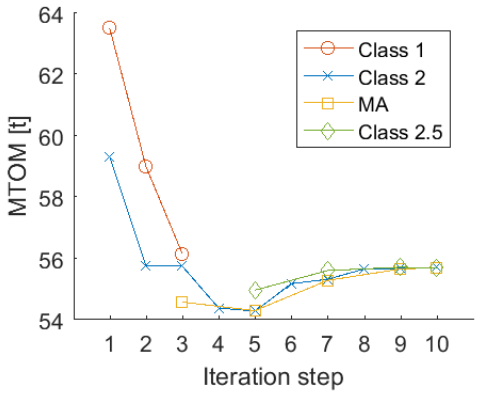

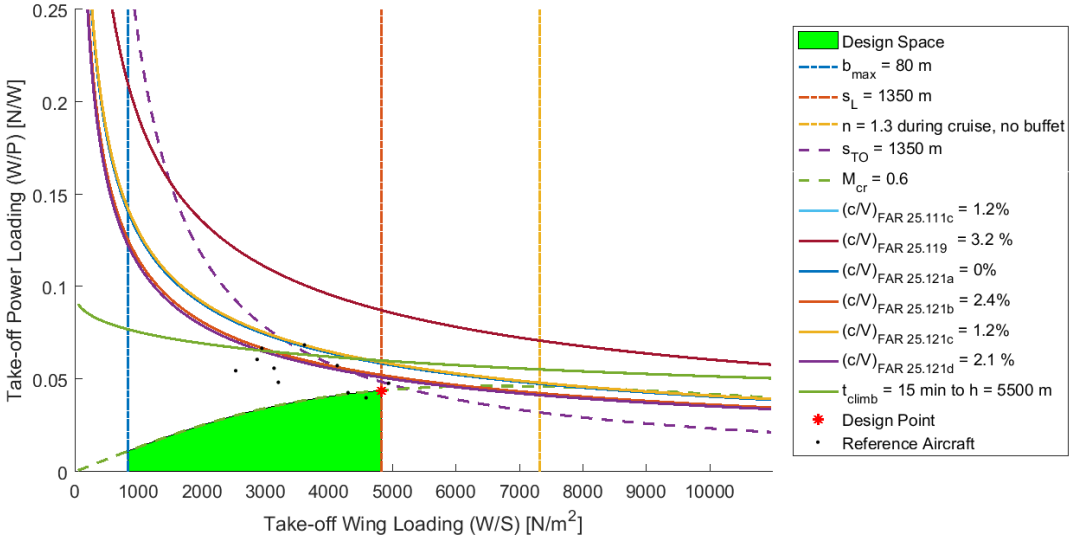

Pax	155	~
Payload Mass	16275	kg
Cruise Mach	0.6	~
Altitude	8500	m
Range	2295	km
Take Off Distance	1350	m
Landing Distance	1350	m
Cargo Mass	3875	kg
Wing loading (MTOM)	4826	N/m^2
Power Loading	0.0439	~

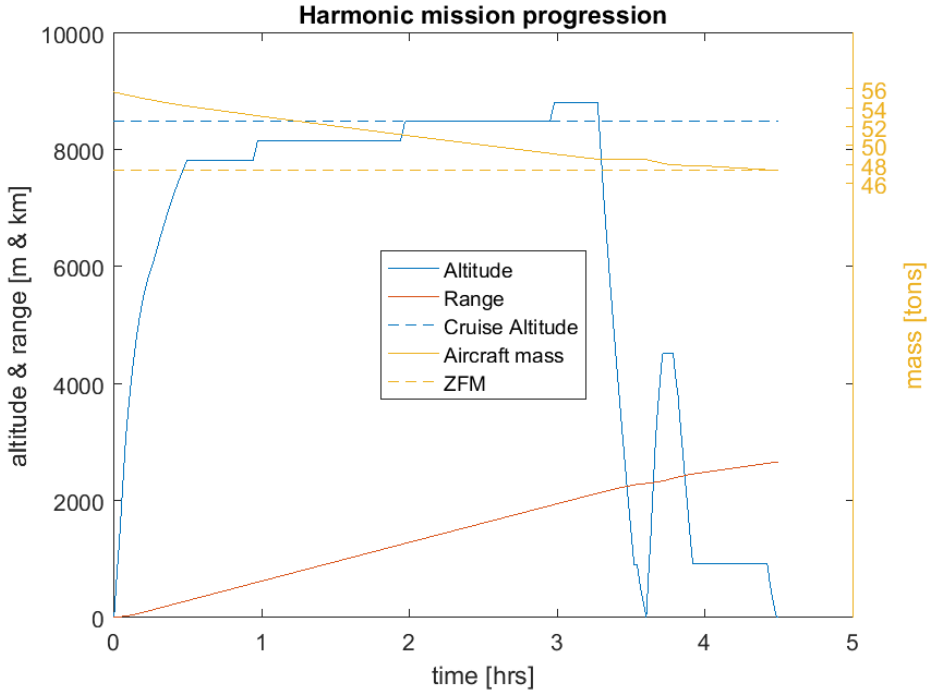

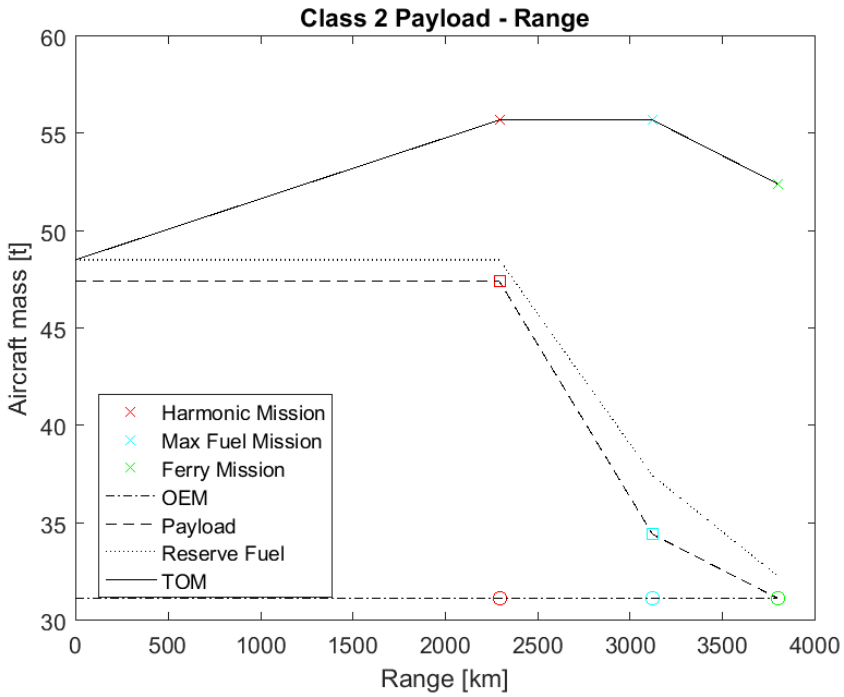

Weight Estimation

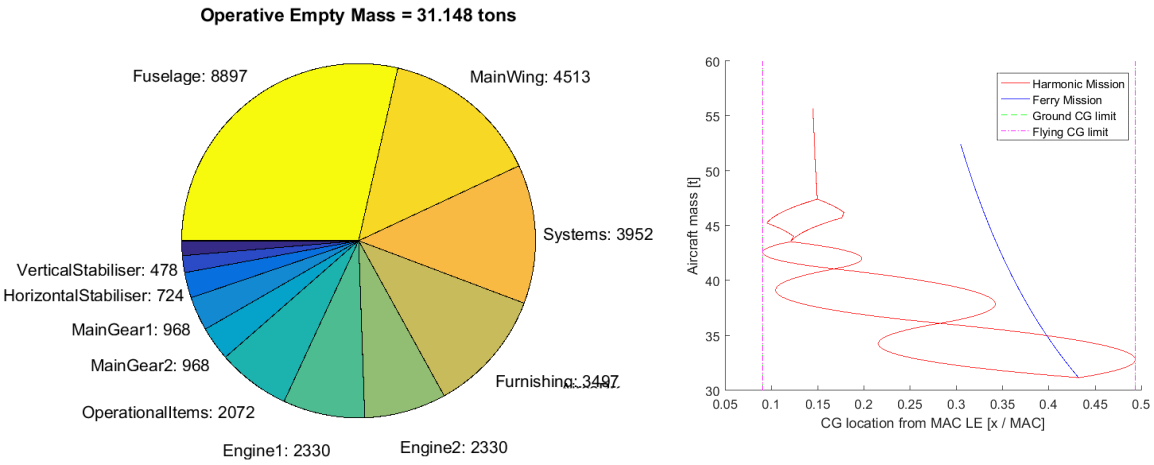

Table F.1: Mass Summary

Maximum take-off mass	55710	kg
Operational empty mass	31148	kg
Design landing mass	48530	kg
Maximum landing mass	49080	kg
Maximum ramp mass	56840	kg
Maximum fuel mass (ferry)	21000	kg
Payload mass	16280	kg
Total fuel mass	8300	kg
Payload mass	16275	kg
Total fuel mass	8300	kg
Reserve fuel mass	1300	kg

Table F.2: Centre-of-gravity locations

X_{cg} (MTOM)	24.2	m
X_{cg} (OEM)	25.3	m
X_{cg} (ZFM)	25.3	m
X_{np}	27.5	m

Aerodynamics

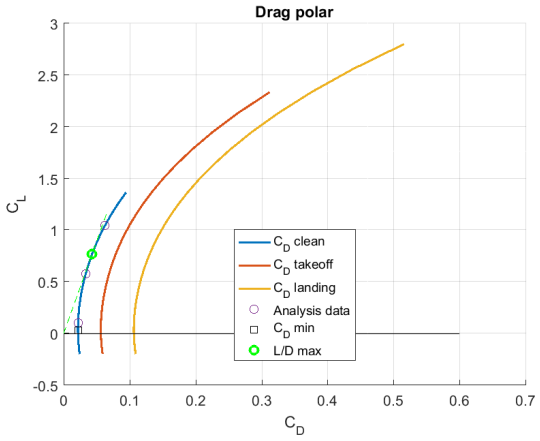

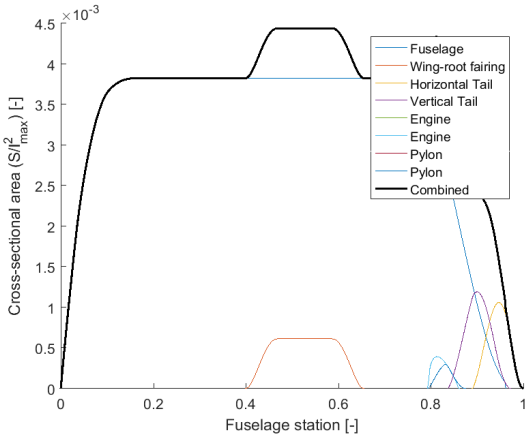

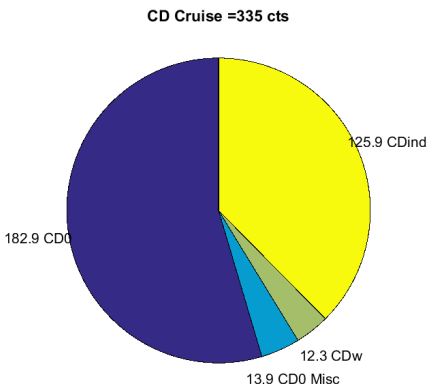

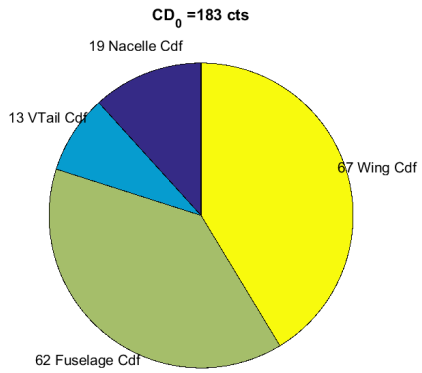

Table F.3: Aerodynamic Properties

$C_{L,\text{cruise}}$	0.58	~
$C_{D,\text{cruise}}$	342	cts
L/D_{cruise}	16.9	~
C_{D_0} (Clean)	218	cts
C_{D_0} (Take~Off)	564	cts
C_{D_0} (Landing)	1064	cts
Oswald factor (e) (Clean)	0.889	~
Oswald factor (e) (Take~Off)	0.84	~
Oswald factor (e) (Landing)	0.789	~
C_{L_α}	6.52	rad^{-1}
C_{m_α}	~5.65	rad^{-1}
$C_{L_{\text{max,clean}}}$	1.39	~
$C_{L_{\text{max,take~off}}}$	2.4	~
$C_{L_{\text{max,landing}}}$	3	~

Aircraft Geometry

Table F.4: Propulsion

Number of engines	2	~
SFC_{cruise}	0.5	h^{-1}
Fan diameter	3.37	m
Number of blades	8	~
Diameter	3.37	m
Length	3.31	m

Table F.5: Main Wing dimensions

Span	33.3	m
Planform area	110.2	m^2
MAC	3.58	m
Root Chord	4.96	m
Root t/c	0.18	~
Tip Chord	1.65	m
Tip t/c	0.13	~
Sections (root to tip)	N663418 N663418 N662415	
Sweep 0.25c	22.6	°
Taper ratio	0.332	~
Twist	0	°
Dihedral	5.5	°

Table F.6: Horizontal Stabilizer dimensions

Span	12.7	m
Planform area	31.78	m^2
MAC	2.62	m
Root Chord	3.44	m
Root t/c	0.1	~
Tip Chord	1.55	m
Tip t/c	0.1	~
Sections (root to tip)	N0012 N0012	
Sweep 0.25c	24.6	°
Taper ratio	0.45	~
Twist	0	°
Dihedral	5.5	°

Table F.7: Vertical Stabilizer dimensions

Span	5.19	m
Planform area	22.42	m^2
MAC	4.34	m
Root Chord	4.8	m
Root t/c	0.12	~
Tip Chord	3.84	m
Tip t/c	0.12	~
Sections (root to tip)	N0012 N0012	
Sweep 0.25c	22.8	°
Taper ratio	0.8	~
Twist	0	°
Dihedral	0	°

Table F.8: Fuselage dimensions

Length	43.7	m
Diameter	3.18	m
Nose Shape Factor	0.15	~
Tail Shape Factor	0.2	~
Nose Length	4.8	m
Tail Length	6.55	~
Aft Ratio Width	0.14	~
Aft Ratio Height	0.14	~

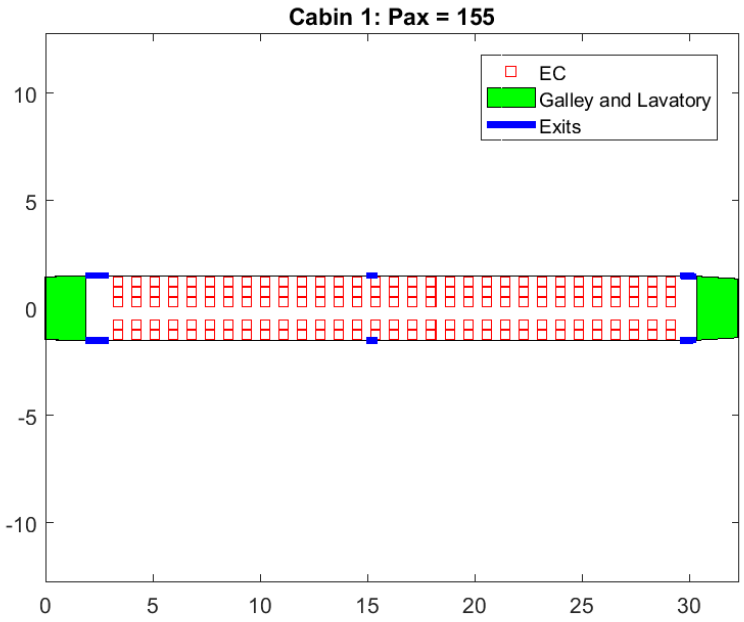

G

DC-9 Mod.3(I) Report

The aircraft is a conventional aircraft with a wing aspect ratio of 9.8. The aircraft is designed to transport 155 passengers with a total payload mass of 16275kg over 2869km.

Specification

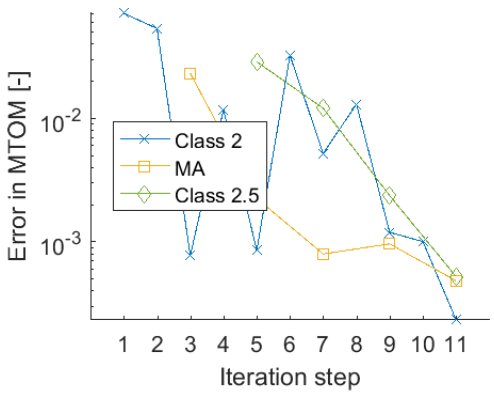

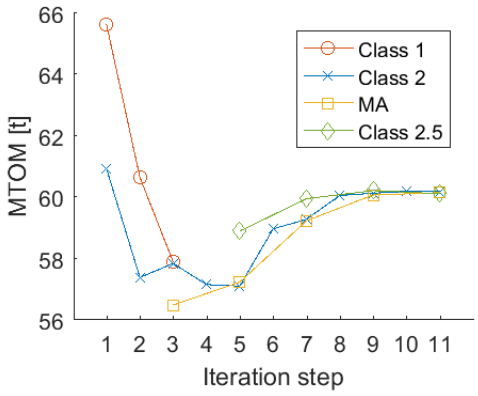

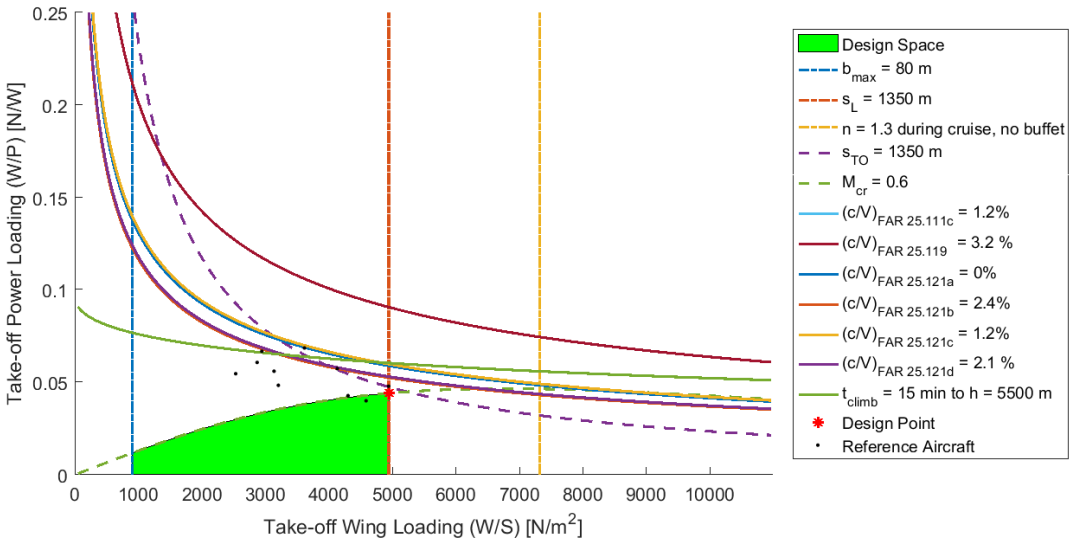

Pax	155	~
Payload Mass	16275	kg
Cruise Mach	0.6	~
Altitude	8500	m
Range	2869	km
Take Off Distance	1350	m
Landing Distance	1350	m
Cargo Mass	3875	kg
Wing loading (MTOM)	4948	N/m^2
Power Loading	0.0441	~

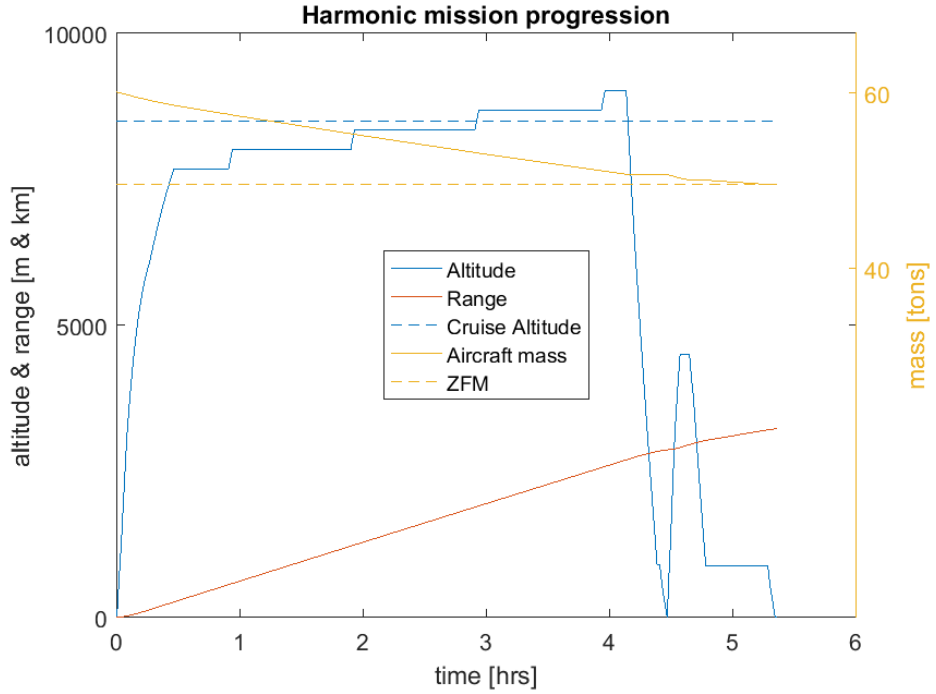

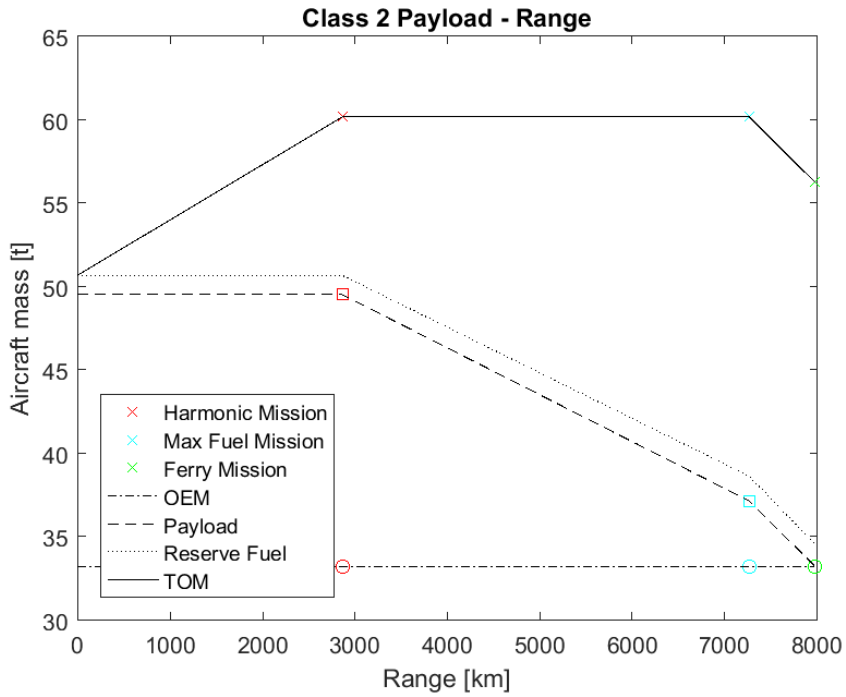

Weight Estimation

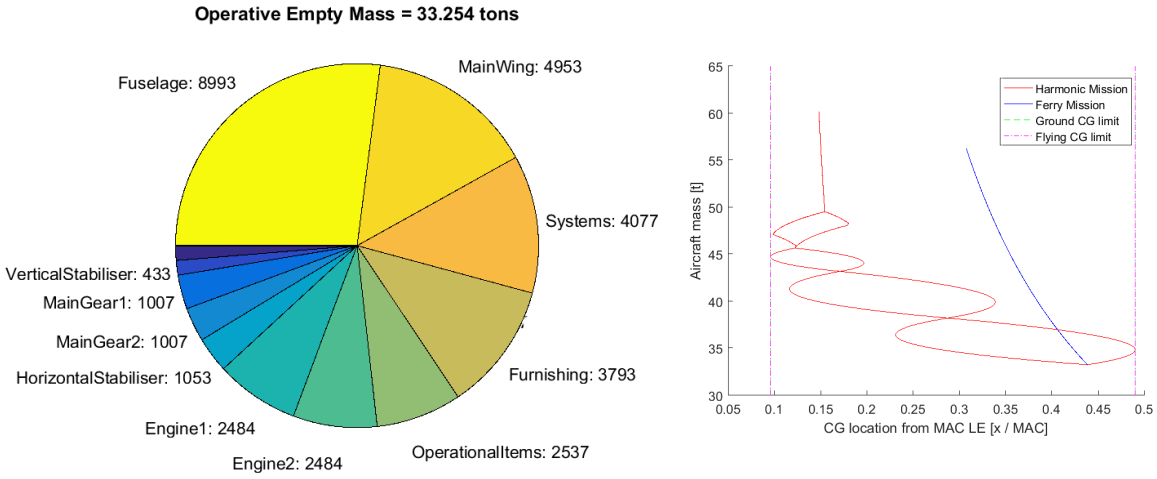

Table G.1: Mass Summary

Maximum take-off mass	60180	kg
Operational empty mass	33254	kg
Design landing mass	50680	kg
Maximum landing mass	51660	kg
Maximum ramp mass	61400	kg
Maximum fuel mass (ferry)	23000	kg
Payload mass	16280	kg
Total fuel mass	11000	kg
Payload mass	16275	kg
Total fuel mass	11000	kg
Reserve fuel mass	1400	kg

Table G.2: Centre-of-gravity locations

X_{cg} (MTOM)	24.5	m
X_{cg} (OEM)	25.7	m
X_{cg} (ZFM)	25.7	m
X_{np}	27.4	m

Aerodynamics

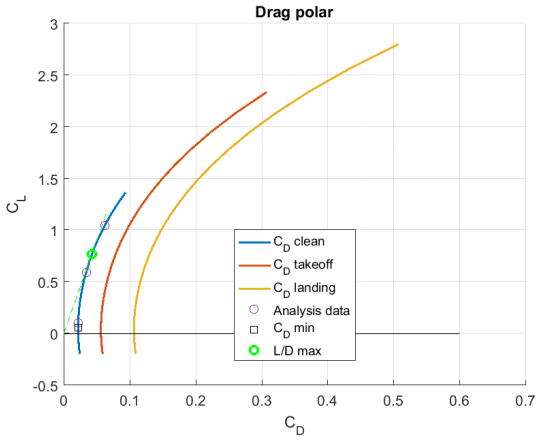

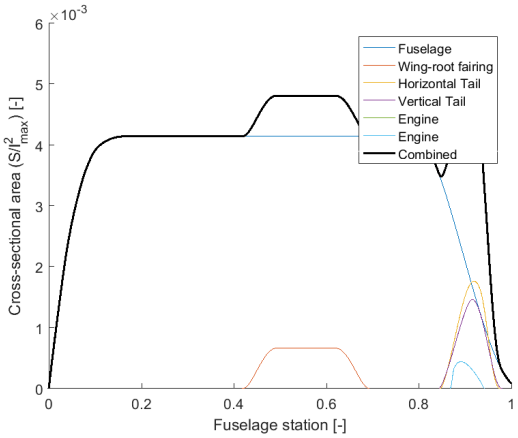

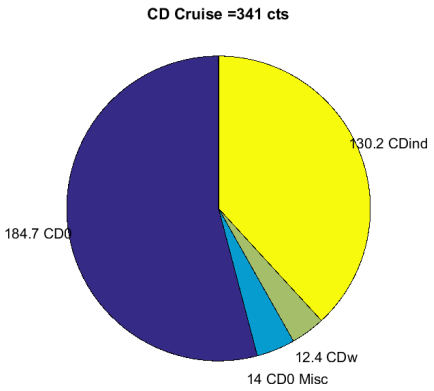

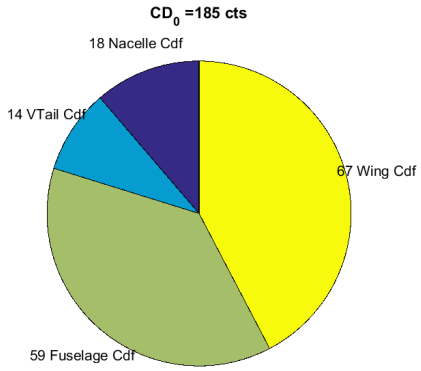

Table G.3: Aerodynamic Properties

$C_{L,\text{cruise}}$	0.59	~
$C_{D,\text{cruise}}$	350	cts
L/D_{cruise}	17	~
C_{D_0} (Clean)	220	cts
C_{D_0} (Take-Off)	566	cts
C_{D_0} (Landing)	1066	cts
Oswald factor (e) (Clean)	0.898	~
Oswald factor (e) (Take-Off)	0.848	~
Oswald factor (e) (Landing)	0.798	~
C_{L_α}	6.63	rad^{-1}
C_{m_α}	-4.91	rad^{-1}
$C_{L_{\text{max,clean}}}$	1.39	~
$C_{L_{\text{max,take-off}}}$	2.4	~
$C_{L_{\text{max,landing}}}$	3	~

Aircraft Geometry

Table G.4: Propulsion

Number of engines	2	~
SFC_{cruise}	0.5	h^{-1}
Fan diameter	3.37	m
Number of blades	8	~
Diameter	3.37	m
Length	3.39	m

Table G.5: Main Wing dimensions

Span	34.2	m
Planform area	116.2	m^2
MAC	3.68	m
Root Chord	5.1	m
Root t/c	0.18	~
Tip Chord	1.69	m
Tip t/c	0.13	~
Sections (root to tip)	N663418 N663418 N662415	
Sweep 0.25c	22.6	°
Taper ratio	0.332	~
Twist	0	°
Dihedral	5.5	°

Table G.6: Horizontal Stabilizer dimensions

Span	13.9	m
Planform area	43.23	m^2
MAC	3.29	m
Root Chord	4.43	m
Root t/c	0.1	~
Tip Chord	1.77	m
Tip t/c	0.1	~
Sections (root to tip)	N0012 N0012	
Sweep 0.25c	23.6	°
Taper ratio	0.4	~
Twist	0	°
Dihedral	5.5	°

Table G.7: Vertical Stabilizer dimensions

Span	6.08	m
Planform area	24.65	m^2
MAC	4.37	m
Root Chord	6.01	m
Root t/c	0.12	~
Tip Chord	2.1	m
Tip t/c	0.12	~
Sections (root to tip)	N0012 N0012	
Sweep 0.25c	18.4	°
Taper ratio	0.35	~
Twist	0	°
Dihedral	0	°

Table G.8: Fuselage dimensions

Length	43.7	m
Diameter	3.18	m
Nose Shape Factor	0.15	~
Tail Shape Factor	0.2	~
Nose Length	4.8	m
Tail Length	6.55	~
Aft Ratio Width	0.14	~
Aft Ratio Height	0.14	~

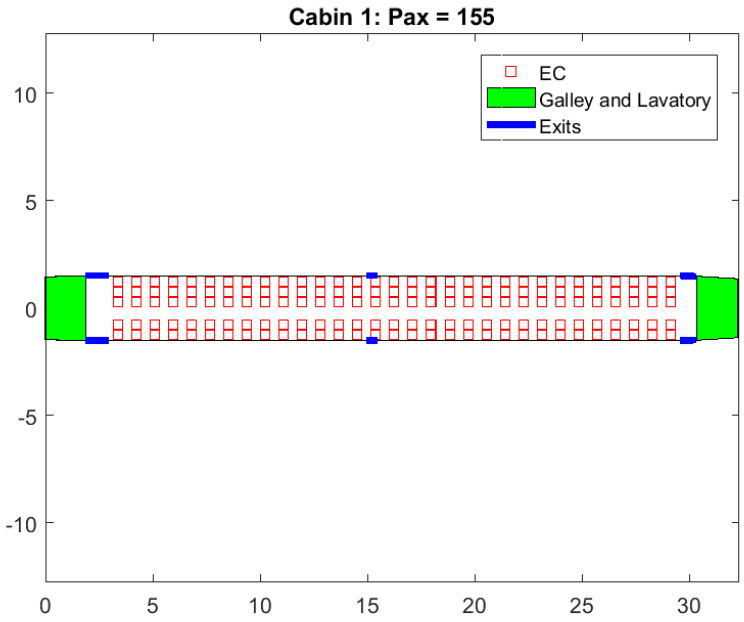

RTP1 Report

The aircraft is a conventional aircraft with a wing aspect ratio of 11. The aircraft is designed to transport 130 passengers with a total payload mass of 13650kg over 2955km.

Specification

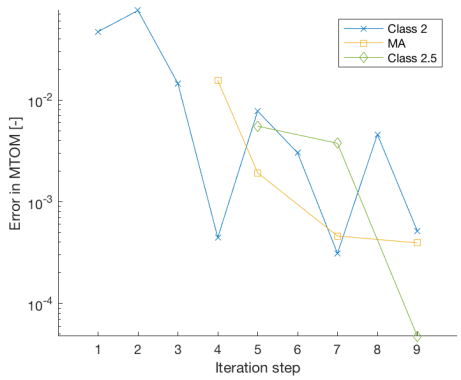

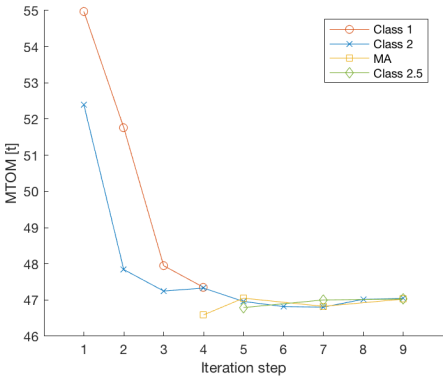

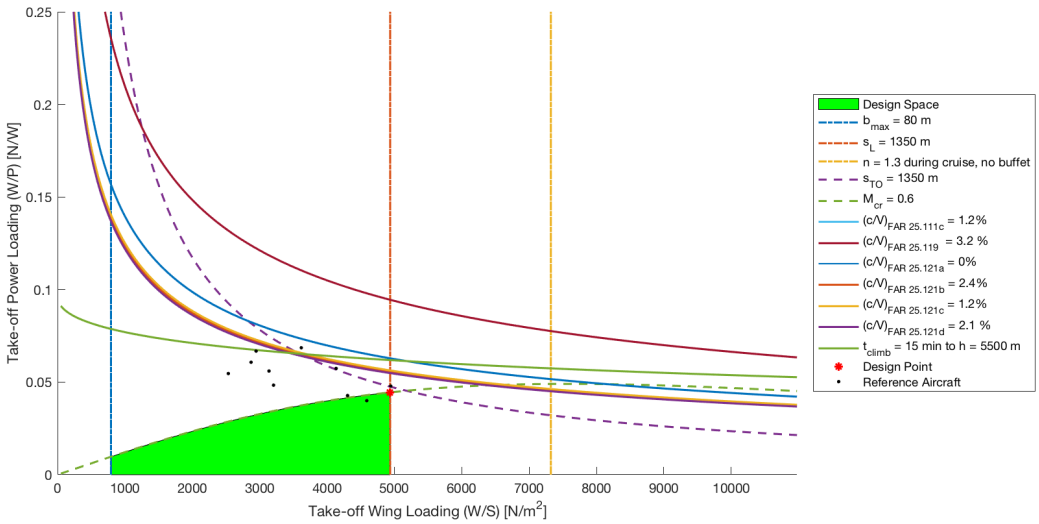

Pax	130	~
Payload Mass	13650	kg
Cruise Mach	0.6	~
Altitude	8500	m
Range	2955	km
Take Off Distance	1350	m
Landing Distance	1350	m
Cargo Mass	3250	kg
Wing loading (MTOM)	4937	N/m^2
Power Loading	0.0444	~

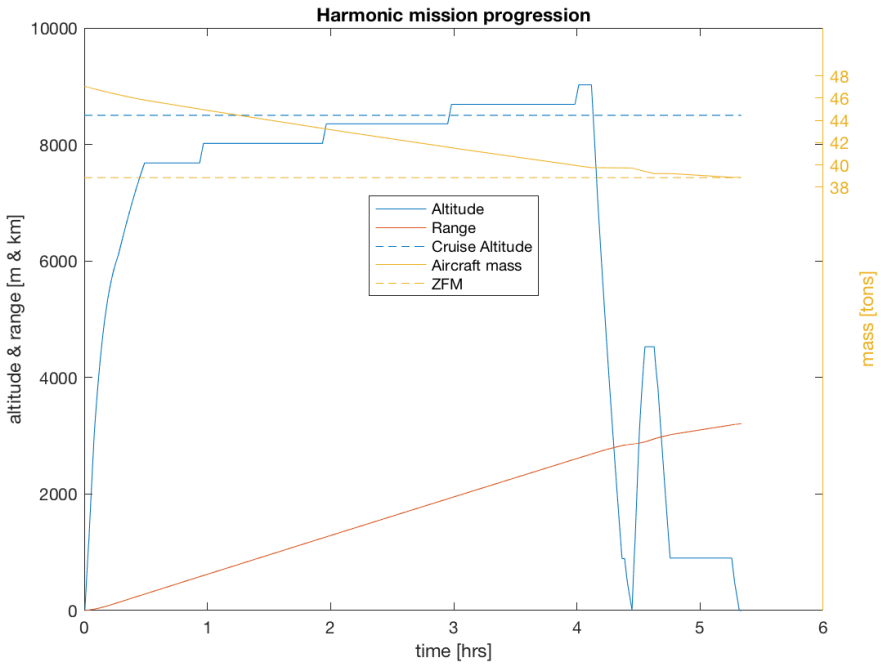

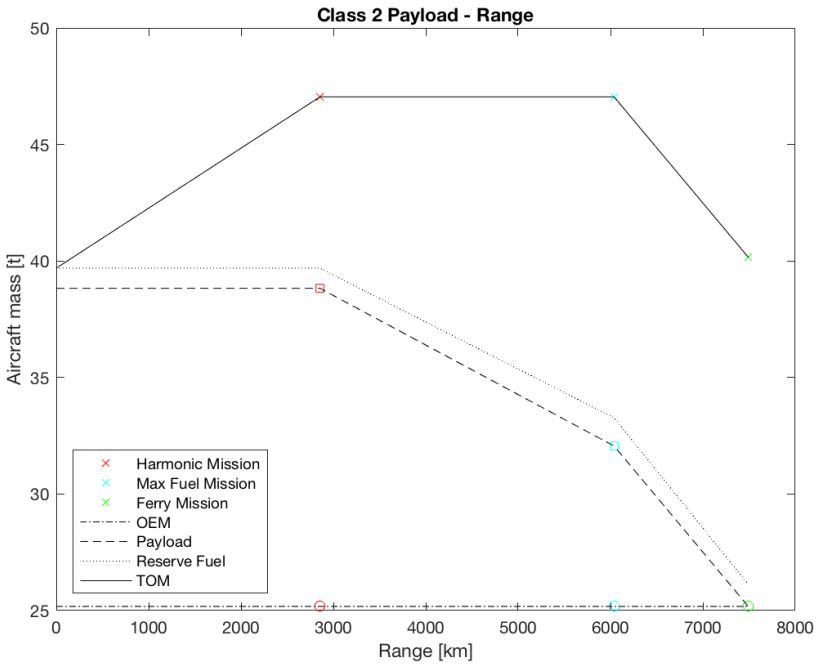

Weight Estimation

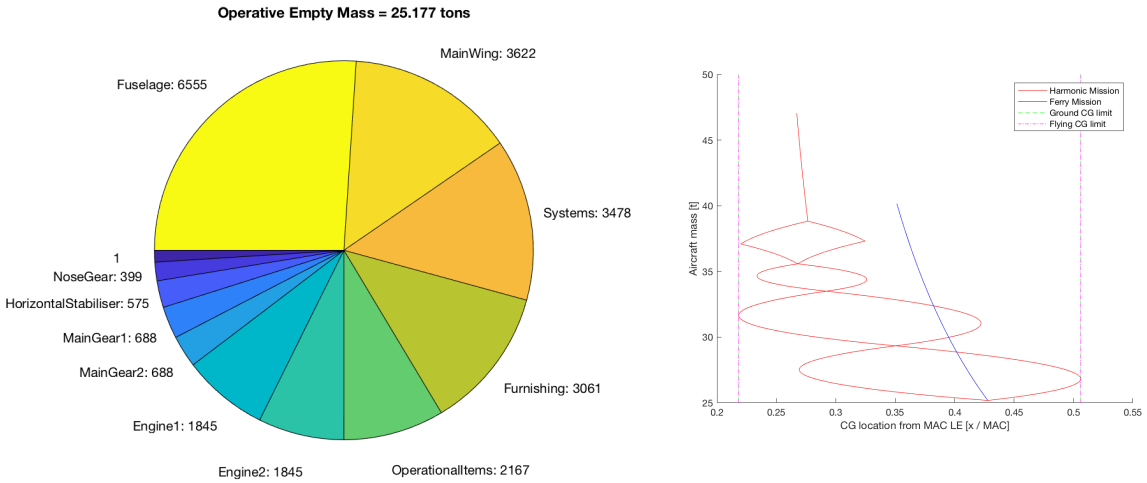

Table H.1: Mass Summary

Maximum take-off mass	47040	kg
Operational empty mass	25177	kg
Design landing mass	39690	kg
Maximum landing mass	40470	kg
Maximum ramp mass	48000	kg
Maximum fuel mass (ferry)	15000	kg
Payload mass	13650	kg
Total fuel mass	8200	kg
Payload mass	13650	kg
Total fuel mass	8200	kg
Reserve fuel mass	1000	kg

Table H.2: Centre-of-gravity locations

X_{cg} (MTOM)	16.9	m
X_{cg} (OEM)	17.4	m
X_{cg} (ZFM)	17.4	m
X_{np}	19.6	m

Aerodynamics

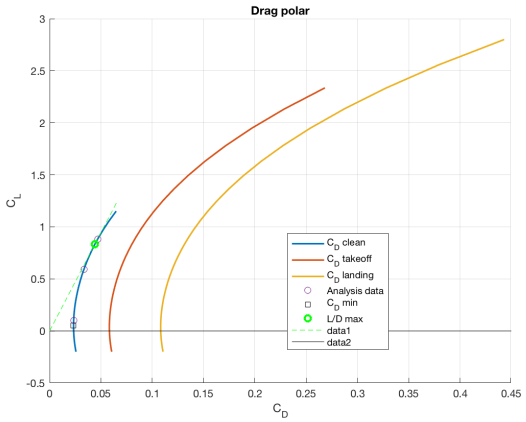

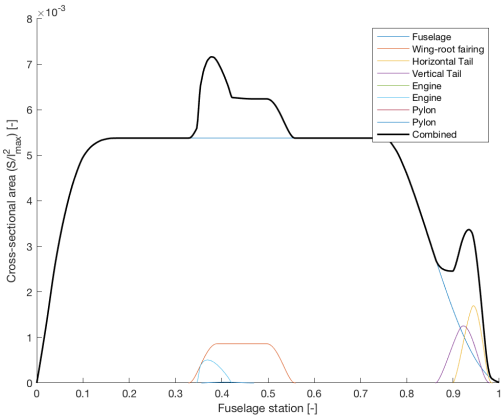

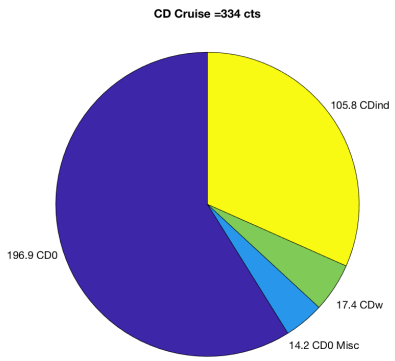

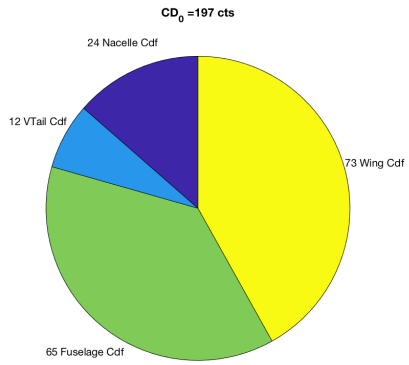

Table H.3: Aerodynamic Properties

$C_{L,\text{cruise}}$	0.59	~
$C_{D,\text{cruise}}$	346	cts
L/D_{cruise}	17.1	~
C_{D_0} (Clean)	234	cts
C_{D_0} (Take-Off)	583	cts
C_{D_0} (Landing)	1083	cts
Oswald factor (e) (Clean)	0.964	~
Oswald factor (e) (Take-Off)	0.914	~
Oswald factor (e) (Landing)	0.864	~
C_{L_α}	7.03	rad^{-1}
C_{m_α}	-5.97	rad^{-1}
$C_{L_{\text{max,clean}}}$	1.18	~
$C_{L_{\text{max,take-off}}}$	2.4	~
$C_{L_{\text{max,landing}}}$	3	~

Aircraft Geometry

Table H.4: Propulsion

Number of engines	2	~
SFC_{cruise}	0.5	h^{-1}
Fan diameter	3.37	m
Number of blades	10	~
Diameter	3.37	m
Length	3.1	m

Table H.5: Main Wing dimensions

Span	32.1	m
Planform area	92.88	m^2
MAC	3.1	m
Root Chord	4.24	m
Root t/c	0.18	~
Tip Chord	1.56	m
Tip t/c	0.16	~
Sections (root to tip)	N663418 N663418 N662415	
Sweep 0.25c	10.2	°
Taper ratio	0.367	~
Twist	0	°
Dihedral	5.5	°

Table H.6: Horizontal Stabilizer dimensions

Span	12.8	m
Planform area	27.21	m^2
MAC	2.17	m
Root Chord	2.66	m
Root t/c	0.1	~
Tip Chord	1.6	m
Tip t/c	0.1	~
Sections (root to tip)	N0012 N0012	
Sweep 0.25c	11.7	°
Taper ratio	0.6	~
Twist	0	°
Dihedral	5.5	°

Table H.7: Vertical Stabilizer dimensions

Span	5.06	m
Planform area	16.03	m^2
MAC	3.36	m
Root Chord	4.52	m
Root t/c	0.12	~
Tip Chord	1.81	m
Tip t/c	0.12	~
Sections (root to tip)	N0012 N0012	
Sweep 0.25c	15.3	°
Taper ratio	0.4	~
Twist	0	°
Dihedral	0	°

Table H.8: Fuselage dimensions

Length	38.3	m
Diameter	3.18	m
Nose Shape Factor	0.15	~
Tail Shape Factor	0.25	~
Nose Length	3.45	m
Tail Length	10.7	~
Aft Ratio Width	0.05	~
Aft Ratio Height	0.05	~

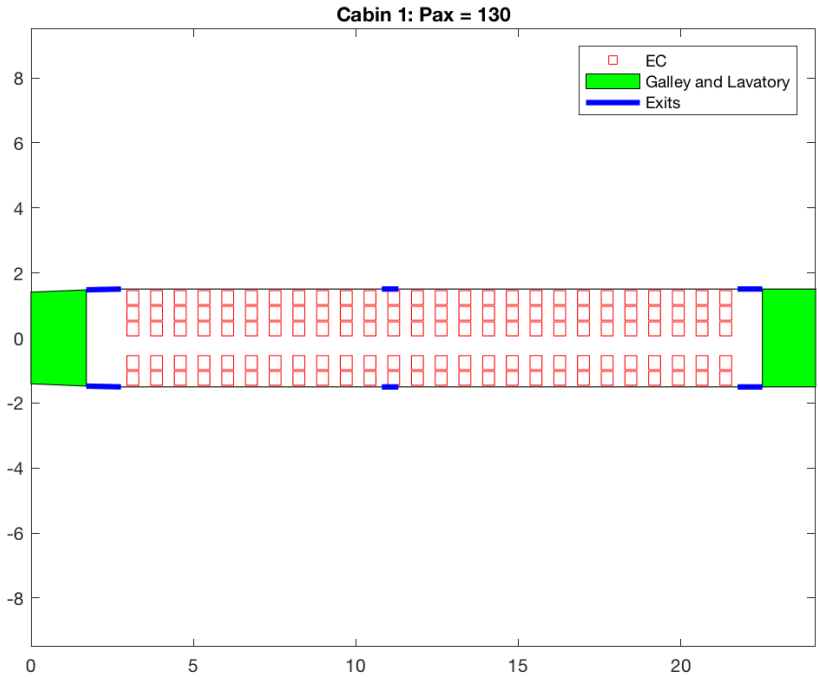

The aircraft is a conventional aircraft with a wing aspect ratio of 11. The aircraft is designed to transport 130 passengers with a total payload mass of 13650kg over 2955km.

Specification

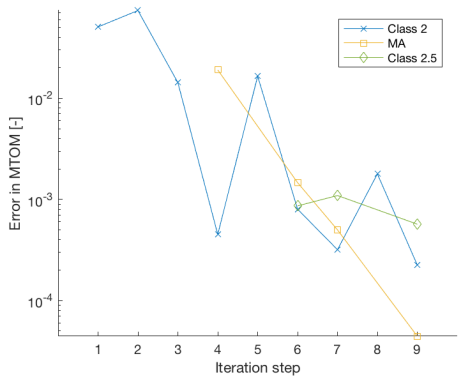

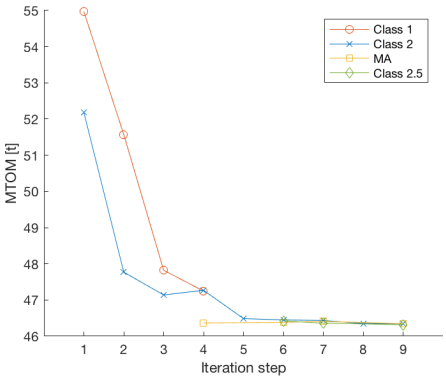

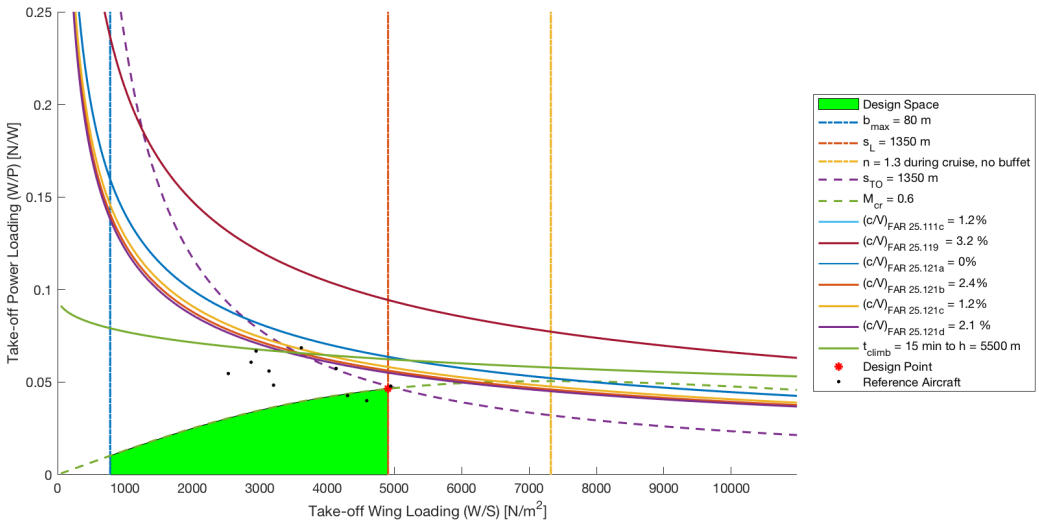

Pax	130	~
Payload Mass	13650	kg
Cruise Mach	0.6	~
Altitude	8500	m
Range	2955	km
Take Off Distance	1350	m
Landing Distance	1350	m
Cargo Mass	3250	kg
Wing loading (MTOM)	4906	N/m^2
Power Loading	0.0464	~

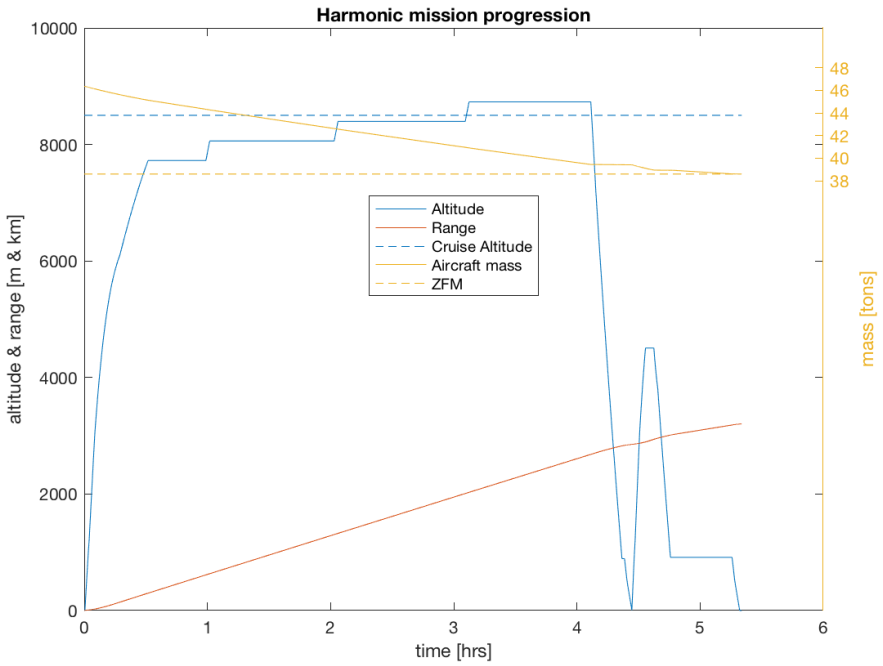

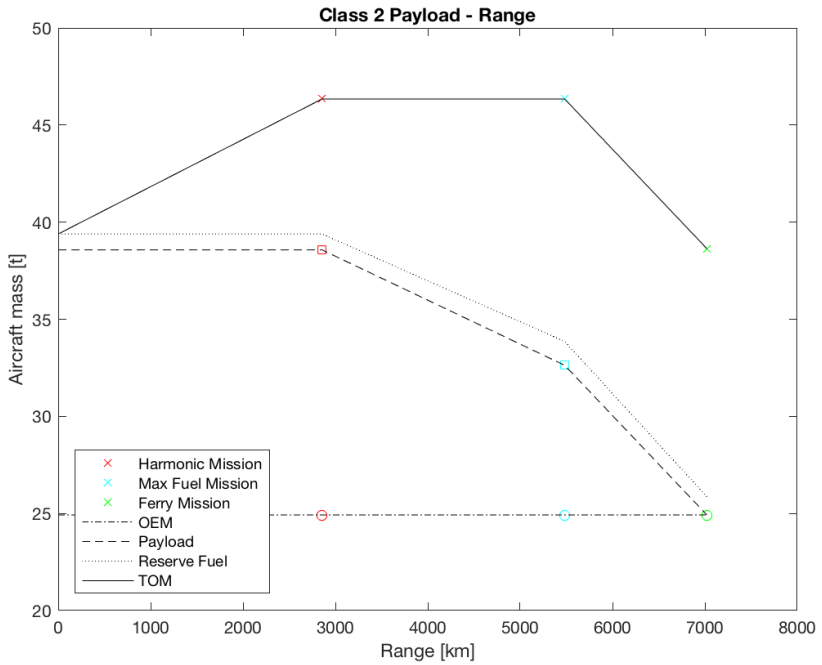

Weight Estimation

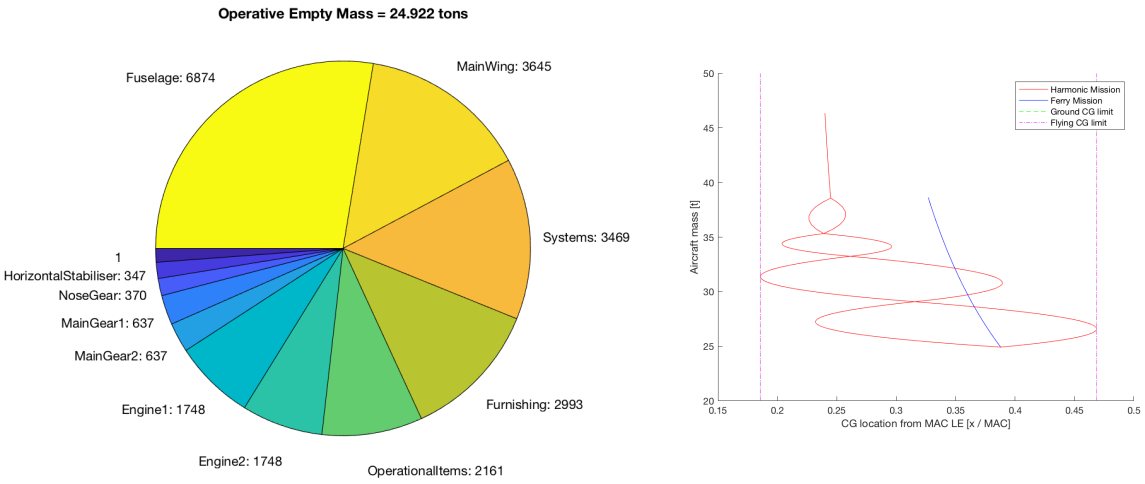

Table I.1: Mass Summary

Maximum take-off mass	46340	kg
Operational empty mass	24922	kg
Design landing mass	39390	kg
Maximum landing mass	40130	kg
Maximum ramp mass	47280	kg
Maximum fuel mass (ferry)	14000	kg
Payload mass	13650	kg
Total fuel mass	7800	kg
Payload mass	13650	kg
Total fuel mass	7800	kg
Reserve fuel mass	990	kg

Table I.2: Centre-of-gravity locations

X_{cg} (MTOM)	16.7	m
X_{cg} (OEM)	17.2	m
X_{cg} (ZFM)	17.2	m
X_{np}	18.8	m

Aerodynamics

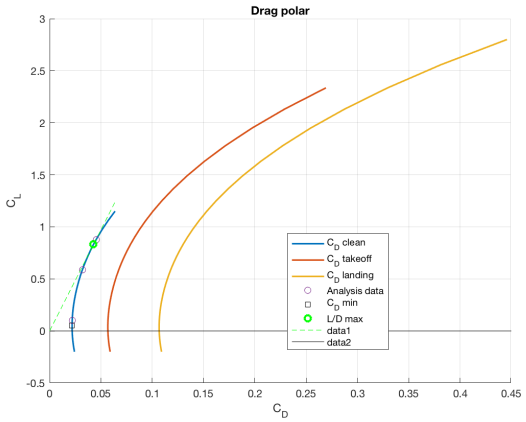

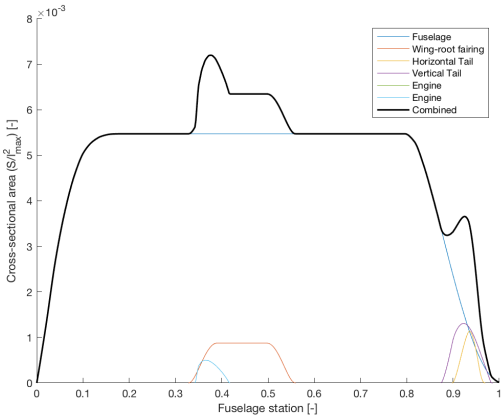

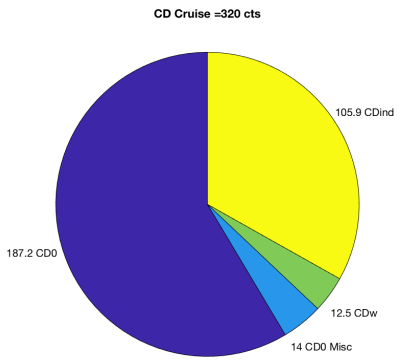

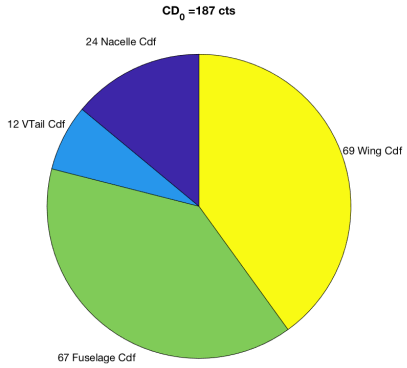

Table I.3: Aerodynamic Properties

$C_{L,\text{cruise}}$	0.59	~
$C_{D,\text{cruise}}$	329	cts
L/D_{cruise}	17.9	~
C_{D_0} (Clean)	220	cts
C_{D_0} (Take-Off)	568	cts
C_{D_0} (Landing)	1068	cts
Oswald factor (e) (Clean)	0.956	~
Oswald factor (e) (Take-Off)	0.906	~
Oswald factor (e) (Landing)	0.856	~
C_{L_α}	6.70	rad^{-1}
C_{m_α}	-4.53	rad^{-1}
$C_{L_{\text{max,clean}}}$	1.17	~
$C_{L_{\text{max,take-off}}}$	2.4	~
$C_{L_{\text{max,landing}}}$	3	~

Aircraft Geometry

Table I.4: Propulsion

Number of engines	2	~
SFC_{cruise}	0.5	h^{-1}
Fan diameter	3.37	m
Number of blades	10	~
Diameter	3.37	m
Length	3.04	m

Table I.5: Main Wing dimensions

Span	31.9	m
Planform area	92.16	m^2
MAC	3.09	m
Root Chord	4.22	m
Root t/c	0.18	~
Tip Chord	1.55	m
Tip t/c	0.13	~
Sections (root to tip)	N663418 N663418 N662415	
Sweep 0.25c	10.2	°
Taper ratio	0.367	~
Twist	0	°
Dihedral	1.3	°

Table I.6: Horizontal Stabilizer dimensions

Span	10.4	m
Planform area	17.98	m^2
MAC	1.77	m
Root Chord	2.16	m
Root t/c	0.1	~
Tip Chord	1.3	m
Tip t/c	0.1	~
Sections (root to tip)	N0012 N0012	
Sweep 0.25c	11.7	°
Taper ratio	0.6	~
Twist	0	°
Dihedral	1.2	°

Table I.7: Vertical Stabilizer dimensions

Span	4.38	m
Planform area	15.98	m^2
MAC	3.66	m
Root Chord	4.05	m
Root t/c	0.12	~
Tip Chord	3.24	m
Tip t/c	0.12	~
Sections (root to tip)	N0012 N0012	
Sweep 0.25c	9.95	°
Taper ratio	0.8	~
Twist	0	°
Dihedral	0	°

Table I.8: Fuselage dimensions

Length	38	m
Diameter	3.18	m
Nose Shape Factor	0.15	~
Tail Shape Factor	0.2	~
Nose Length	3.42	m
Tail Length	10.6	~
Aft Ratio Width	0.05	~
Aft Ratio Height	0.05	~

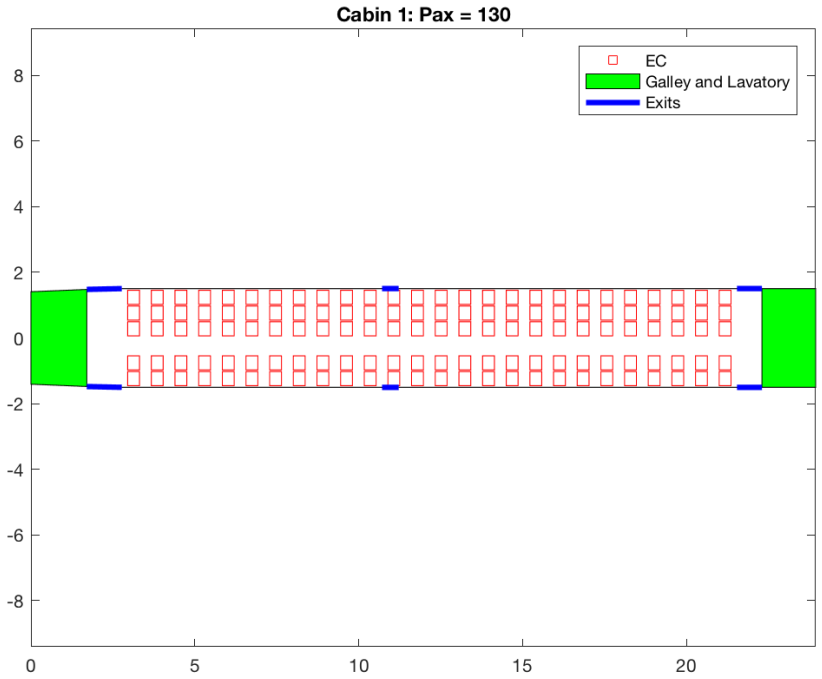

RTP3 Report

The aircraft is a conventional aircraft with a wing aspect ratio of 11. The aircraft is designed to transport 130 passengers with a total payload mass of 13650kg over 2955km.

Specification

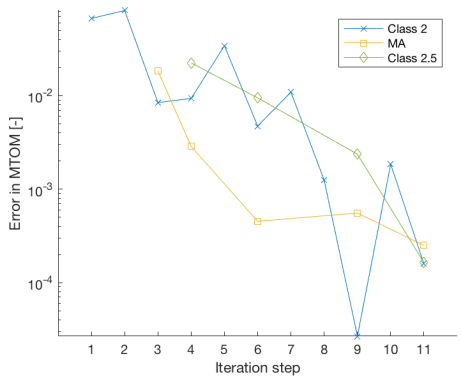

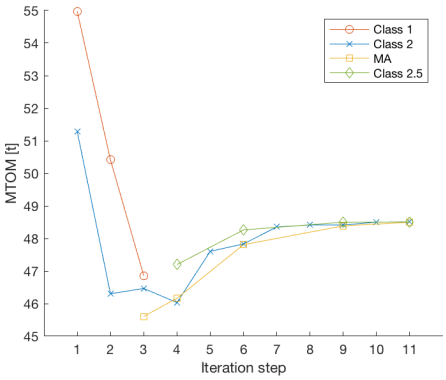

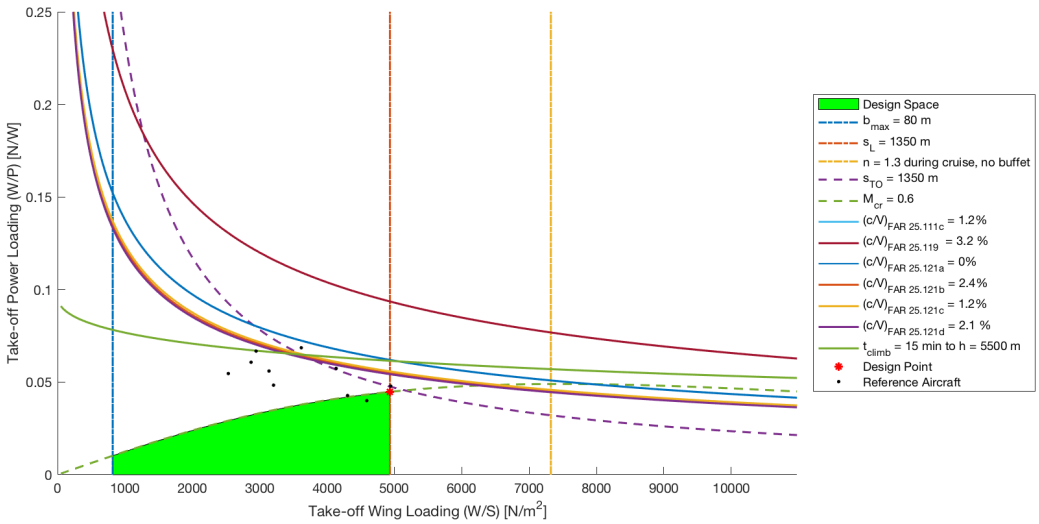

Pax	130	~
Payload Mass	13650	kg
Cruise Mach	0.6	~
Altitude	8500	m
Range	2955	km
Take Off Distance	1350	m
Landing Distance	1350	m
Cargo Mass	3250	kg
Wing loading (MTOM)	4934	N/m^2
Power Loading	0.0447	~

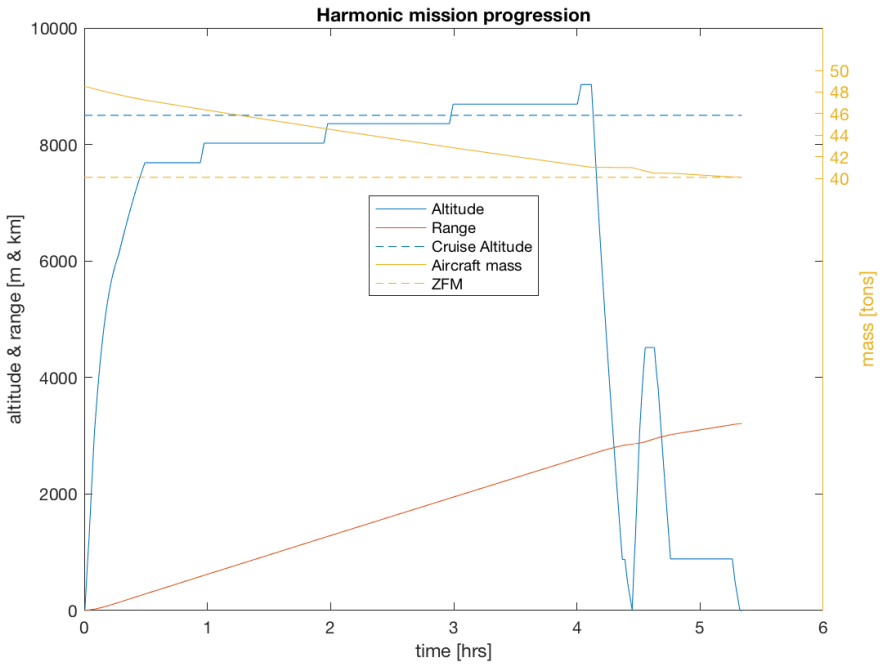

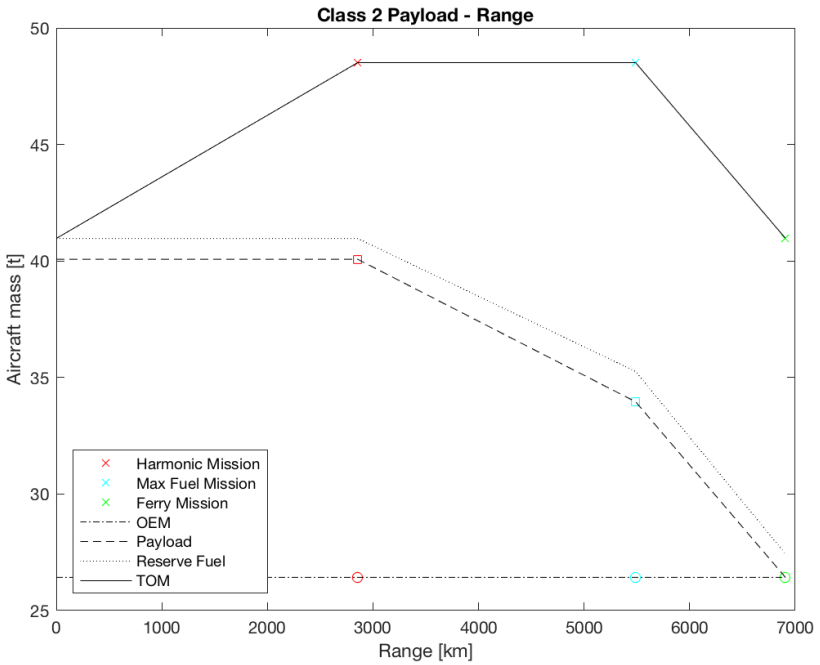

Weight Estimation

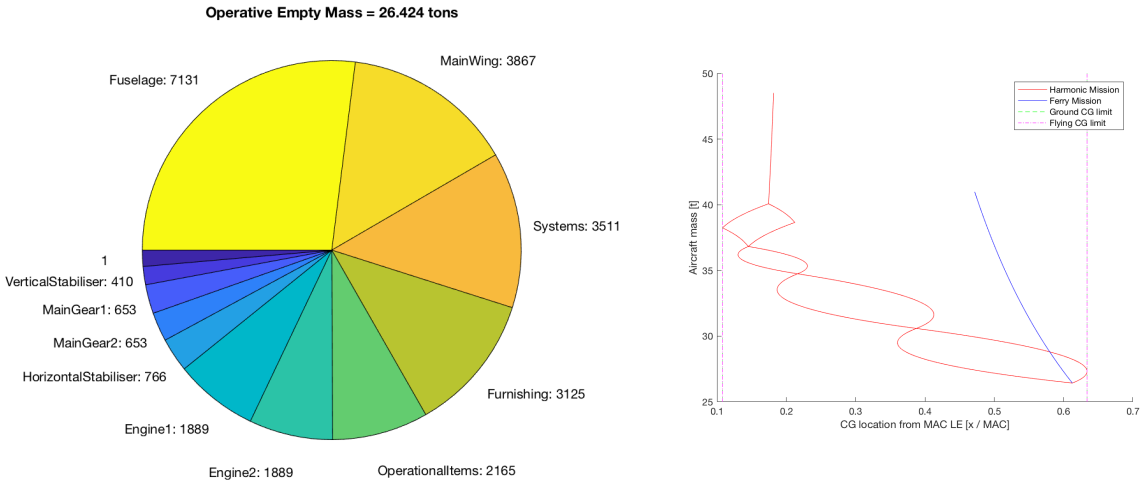

Table J.1: Mass Summary

Maximum take-off mass	48510	kg
Operational empty mass	26424	kg
Design landing mass	40970	kg
Maximum landing mass	41760	kg
Maximum ramp mass	49500	kg
Maximum fuel mass (ferry)	15000	kg
Payload mass	13650	kg
Total fuel mass	8400	kg
Payload mass	13650	kg
Total fuel mass	8400	kg
Reserve fuel mass	1100	kg

Table J.2: Centre-of-gravity locations

X_{cg} (MTOM)	19.5	m
X_{cg} (OEM)	20.9	m
X_{cg} (ZFM)	20.9	m
X_{np}	22.6	m

Aerodynamics

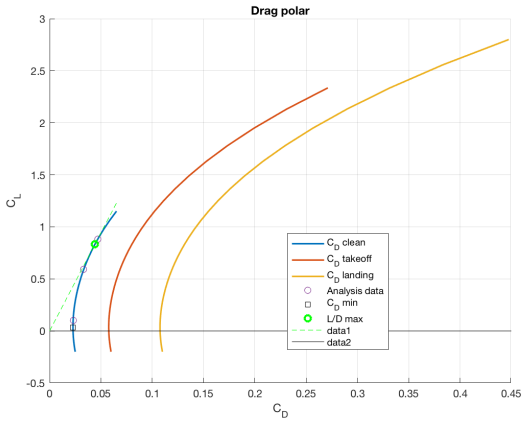

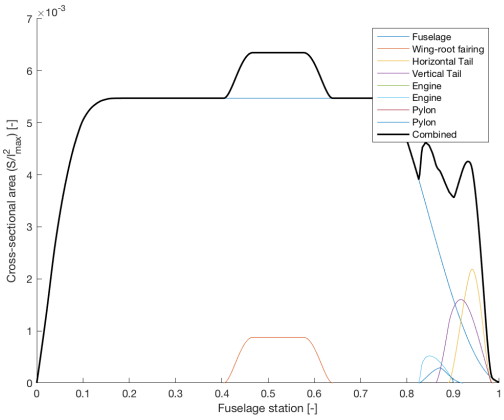

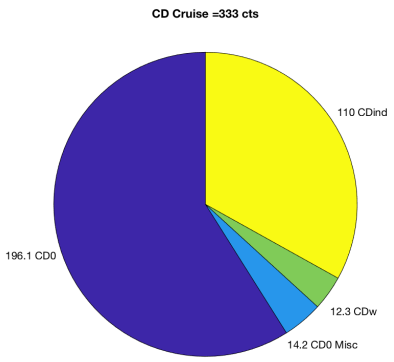

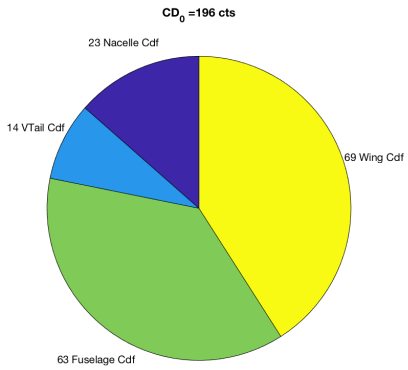

Table J.3: Aerodynamic Properties

$C_{L,\text{cruise}}$	0.59	~
$C_{D,\text{cruise}}$	344	cts
L/D_{cruise}	17.2	~
C_{D_0} (Clean)	228	cts
C_{D_0} (Take-Off)	577	cts
C_{D_0} (Landing)	1077	cts
Oswald factor (e) (Clean)	0.939	~
Oswald factor (e) (Take-Off)	0.889	~
Oswald factor (e) (Landing)	0.839	~
C_{L_α}	7.43	rad^{-1}
C_{m_α}	-7.33	rad^{-1}
$C_{L_{\text{max,clean}}}$	1.18	~
$C_{L_{\text{max,take-off}}}$	2.4	~
$C_{L_{\text{max,landing}}}$	3	~

Aircraft Geometry

Table J.4: Propulsion

Number of engines	2	~
SFC_{cruise}	0.5	h^{-1}
Fan diameter	3.37	m
Number of blades	10	~
Diameter	3.37	m
Length	3.13	m

Table J.5: Main Wing dimensions

Span	32.6	m
Planform area	95.89	m^2
MAC	3.15	m
Root Chord	4.31	m
Root t/c	0.18	~
Tip Chord	1.58	m
Tip t/c	0.13	~
Sections (root to tip)	N663418 N663418 N662415	
Sweep 0.25c	10.2	°
Taper ratio	0.367	~
Twist	0	°
Dihedral	5.5	°

Table J.6: Horizontal Stabilizer dimensions

Span	14.3	m
Planform area	34.21	m^2
MAC	2.44	m
Root Chord	2.98	m
Root t/c	0.1	~
Tip Chord	1.79	m
Tip t/c	0.1	~
Sections (root to tip)	N0012 N0012	
Sweep 0.25c	11.7	°
Taper ratio	0.6	~
Twist	0	°
Dihedral	5.5	°

Table J.7: Vertical Stabilizer dimensions

Span	4.85	m
Planform area	19.59	m^2
MAC	4.06	m
Root Chord	4.49	m
Root t/c	0.12	~
Tip Chord	3.59	m
Tip t/c	0.12	~
Sections (root to tip)	N0012 N0012	
Sweep 0.25c	9.95	°
Taper ratio	0.8	~
Twist	0	°
Dihedral	0	°

Table J.8: Fuselage dimensions

Length	38	m
Diameter	3.18	m
Nose Shape Factor	0.15	~
Tail Shape Factor	0.25	~
Nose Length	3.42	m
Tail Length	10.6	~
Aft Ratio Width	0.05	~
Aft Ratio Height	0.05	~

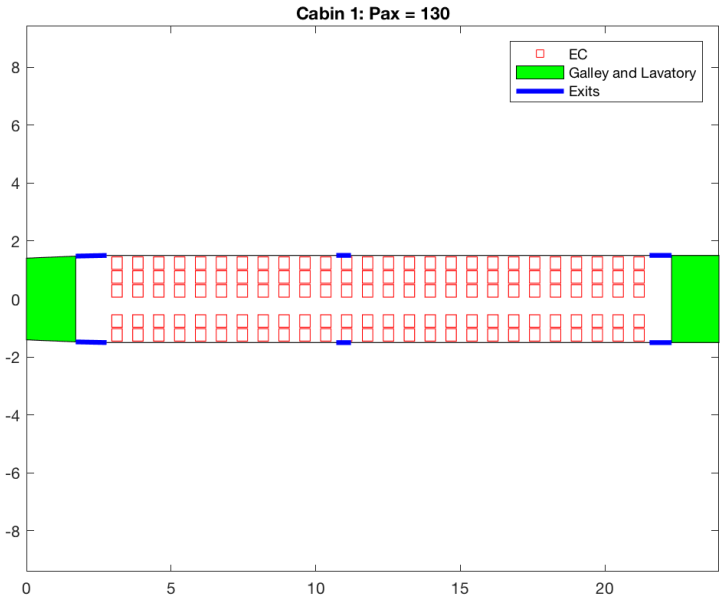

K

RTP4 Report

The aircraft is a conventional aircraft with a wing aspect ratio of 11. The aircraft is designed to transport 130 passengers with a total payload mass of 13650kg over 2955km.

Specification

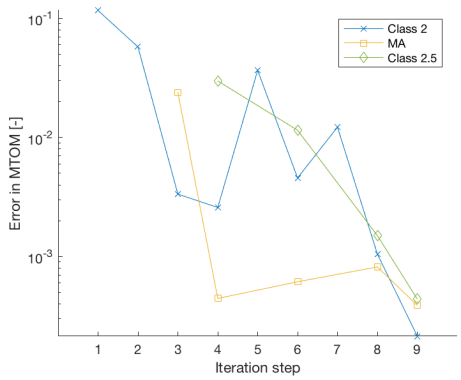

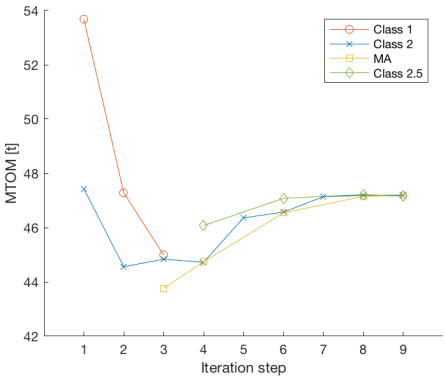

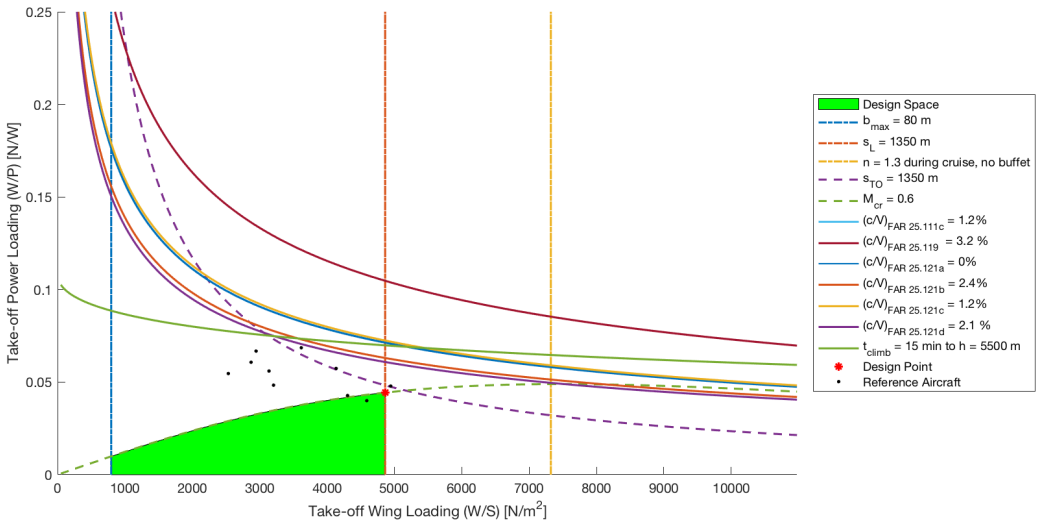

Pax	130	~
Payload Mass	13650	kg
Cruise Mach	0.6	~
Altitude	8500	m
Range	2955	km
Take Off Distance	1350	m
Landing Distance	1350	m
Cargo Mass	3250	kg
Wing loading (MTOM)	4863	N/m^2
Power Loading	0.0443	~

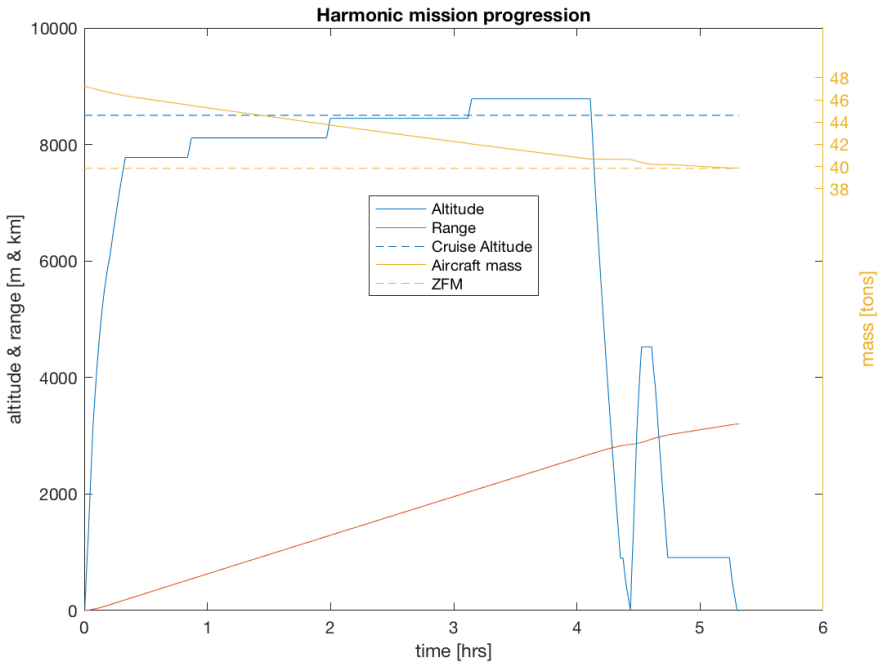

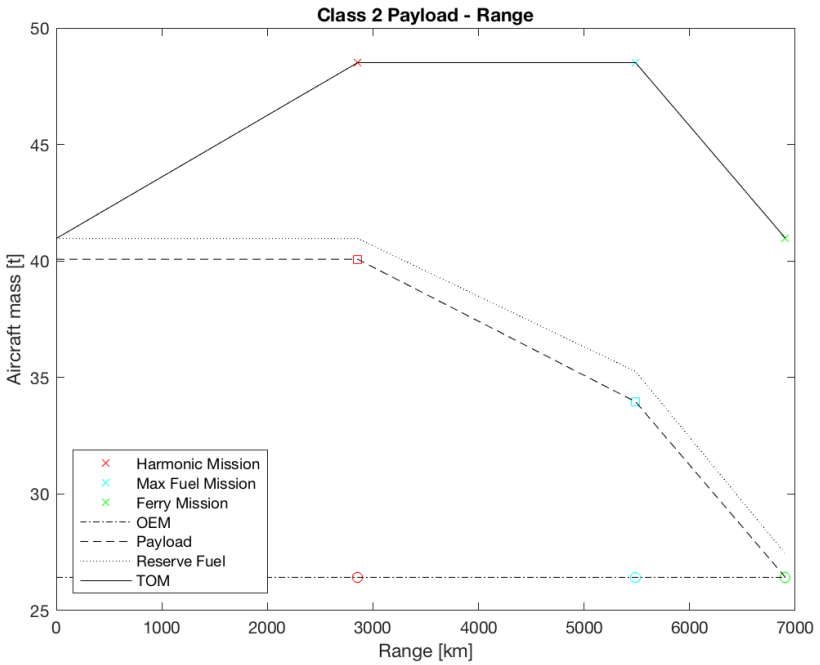

Weight Estimation

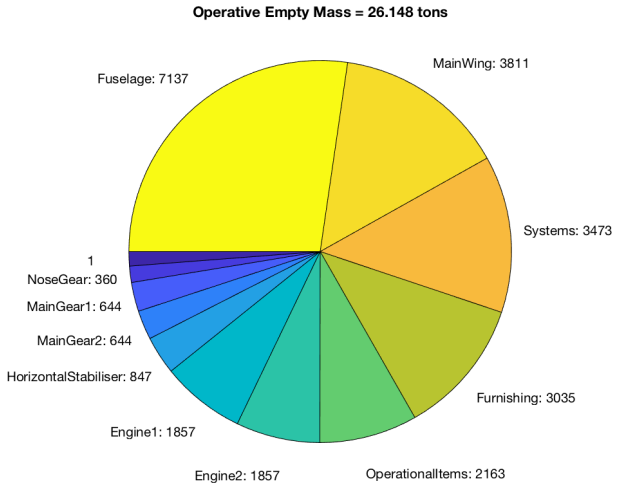

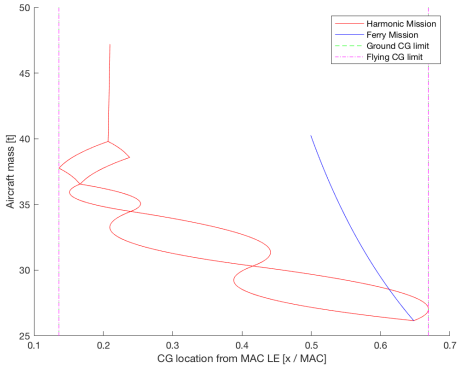

Table K.1: Mass Summary

Maximum take-off mass	47200	kg
Operational empty mass	26148	kg
Design landing mass	40590	kg
Maximum landing mass	41280	kg
Maximum ramp mass	48160	kg
Maximum fuel mass (ferry)	14000	kg
Harmonic range mission:		
Payload mass	13650	kg
Total fuel mass	7400	kg
Max payload mission:		
Payload mass	13650	kg
Total fuel mass	7400	kg
Reserve fuel mass	940	kg

Table K.2: Centre-of-gravity locations

X_{cg} (MTOM)	19.5	m
X_{cg} (OEM)	20.9	m
X_{cg} (ZFM)	20.9	m
X_{np}	22.3	m

Aerodynamics

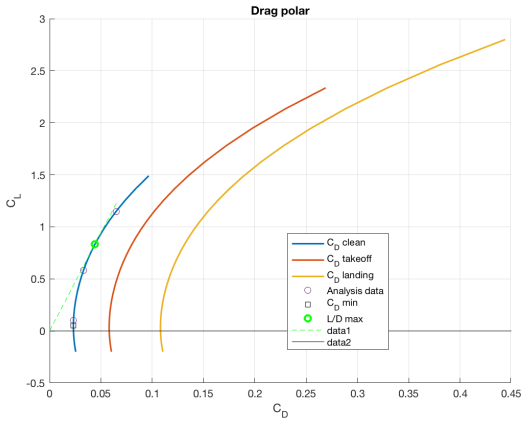

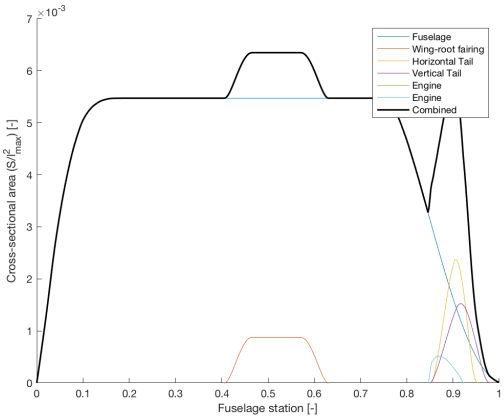

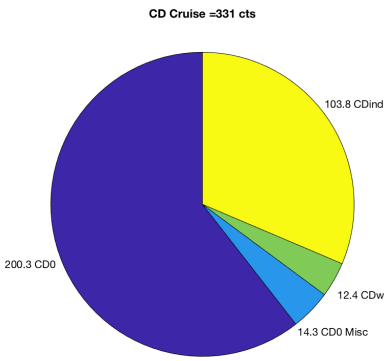

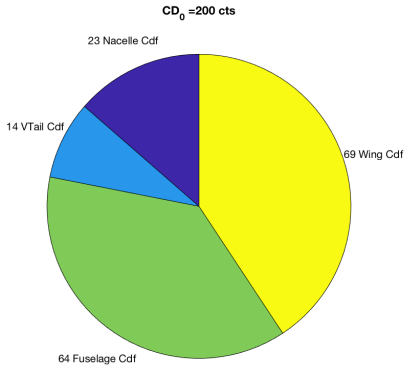

Table K.3: Aerodynamic Properties

$C_{L,\text{cruise}}$	0.58	~
$C_{D,\text{cruise}}$	341	cts
L/D_{cruise}	17.1	~
C_{D_0} (Clean)	233	cts
C_{D_0} (Take-Off)	581	cts
C_{D_0} (Landing)	1081	cts
Oswald factor (e) (Clean)	0.954	~
Oswald factor (e) (Take-Off)	0.904	~
Oswald factor (e) (Landing)	0.854	~
C_{L_α}	7.42	rad^{-1}
C_{m_α}	-6.45	rad^{-1}
$C_{L_{\text{max,clean}}}$	1.53	~
$C_{L_{\text{max,take-off}}}$	2.4	~
$C_{L_{\text{max,landing}}}$	3	~

Aircraft Geometry

Table K.4: Propulsion

Number of engines	2	~
SFC_{cruise}	0.5	h^{-1}
Fan diameter	3.37	m
Number of blades	10	~
Diameter	3.37	m
Length	3.11	m

Table K.5: Main Wing dimensions

Span	32.4	m
Planform area	95.53	m^2
MAC	3.17	m
Root Chord	4.33	m
Root t/c	0.18	~
Tip Chord	1.57	m
Tip t/c	0.13	~
Sections (root to tip)	N663418 N663418 N662415	
Sweep 0.25c	10.2	°
Taper ratio	0.363	~
Twist	0	°
Dihedral	5.5	°

Table K.6: Horizontal Stabilizer dimensions

Span	14.9	m
Planform area	37.19	m^2
MAC	2.54	m
Root Chord	3.11	m
Root t/c	0.1	~
Tip Chord	1.87	m
Tip t/c	0.1	~
Sections (root to tip)	N0012 N0012	
Sweep 0.25c	11.7	°
Taper ratio	0.6	~
Twist	0	°
Dihedral	5.5	°

Table K.7: Vertical Stabilizer dimensions

Span	5.54	m
Planform area	19.19	m^2
MAC	3.67	m
Root Chord	4.95	m
Root t/c	0.12	~
Tip Chord	1.98	m
Tip t/c	0.12	~
Sections (root to tip)	N0012 N0012	
Sweep 0.25c	15.3	°
Taper ratio	0.4	~
Twist	0	°
Dihedral	0	°

Table K.8: Fuselage dimensions

Length	38	m
Diameter	3.18	m
Nose Shape Factor	0.15	~
Tail Shape Factor	0.25	~
Nose Length	3.42	m
Tail Length	10.6	~
Aft Ratio Width	0.05	~
Aft Ratio Height	0.05	~